NMR IN RAPIDLY ROTATED METALS

By

R. S. TIFFEN, B.Sc.

Thesis Submitted to the University of Nottingham
for the Degree of Doctor of Philosophy

MAY 1975

'Let them loiter in pleasure or toilfully spin' !

from 'The Old Sexton'

by Park Benjamin (1809-1864)

ACKNOWLEDGEMENTS

I wish to express my thanks to:

Professor E. R. Andrew for providing me with both the opportunity and the facilities to undertake this work: also his guidance throughout.

Dr. Waldo S. Hinshaw and Dr. James L. Carolan for much practical help and many useful discussions.

Mr. Tony Tatlow for manufacturing the rotors, and for his assistance in trying out the many variations of design.

The Government of the United States of America who through one of their divisions provided me with a grant.

*****

ABSTRACT

Although this thesis is concerned solely with nuclear magnetic resonance, it may be divided into two parts. One part deals with a series of measurements on the NMR parameters of several pure metal powders, namely aluminium, cadmium, niobium and vanadium, and in particular the effect on their resonance spectra of rapid macroscopic sample rotation at the 'magic angle'. The other part relates measurements of spin-lattice relaxation time as a function of temperature for the three solid cuprous halides.

By spinning at high speeds a significant narrowing of the resonance lineshape has been achieved in the case of cadium and aluminium. This has enabled precise determinations of their isotropic Knight shifts to be made. For cadmium the width of the residual symmetric central spectrum has been used to obtain an estimate of the magnitude of the indirect electron coupled exchange interaction. Complete narrowing of the aluminium resonance line requires rotation rates in excess of 8 kHz. To this end it has been necessary to develop a new rotor system capable of carrying small metal samples at extremely high spinning rates. In connection with the work on aluminium, pure powder specimens have been prepared which exhibit values of second moment and dipolar relaxation time that agree well with theory. This is in contradiction to the results obtained from filed powders and those recorded by all other workers.

Below room temperature the form of the T_1 results obtained from the cuprous halides is in accord with the theory of Raman

quadrupole relaxation. However theoretical T_1 values, as derived from the simple Raman two-phonon mechanism in an ionic crystal lattice, fail to give quantitative agreement with experiment.

CONTENTS

Page

CHAPTER 1. INTRODUCTION TO THE NMR TECHNIQUE

CHAPTER 2. SPIN-SPIN AND SPIN-LATTICE INTERACTIONS

CHAPTER 3. NARROWING THE NUCLEAR RESONANCE SPECTRUM BY MACROSCOPIC ROTATION

CHAPTER 4. EXPERIMENTAL ROTATION SYSTEMS

CHAPTER 5. EXPERIMENTAL PROCEDURE

CHAPTER 6. MEASUREMENTS OF THE SPIN-LATTICE RELAXATION TIMES IN THE CUPROUS HALIDES

CHAPTER 7. EXPERIMENTAL RESULTS ON ALUMINIUM METAL

CHAPTER 8. MEASUREMENTS ON VANADIUM, NIOBIUM AND CADMIUM METALS

*****

CHAPTER 1

INTRODUCTION TO THE NMR TECHNIQUE

1.1 BASIC THEORY

A large number of nuclear species possess an intrinsic spin I with a corresponding angular momentum ($\underline{J} = \hbar\underline{I}$) and a resulting magnetic moment

$$\underline{\mu} = \gamma\underline{J} = \gamma\hbar\underline{I}$$

where γ is the gyromagnetic ratio. If a magnetic field $\underline{H}_o$ is applied along the z axis of the laboratory reference frame, the Zeeman interaction with the magnetic moment is given by the Hamiltonian

$$\begin{aligned}\mathcal{H} &= -\underline{\mu}.\underline{H}_o \\ &= -\gamma\hbar H_o I_z \ .\end{aligned} \tag{1.1}$$

The eigenvalues of this Hamiltonian give rise to (2I + 1) energy levels, of energy separation $\gamma\hbar H_o$, such that

$$\begin{aligned}E_m &= -\langle I,m|\gamma\hbar H_o I_z|I,m\rangle \\ &= -\gamma\hbar H_o m\end{aligned} \tag{1.2}$$

with m = I, I - 1, ... -I, where $|I,m\rangle$ are the spin eigenfunctions. Transitions between these energy levels governed by the selection rule $\Delta m = \pm 1$ may be induced by an alternating magnetic field of frequency ν applied in a direction perpendicular to H_o. The condition for resonance is satisfied when $2\pi\nu = \omega_o = \gamma H_o$, where ω_o is the Larmor angular precession frequency.

In considering the motion of the spin magnetic moment at resonance it is useful to introduce a rotating co-ordinate system. The classical equation of motion of the spin magnetic moment in a static field $H_o\underline{k}$ is given by equating torque with rate of change of angular momentum so

$$\frac{d\underline{\mu}}{dt} = \underline{\mu} \times (\gamma H_o)\underline{k} \; . \tag{1.3}$$

The quantum mechanical expectation value of the magnetic moment obeys an identical relationship. It can be shown (Slichter, p.11) that in a reference frame I* rotating about the z axis with angular frequency W, equation (1.3) becomes

$$\left(\frac{d\underline{\mu}}{dt}\right)^* = \underline{\mu}^* \times (\gamma H_o + W)\underline{k} \; . \tag{1.4}$$

This has the same form as equation (1.3) with H_o replaced by an effective field

$$\underline{H}_{eff} = \underline{H}_o + \frac{\underline{W}}{\gamma} \; .$$

We now consider the addition of a circularly polarized and positively rotating magnetic field given by

$$H_1(t) = H_1(\underline{i} \cos wt + \underline{j} \sin wt) \; .$$

The total magnetic field in the laboratory reference frame is then

$$\underline{H} = H_o\underline{k} + H_1\underline{i} \cos wt + H_1\underline{j} \sin wt$$

and

$$\frac{d\underline{\mu}}{dt} = \underline{\mu} \times \gamma(\underline{H}_o + \underline{H}_1) \; . \tag{1.5}$$

Transforming to the rotating frame such that W = +w both H_o and H_1 will be static. With the choice of the $\underline{i}^*$ axis of the rotating frame to lie along H_1 equation (1.3) becomes

$$\left(\frac{d\underline{\mu}}{dt}\right)^* = \underline{\mu}^* \times \gamma\left[(H_o + \frac{w}{\gamma})\underline{k} + H_1\underline{i}^*\right] \tag{1.6}$$

and

$$\underline{H}_{eff} = (H_o + \frac{w}{\gamma})\underline{k} + H_1\underline{i}^* \ . \tag{1.7}$$

Thus, in the rotating frame, μ precesses in a cone about H_{eff} with angular frequency γH_{eff}, and at a fixed angle θ to the z axis where

$$\theta = \tan^{-1}\left[\frac{H_1}{H_o + \frac{w}{\gamma}}\right] . \tag{1.8}$$

At resonance $w = -\gamma H_o$ so $H_{eff} = H_1$ and μ^* will precess about H_1 with $\theta = \pi/2$. Assuming that at t = 0 μ lies along the k axis, then if H_1 is applied as a pulse at the resonance frequency for a time duration $\delta\tau$ the angle through which the magnetic moment nutates is given by

$$\phi = \gamma H_1 \delta\tau \ . \tag{1.9}$$

The rf pulse may then be defined by this angle.

Providing the system of spins is non-interacting the above equations are equally applicable to the expectation value of the macroscopic total magnetic moment M.

In the experimental situation an alternating rf voltage V cos ωt is applied to a coil wound around the sample with its axis perpendicular to H_o. A linearly polarized magnetic field is produced which is equivalent to two counter rotating components of equal amplitude H_1. While the component rotating in the opposite direction to the Larmor precession may be ignored (Abragam p.21) the other component fulfils the role of the perturbing H_1 field described above. In continuous wave NMR (CWNMR) the perturbation is applied continuously and at resonance will upset the Boltzmann energy distribution of the nuclear spins by transferring energy to the spin system. By keeping the magnitude of H_1 low, the system remains close to thermal equilibrium. The absorption of energy by the spin system can then be measured as either H_o or the driving frequency ν is swept slowly through the resonance condition. In pulsed NMR (PNMR) a short,intense pulse of resonant rf voltage is applied to the coil causing the magnetic moment to precess about H_1 in the rotating frame. After the pulse is switched off the spin system returns to equilibrium at a rate determined by the interaction of the spins with the lattice and each other. It is with the PNMR method that we are primarily concerned here.

1.2 SPIN-SPIN AND SPIN-LATTICE RELAXATION TIMES

We now introduce the phenomenological equation of motion for the macroscopic magnetic moment first proposed by Bloch$^{(1)}$. In this equation the return to equilibrium is defined by two separate relaxation times so

$$\frac{d\underline{M}}{dt} = \gamma \underline{M} \times \underline{H} - \frac{M_x \underline{i} + M_y \underline{j}}{T_2} - \frac{(M_Z - M_o)}{T_1} \underline{k} \quad . \tag{1.10}$$

T_1 is the spin-lattice relaxation time describing the rate at which the nuclear spin system approaches thermal equilibrium with the lattice and T_2 is the spin-spin relaxation time describing the decay of any transverse magnetization. Bloch's equation predicts a Lorentzian lineshape function

$$f(\omega) = \frac{T_2}{\pi}\frac{1}{1 + \omega^2 T_2^2}$$

which usually provides a good approximation of the experimental lineshape obtained from liquid samples. Implicit in equation (1.10) is the assumption that both the transverse and longitudinal magnetizations decay exponentially. Although the decay of transverse magnetization in solids does not usually obey such a relationship, the two relaxation processes introduced in equation (1.10) are generally valid. The absorption lineshapes obtained from solids can often be represented satisfactorily by a Gaussian-shape function

$$f(\omega) = \frac{1}{\Delta\sqrt{2\pi}}\, e^{-\omega^2/2\Delta^2}$$

where Δ is the half-width between points of maximum slope of $f(\omega)$ and $1/\Delta\sqrt{2\pi}$ is a normalizing factor.

At this point we consider the development of the nuclear magnetization in the rotating frame following a 90° rf pulse applied along the x* axis. Immediately after the pulse the nuclear magnetization will lie along the y* axis. In solids the spins experience finite local internal magnetic fields (described in detail in the next chapter) which give rise to a spread of precession frequencies about ω_o. As a result the spins begin to fan out about y* in the x-y plane, and the transverse magnetization decays with a characteristic time T_2. Any mechanism leading to a loss of transverse magnetization will contribute to T_2. This includes the effect of a non-uniform external magnetic field across the sample as well as processes governing the return of the nuclear magnetization to thermal equilibrium - along the z axis - with time constant T_1.

1.3 COMPARISON BETWEEN PNMR AND CWNMR METHODS

In PNMR, following the rf pulse the voltage induced in the receiver coil by the rotating magnetic moment may be observed using phase coherent detection. The resulting signal is termed the free induction decay (FID). When the rf reference applied to the detector is equivalent to ω_o, the detected signal $V_d(t)$ can be set to trace out the decay of M_y^* directly. Hence, at any point in time τ

$$V_d(\tau) \propto M_y^*(\tau) = \mu\sum_{\omega'}\cos \omega'\tau\delta N_{\omega'}(\tau) \qquad (1.11)$$

where $\omega' = \omega - \omega_o$ and $\delta N_{\omega'}$ is the number of spins per unit volume with frequency between ω' and $\omega' + \delta\omega$.

With perfect instrumentation and negligible saturation the absorption spectrum obtained from the CWNMR method is a direct measure of the distribution of precession frequencies present in the sample. Writing the normalized lineshape function as $f(\omega')$ it follows that in the rotating frame the fraction of spins with angular precession frequency between ω' and $\omega' + \delta\omega$ is given by $f(\omega')\delta\omega$. Therefore

$$\delta N_{\omega'} = f(\omega')\delta\omega$$

and

$$V_d(t) \propto \int_{-\infty}^{+\infty} f(\omega')\cos \omega' t \, d\omega$$

$$= G(t) \ . \qquad (1.12)$$

If the nuclear lineshape is symmetric about $\omega' = 0$, $G(t)$ may be rewritten in the form

$$G(t) = 2\pi \int_{-\infty}^{+\infty} f(\nu')\exp(-2\pi i\nu' t)d\nu \qquad (1.13)$$

where $\nu' = \omega'/2\pi$. Hence, we have shown that the observed FID is equivalent to the Fourier transform of the absorption lineshape. It follows that the lineshape may be defined by the inverse Fourier transform of the FID.

In the case where $f(\omega')$ is asymmetric the lineshape is obtained by including the two components of the transverse decay, along the x* and y* axes, in the complex Fourier transform(2)

$$f(\omega') = \int_{-\infty}^{+\infty} M_y^* \cos \omega' t + M_x^* \sin \omega' t \, dt \ .$$

A similar result is achieved by shifting the detection frequency by a value σ (greater than the linewidth) away from ω_0, and recording the decay component $M_y^*(t)$. It is then only necessary to define the phase of $M_y^*(t)$ in order to obtain the asymmetric spectrum from a symmetric transform about σ.

CHAPTER 2

SPIN-SPIN AND SPIN-LATTICE INTERACTIONS

2.1 INTRODUCTION

For an assembly of nuclear spins the (2I + 1) discrete energy levels described by the eigenvalues of the Zeeman Hamiltonian are broadened by internal interactions. The complete Hamiltonian can be written as

$$\mathscr{H} = \mathscr{H}_Z + \mathscr{H}_{int} \quad .$$

$\mathscr{H}_{int}$ may consist of several different terms but, providing quadrupole effects are not large, it is generally considered as a perturbation of the Zeeman Hamiltonian. If $\mathscr{H}_{int}$ contains diagonal matrix elements between the Zeeman eigenstates it results in shifts and/or broadening of the nuclear levels with a corresponding structure and broadening of the resonance spectrum. These secular terms commute with $\mathscr{H}_Z$. The off-diagonal matrix elements of $\mathscr{H}_{int}$ connect states of different eigenvalue m and hence give rise to transitions between energy levels. In this way the non-secular terms are responsible for the relaxation of the spin system to the temperature of the lattice.

There are four main secular components of $\mathscr{H}_{int}$. Hence the spin Hamiltonian may be written as

$$\mathscr{H} = \mathscr{H}_Z + \mathscr{H}_D + \mathscr{H}_Q + \mathscr{H}_S + \mathscr{H}_J$$

where the terms represent the Zeeman, dipolar, quadrupole, frequency (chemical and Knight) shift and the indirect exchange interactions respectively. We now describe the spin-spin interactions briefly in turn.

2.2 SECULAR INTERACTIONS

2.2.1 DIPOLAR INTERACTION

From the classical energy of interaction between dipole moments the dipolar Hamiltonian over N spins can be written as

$$\mathcal{H}_D = \sum_{i<j}^{N} \frac{\gamma_i\gamma_j}{r_{ij}^3}\hbar^2\left[\underline{I}_i\cdot\underline{I}_j - \frac{3(\underline{I}_i\cdot\underline{r}_{ij})(\underline{I}_j\cdot\underline{r}_{ij})}{r_{ij}^2}\right] \qquad (2.1)$$

where the summation is performed once over each pair of spins and $\underline{r}_{ij}$ is the position vector between spins $\underline{I}_i$ and $\underline{I}_j$. Rewriting this expression in terms of spherical co-ordinates we get

$$\mathcal{H}_D = \sum_{i<j}^{N} \frac{\gamma_i\gamma_j}{r_{ij}^3}\hbar^2\left[A + B + C^+ + C^- + D^+ + D^-\right]$$

where

$$A = I_{iz}I_{jz}(1 - 3\cos^2\theta)$$

$$B = -\tfrac{1}{4}\left[I_i^+I_j^- + I_i^-I_j^+\right](1 - 3\cos^2\theta)$$

$$C^{\pm} = -\tfrac{3}{2}\left[I_i^{\pm}I_{jz} + I_{iz}I_j^{\pm}\right]\sin\theta\cos\theta\, e^{\mp i\phi}$$

$$D^{\pm} = -\tfrac{3}{4}I_i^{\pm}I_j^{\pm}\sin^2\theta\, e^{\mp 2i\phi}$$

and

$$I^{\pm} = I_x \pm iI_y \ .$$

Term A represents the effect of the static local field produced at spin $\underline{I}_i$ by $\underline{I}_j$. From a classical viewpoint, term B can be considered as arising from the rotating component of the local field. For identical nuclei it connects states of zero total spin, i.e. $\Delta(m_i + m_j) = 0$, causing mutual spin flips between energy levels. In this way the lifetime of a spin state is limited and both terms will contribute to the width of the resonance line. Whereas term A is always secular, term B is only secular between like nuclei.

Terms C and D are non-secular. C gives rise to single spin flips $\Delta(m_i + m_j) = \pm 1$ and D flips pairs of spins simultaneously $\Delta(m_i + m_j) = \pm 2$.

To first order the non-secular terms of $\mathcal{H}_D$ will only contribute indirectly to the resonance linewidth by limiting the lifetime of the energy states. The second order effect is an admixing of spin states resulting in second order energy shifts and permitting otherwise forbidden transitions between states. Weak satellite lines are produced in this manner at multiples of the resonance frequency, but these are normally disregarded. The truncated Hamiltonian which neglects the non-secular interactions is given by

$$\mathcal{H}_D^T = \frac{1}{2} \sum_{i<j}^{N} \frac{\gamma_i \gamma_j}{r_{ij}^3} \hbar^2 \left[\underline{I}_i \cdot \underline{I}_j - 3 I_{iz} I_{jz}\right] (3 \cos^2\theta - 1). \tag{2.2}$$

The dipolar Hamiltonian may be represented as the tensor interaction

$$\mathcal{H}_D = \sum_{i<j}^{N} \frac{\gamma_i \gamma_j}{r_{ij}^3} \hbar^2 \left[\underline{I}_i \cdot \underline{D}_{ij} \cdot \underline{I}_j\right] . \tag{2.3}$$

If $\underline{r}_{ij} = \underline{n}r_{ij} = (\lambda_1\underline{i} + \lambda_2\underline{j} + \lambda_3\underline{k})$ where $\lambda_1\lambda_2\lambda_3$ are direction cosines, then

$$D_{ij} = \begin{bmatrix} 1-3\lambda_1^2 & -3\lambda_1\lambda_2 & -3\lambda_1\lambda_3 \\ -3\lambda_1\lambda_2 & 1-3\lambda_2^2 & -3\lambda_2\lambda_3 \\ -3\lambda_1\lambda_3 & -3\lambda_2\lambda_3 & 1-3\lambda_3^2 \end{bmatrix} .$$

Since $\lambda_1^2 + \lambda_2^2 + \lambda_3^2 = 1$, and $D_{\ell m} = D_{m\ell}$ the tensor is traceless and symmetric.

Similarly the truncated dipolar interaction may be represented by the traceless symmetric tensor

$$D_{ij}^T = \begin{bmatrix} 1 & 0 & 0 \\ 0 & 1 & 0 \\ 0 & 0 & -2 \end{bmatrix} (3\cos^2\theta - 1) .$$

2.2.2 THE QUADRUPOLE INTERACTION

Nuclei with spin greater than ½ possess an electric quadrupole moment and therefore interact with electric field gradients produced by the surrounding charge distribution. Following the approach of Cohén and Reif(3) this interaction may be written in the form of a product of two second rank symmetric tensors so

$$\mathscr{H}_Q = \tfrac{1}{2} \sum_{\alpha,\beta} \left(\frac{\partial^2 V}{\partial\alpha\partial\beta}\right)_{r=0} Q_{\alpha\beta} \tag{2.4}$$

$$= \frac{eQ}{6I(2I-1)} \sum_{\alpha,\beta} \left(\frac{\partial^2 V}{\partial\alpha\partial\beta}\right)_{r=0} \left[\frac{3}{2}(I_\alpha I_\beta + I_\beta I_\alpha) - \delta_{\alpha\beta} I(I+1)\right]$$

where $V(r)_{r=0}$ is the crystalline electrostatic potential at the nucleus, $\alpha\beta$ refers to any pair of cartesian axes and Q is the quadrupole moment.

The tensor $\partial^2V/\partial\alpha\partial\beta$ (now written as $V_{\alpha\beta}$) representing the electric field gradient is diagonalized in its principal reference frame (i,j,k). From Laplace's equation $\sum V_{ii} = 0$, so the tensor is also traceless. In a position of cubic symmetry $V_{ii} = V_{jj} = V_{kk}$ and the quadrupole interaction therefore vanishes. Generally the principal axes are chosen so that $|V_{kk}| \geq |V_{jj}| \geq |V_{ii}|$, and an asymmetry parameter η and field gradient q are defined so

$$eq = V_{kk} \qquad \eta = \frac{V_{ii} - V_{jj}}{V_{kk}} \; .$$

The quadrupole Hamiltonian then becomes

$$\mathcal{H}_Q = \frac{e^2qQ}{4I(2I-1)} |3I_z^2 - I(I+1) + \eta(I_i^2 - I_j^2)| \; . \tag{2.5}$$

If the electric field gradients arise from defects in an otherwise cubic lattice structure the quadrupole interaction can be treated as a perturbation of the Zeeman Hamiltonian. Assuming axial symmetry ($V_{ii} = V_{jj}$) and that the angle between the external field H_o and the k axis is θ, the eigenvalues of the Hamiltonian $\mathcal{H} = \mathcal{H}_Z + \mathcal{H}_Q$ are given by

$$E_m = -\gamma\hbar H_o I_z + \frac{e^2qQ}{4I(2I-1)} \left(\frac{3\cos^2\theta - 1}{2}\right) |3m^2 - I(I+1)| \; . \tag{2.6}$$

As the energy levels $m = \pm\frac{1}{2}$ are shifted equally the centre of gravity of the resonance line is unaffected. The 2I satellite lines occur at frequencies

$$\nu_m \rightarrow \nu_{m-1} = \nu_o + \frac{3e^2Qq(2m-1)}{(8I-1)} (3\cos^2\theta - 1) \; .$$

In powdered samples a weak interaction of this form usually results in an increase in the linewidth and an enhancement of the wings of the absorption lineshape(4). In cases where the quadrupole interaction is large it can no longer be considered as a perturbation of $\mathcal{H}_Z$, and the central $\frac{1}{2} \rightarrow -\frac{1}{2}$ transition is also shifted.

2.2.3 FREQUENCY SHIFT MECHANISMS

(a) Chemical Shifts

The chemical shift interaction arises via the magnetic coupling between the external magnetic field H_o and the motion of electronic charges. For a fixed value of H_o the nuclear resonance frequency of any nuclear species depends in principle upon the particular chemical sample observed. The precession of electrons about H_o produces a diamagnetic contribution to the magnetic field at the nucleus. Polarization of the electronic orbitals gives rise to a second order paramagnetic contribution to this field. Although in most samples the orbital angular momentum is quenched, the applied field produces an admixing of electronic states which results in states having non-zero expectation values of angular momentum. The total additional magnetic field at the nucleus is proportional to H_o, so the effective field is given by

$$\underline{H}_{eff} = \underline{H}_o(\underline{I} - \underline{\sigma})$$

where $\underline{I}$ is the unit tensor and $\underline{\sigma}$ is the chemical shift tensor. The chemical shift interaction may be written

$$\mathcal{H}_C = \sum_j \gamma_j \hbar \underline{I}_j \cdot \underline{\sigma}_j \cdot \underline{H}_o \qquad (2.7)$$

so if H_o is applied along the z axis we have

$$\mathcal{H}_C = \sum_j \hbar H_o | I_{jx}\sigma_{jxz} + I_{jy}\sigma_{jyz} + I_{jz}\sigma_{jzz} | \ . \qquad (2.8)$$

In practice the magnitude of the chemical shift is small so only the σ_{zz} component need be considered.

(b) Knight Shifts

The nuclear resonance properties of metals are dominated by the conduction electrons. Although these electrons are non-localized they have predominantly s-type wave functions which have large probability densities at any nucleus. This results in a magnetic hyperfine interaction, the magnitude of which depends upon the average orientation of all the conduction electrons. In the presence of an applied magnetic field any unpaired electron spins are polarized so there is a net spin density of s spins parallel to the applied field. Because the spin susceptibility of the conduction electron gas is small the resulting positive shift in the magnetic field experienced at any nucleus is also small. The Hamiltonian describing this contact term may therefore be treated as a perturbation of the Zeeman Hamiltonian. It is given by

$$\mathcal{H}_K = \gamma\hbar \underline{I}.\underline{H}_o \frac{8\pi}{3} \chi_s \Omega < |\psi_k(0)|^2 >_F \qquad (2.9)$$

where χ_s is the electron spin susceptibility per unit volume, $<|\psi_k(0)|^2>_F$ is the average probability density at the nucleus of the conduction electron states at the Fermi surface, and Ω is the atomic volume.

This contact term manifests itself as a small difference in the resonance frequencies of a particular nucleus in the metal and in a diamagnetic compound. This frequency shift, called the Knight shift, is defined as

$$K = \frac{\nu_m - \nu_r}{\nu_r}$$

where ν_m and ν_r are the resonance frequencies of the metal and reference compound respectively in the same external field.

Because of the existence of chemical shifts any Knight shift value will depend upon the particular reference compound used. Similar chemical shifts are also present in metals usually arising from the shielding of nuclei by the inner shell electrons. Although this effect may not be negligible, it is usually approximately equal for the metal and reference compound so it can be ignored. Reference compounds are normally chosen which have no large paramagnetic contribution to the chemical shift. Measured Knight shifts are then usually much greater than the chemical shifts between different possible reference samples.

From equation (2.9) the Knight shift can be written

$$K = \frac{\nu_m - \nu_r}{\nu_r} = \frac{\Delta\nu}{\nu_o} = \frac{8\pi}{3} \chi_s \Omega \langle |\psi_k(0)|^2 \rangle_F \quad . \qquad (2.10)$$

This predicts that the Knight shift is

(i) Positive and independent of the applied field.

(ii) Insensitive to temperature.

(iii) Dependent upon atomic number.

These predictions are generally confirmed but other interactions also contribute to the experimental value(5).

From a classical point of view the paired s electrons in the filled shells cannot contribute to the contact term. However they become exchange polarized by the polarized conduction electrons. The magnitude and sign of the resulting hyperfine field depends upon the relative s,p,d, etc. character of the conduction electron wave functions. Generally this term appears to enhance the Knight shift; in some cases by as much as 30%(6). Similarly, for metals and alloys with unfilled electron shells the applied field produces a net polarization. The unfilled shells exchange polarize the core s electrons resulting in a negative effective field at the nucleus(7). The negative Knight shifts recorded for platinum(8) and palladium(9) have been accounted for in this way.

Most transition metals have large Knight shifts. This is due in part to the large density of states at the Fermi surface of the narrow conduction bands, but there is also a large second order paramagnetic orbital contribution arising from the small energy separation between the occupied and unoccupied levels(10,11).

The p and d character of the conduction electron wave function couples with the nucleus through a classical dipolar interaction between spins. In metals with cubic symmetry such an interaction is zero, but for non-cubic metals it gives rise to anisotropic Knight shifts. Polycrystalline metal samples are normally used in NMR measurements. This anisotropy then becomes apparent as a field-dependent broadening of the resonance spectrum. Following Winter (p. 53), assuming axial symmetry the resonance frequency at a nuclear site is given by

$$\nu = \nu_s + \tfrac{1}{2}\alpha(3\cos^2\theta - 1)$$

where θ is the angle between the quadratic axis and the magnetic field, $\nu_s = \nu_o(1 + K_{iso})$ and α is proportional to the value of the anisotropic shift. In powdered samples all possible values of θ are equally probably and the lineshape is given by

$$g(\nu) \equiv |2(\nu - \nu_s) + \alpha|^{-\frac{1}{2}} \tag{2.11}$$

for $\alpha \geq (\nu - \nu_s) > -\frac{1}{2}\alpha$. In practice the singularity predicted when $\nu = \nu_s - \frac{1}{2}\alpha$ (i.e. $g(\nu) = \infty$) is suppressed by other sources of broadening.

The Knight shift interaction may of course be represented in tensorial form in the same manner as the chemical shift so

$$\mathcal{H}_K = \sum_j \gamma_j \hbar \underline{I}_j \cdot \underline{K}_j \cdot \underline{H}_o$$

where $\underline{K}_j$ is a second rank tensor. Assuming that the Knight shift tensor components are small this can be again rewritten in the form

$$\mathcal{H}_K = \sum_j \gamma_j \hbar H_o I_{jz} K_{jzz} \quad . \tag{2.12}$$

2.2.4 INDIRECT SPIN-SPIN COUPLING

(a) Non-Metals

To first order there is no coupling between electrons and nuclei in diamagnetic compounds because there is zero total electron spin. There is however a second order effect. Classically a nucleus slightly perturbs its electronic states and through exchange coupling between electrons this results in an indirect spin-spin coupling between nuclei. The interaction is proportional to the magnetic moment of the nuclei and can be written in the form

$$A_{ij}\underline{\mu}_i\cdot\underline{\mu}_j \quad .$$

Such an interaction was first postulated to explain line splittings observed in liquids(12). Similar effects occur in solids but with the exception of metals are usually obscured by dipolar broadening of the resonance line.

We mention at this point the circumstances which may tend to average the indirect exchange interaction to zero. If the lifetime of the Zeeman energy state of either spin is much shorter than h/A, then the second spin experiences a time averaged hyperfine field which averages to zero over the period h/A. Rapid chemical exchange will result in a similar averaging effect.

(b) Metals

The indirect exchange interaction can be written in the form

$$\mathcal{H}_J = \sum_{i<j} \hbar\underline{I}_i\cdot\underline{J}_{ij}\cdot\underline{I}_j \tag{2.13}$$

where J is a second rank tensor.

For metals this tensor is symmetric and can be divided into two parts, a scalar and a symmetric traceless tensor. The symmetric traceless tensor arises from an indirect interaction between nuclei via a classical dipolar coupling between the nuclei and the non-s-character conduction electrons. Because it has the same form as the normal dipolar coupling between nuclei this interaction is often termed pseudo-dipolar. It is only substantial in heavy metals where the p character of the conduction electron wave functions is large. With the assumption of a spherical Fermi surface the pseudo-dipolar interaction may be written as$^{(13)}$

$$\mathcal{H}_{P.D.} = \sum_{i<j} B_{ij}\left[\underline{I}_i\cdot\underline{I}_j - 3\frac{(\underline{I}_i\cdot\underline{r}_{ij})(\underline{I}_j\cdot\underline{r}_{ij})}{r_{ij}^2}\right] . \qquad (2.14)$$

For large distances B_{ij} typically falls off as r_{ij}^{-3} .

The scalar term arises from an isotropic indirect exchange interaction between nuclei via the s type conduction electrons. The Hamiltonian describing this interaction can be written

$$\mathcal{H} = \sum_{i<j} A_{ij}\underline{I}_i\cdot\underline{I}_j \quad . \qquad (2.15)$$

The evaluation of A_{ij} is not trivial. However with the assumption that the Fermi surface is spherical Ruderman and Kittel$^{(14)}$ obtained an expression of the form

$$A_{ij} = \frac{2}{9\pi}\gamma e^2\gamma_i\gamma_j\hbar^2 m^*\Omega^2|\psi_k(0)|^4\left[\frac{2k_F r_{ij}\cos 2k_F r_{ij} - \sin 2k_F r_{ij}}{r_{ij}^4}\right] \qquad (2.16)$$

where m* is the effective mass of the electron and k_F is the Fermi wave vector.

The isotropic exchange interaction is greater in elements of higher atomic number and becomes of comparable magnitude to the ordinary dipolar interaction when the atomic number is around 40. Between identical nuclei it has no effect on the second moment but increases the fourth moment. This corresponds to a narrowing of the centre of the resonance line and an intensification of the wings, known as exchange narrowing. Between unlike nuclei the exchange interaction increases the second moment; termed exchange broadening.

2.2.5 METHOD OF MOMENTS

A calculation of the theoretical free precession signal or absorption curve for an assembly of nuclear spins requires a complete knowledge of the energy levels and has only proved possible in a few special cases(15). However, theoretical expressions for the moments of a lineshape may be obtained without prior evaluation of the eigenfunctions and eigenstates(16). The nth moment of the frequency distribution curve $f(\omega')$ is defined by

$$M_n = \int_{-\infty}^{+\infty} (\omega')^n f(\omega') d\omega \Big/ \int_{-\infty}^{+\infty} f(\omega') d\omega \qquad (2.17)$$

where $\omega' = \omega - \omega_o$. If the lineshape is symmetric about $\omega' = 0$ the odd moments vanish. In practice the wings of any experimental lineshape are relatively poorly defined yet make an increasingly large contribution to the value of the higher moments. Hence usually only the experimental second moment and sometimes the fourth moment are measured and compared to theoretical values. From Abragam, p.111, these terms are given by

$$\begin{aligned} M_2 &= -\frac{1}{\hbar^2} \mathrm{Tr}\left[\mathscr{H}_{sec}, I_x\right]^2 / \mathrm{Tr}\left[I_x^2\right] \\ M_4 &= \frac{1}{\hbar^4} \mathrm{Tr}\left[\mathscr{H}_{sec}, \left[\mathscr{H}_{sec}, I_x\right]\right]^2 / \mathrm{Tr}\left[I_x^2\right] . \end{aligned} \qquad (2.18)$$

Limiting the total perturbing Hamiltonian to its secular components ensures that the satellite lines at 0, $2\omega_o$, $3\omega_o$, etc. produced by the non-secular terms of the dipolar Hamiltonian (for example) are ignored.

For a powdered sample the second moment due to dipolar interactions between like nuclei is given by

$$M_2 = \frac{3}{5} I(I + 1)\gamma_I^4\hbar^2 \sum_{i<j}^{N} r_{ij}^{-6} \tag{2.19}$$

and between unlike nuclei

$$M_2 = \frac{4}{15}\gamma_I^2\gamma_S^2\hbar^2 S(S + 1) \sum_{i<j}^{N} r_{ij}^{-6}$$

where I and S are the resonant and non-resonant nuclei respectively, N is the total number of nuclei and r_{ij} is the inter-nuclear distance. The total second moment is given by adding these two components. This calculation can be extended to include exchange and pseudo-dipolar interactions(13).

G(t), the function describing the free precession of spins in the xy plane of the rotating frame, may be written via Abragam, p.110, as the power series

$$G(t) = G(0) \sum_{n=0}^{\infty} M_{2n} \frac{(-t)^{2n}}{2n!} \quad . \tag{2.20}$$

The even moments are given by

$$M_{2n} = (-1)^n\left(\frac{d^{2n}G(t)}{dt^{2n}}\right)_{t=0}/G(0) \quad . \tag{2.21}$$

This equation relates the even moments directly to the FID at the time origin. Experimentally, however, the initial part of the FID is obscured by the finite recovery time of the transmitter and receiver so the moments cannot normally be measured in this way.

2.3 NON-SECULAR INTERACTIONS

2.3.1 INTRODUCTION

There are a number of different processes by which a spin system can exchange energy with the lattice. Any mechanism which gives rise to fluctuating magnetic fields at a nucleus is a possible relaxation process, although often one particular mechanism is dominant and the return to equilibrium may be described by a single spin relaxation time. In liquids the relaxation processes are usually different from those in solids. Here we are primarily concerned with solid samples so of these processes we list only the dipole-dipole interaction which usually predominates.

2.3.2 DIPOLE-DIPOLE RELAXATION

Motion of nuclei through Brownian motion and diffusion changes the internal local fields. The component of the Fourier transform of the fluctuating fields at the Larmor frequency induces transitions between the Zeeman energy levels. Such a relaxation process is most efficient when the correlation time τ_c equals $1/\nu_o$. T_1 then exhibits a minimum when plotted against temperature.

2.3.3 IMPURITY RELAXATION

Any paramagnetic ions present in the sample are strongly coupled to the lattice via spin-orbit coupling. Nearby nuclei are coupled to the lattice directly via the time-dependent magnetic field of the unpaired electron of the impurity ion. However most of the nuclei are coupled only indirectly by spin diffusion through dipole-dipole interactions. The spin-lattice relaxation time resulting from such a process depends upon the nature of the impurities and the impurity concentration. Where the concentration of impurities is low, T_1 depends upon the rate of spin diffusion.

2.3.4 INTERACTION WITH CONDUCTION ELECTRONS

This mechanism is the dominant relaxation process in metals. The non-localized conduction electrons create relatively large time varying local magnetic fields at a nucleus, which can induce simultaneous but opposite flips of the electron and nuclear spins. The resulting energy difference is made up by an increase in the kinetic energy of the electrons. To a first approximation only those s character electrons near the top of the Fermi distribution are able to take part in this process. From Slichter, p.126, the relaxation rate induced by this mechanism is given by

$$\frac{1}{T_1} = \frac{64}{9}\pi^3\hbar^3\gamma_e^2\gamma_n^2\Omega^2<|\psi_k(0)|^2>_F^2\rho^2(E_F)k_BT \tag{2.22}$$

where $\rho(E_F)$ is the density of states at the Fermi surface and k_B is Boltzmann's constant. For a non-interacting electron gas

$$\chi_s = \frac{\gamma_e^2\,\hbar^2}{2}\,\rho(E_F) \quad .$$

Hence equations (2.10) and (2.22) lead to the simple Korringa relationship$^{(17)}$ between the Knight shift and spin-lattice relaxation time thus

$$T_1K^2T = \frac{\hbar}{4\pi k_B} (\frac{\gamma_e}{\gamma_n})^2 \quad . \tag{2.23}$$

This expression is only approximate because it is based on the free electron model and ignores the effect of exchange interactions between electrons on χ_s and $\rho(E_F)$. Contributions to T_1 and K other than from the direct contact term via the s character conduction electrons are also ignored. In transition metals in particular, core polarization and orbital hyperfine interactions arising from the d band electrons can be significant in determining the magnitude of both the relaxation time and the Knight shift.

The above discussion is concerned with the spin-lattice relaxation of the Zeeman Hamiltonian. The secular interactions ($\mathcal{H}_S$) of $\mathcal{H}_{int}$ also return to thermal equilibrium, although at a different rate. However, as the energy associated with spin-spin interactions is small there is usually no observable effect on T_1. Following Anderson and Redfield$^{(18)}$ we may define the two relaxation rates T_{1Z} and T_{1S} by

$$\frac{d\langle\mathcal{H}_Z\rangle}{dt} = -(\frac{\langle\mathcal{H}_Z\rangle - \langle\mathcal{H}_Z\rangle_o}{T_{1Z}}) \tag{2.24}$$

$$\frac{d\langle\mathcal{H}_S\rangle}{dt} = -(\frac{\langle\mathcal{H}_S\rangle - \langle\mathcal{H}_S\rangle_o}{T_{1S}}) \quad . \tag{2.25}$$

Strictly these two processes are not independent because equations (2.24) and (2.25) neglect the effect of spin flips induced by non-secular spin-spin interactions, which act so as to conserve the total energy $\mathcal{H}_Z + \mathcal{H}_S$. Although the spin system is brought to a common spin temperature in this way, in large fields this process is extremely slow (i.e. longer than T_{1Z}). Equations (2.24) and

(2.25) can then be assumed to apply directly.

If $\mathscr{H}_S$ is regarded as the sum of the local dipolar interaction energies between all combinations of pairs of nuclei, this energy will change if either of the spins in a single pair is relaxed. By definition the relaxation of single spins proceeds at a rate $1/T_{1Z}$, so from this simple model it follows that $T_{1S} = T_{1Z}/2$. The ratio of the spin-lattice relaxation times $\delta = T_{1Z}/T_{1S}$ is therefore equal to 2.

In practice the situation is more complicated because T_{1S} depends both upon the terms making up $\mathscr{H}_S$ and the degree of correlation between the fluctuating fields at the nuclear spin sites. If we consider $\mathscr{H}_S$ as the sum of a dipolar interaction and a scalar exchange interaction thus

$$\mathscr{H}_S = \mathscr{H}_D + \sum A_{ij}\underline{I}_i.\underline{I}_j \qquad (2.26)$$

then if the second term dominates and the conduction electrons have long wavelengths, the local fields experienced by near-neighbours are identical. Consequently the product $\underline{I}_i.\underline{I}_j$ remains constant and the relaxation time T_{1S} will be very long. Generally, however, (and particularly in light metals) the first term of equation (2.26) dominates. δ is then a measure of the correlation in the conduction electron spin system. It is given by

$$\delta = 2 + \varepsilon$$

where

$$\varepsilon = \sum_{ij} K_{ij}\left(\frac{1}{r_{ij}^6}\right) / \sum_{ij} \left(\frac{1}{r_{ij}^6}\right)$$

and K_{ij} is a measure of the degree of electron correlation between sites r_i and r_j as calculated by Wolff(19). It includes consideration of the electron wavelength as well as the amplitude of electron exchange effects. For an ideal non-interacting gas

$$K_{ij} = \sin^2(k_F r_{ij})/(k_F r_{ij})^2 \tag{2.27}$$

where k_F is the radius of the Fermi surface. Assuming one electron per atom this yields a value for ε of approximately 0.05(18) whereas for complete spatial correlation ε is unity.

In addition we note that there may also be a quadrupole contribution to $\mathscr{H}_S$. If the quadrupole interactions are small (e.g. arising from imperfections in a cubic lattice structure) and axially symmetric, the quadrupole reservoir has a relaxation time given by $T_{1Z}/3$(18). Hence any experimental estimate of δ is sensitive to quadrupole effects as well as spin correlation in the electronic system.

2.3.5 QUADRUPOLE RELAXATION

For nuclei with spin greater than ½ the nuclear quadrupole moment can couple to local field gradients due to molecular motion, lattice vibrations or (in the case of metals) the non-localized conduction electrons. In metals the quadrupole relaxation rate is usually negligible but in ionic crystals quadrupole coupling with the lattice phonons proves to be the dominant relaxation mechanism. The transient departures from cubic symmetry caused by the vibrations of the lattice result in fluctuating electric field gradients at the nuclei which interact with the nuclear quadrupole moments to produce transitions within the spin levels of the nuclei. The vibrational modes in a solid may be assumed to occupy a Debye spectrum, the Debye frequency being defined by $h\nu_D = k\theta_D$. There are three suggested phonon relaxation processes,

(i) Single Phonon. Transitions induced between the nuclear spin states correspond to the creation or destruction of a single phonon. Only these phonons with energy $h\nu_p = h\nu_o$ can participate. However $\nu_o << \nu_D$, so there are very few phonons which fulfil this condition and such a process is not an efficient relaxation mechanism. As phonons obey Bose-Einstein statistics and $h\nu_o << kT$ the number of phonons with energy $h\nu_o$ is proportional to the absolute temperature. The relaxation probability depends upon the number of vibrational modes with frequency ν_o. Hence $1/T_1 \propto \nu_o^2 T$.

(ii) Four Phonon. A second order process has been suggested(20) by which two phonons are created and two destroyed, the energy difference being made up by the lattice transition. This mechanism predicts a T^{-4} dependence of T_1 but although it was expected to dominate at high temperatures it has never been observed experimentally. Indeed, a more recent calculation(21) has shown that such a process does not in fact give rise to any net transition between nuclear spin levels, and consequently does not contribute to the overall T_1.

(iii) Two Phonon (Raman). This process is far more efficient than the single phonon because any phonon in the Debye spectrum can participate. A phonon is scattered inelastically at a nucleus so an induced transition between spin states is accompanied by a corresponding change in the phonon energy. Although the relaxation rate is independent of the resonance frequency it has the following temperature dependence

$$T_1 \propto T^{-2} \quad \text{for} \quad T \geq \theta_D$$
$$T_1 \propto T^{-7} \quad \text{for} \quad T < 0.02\theta_D \ .$$

Such a relaxation process was first examined in ionic crystals of the NaCl type by Van Kranendonk$^{(22)}$, who assumed that the lattice could be described by an array of point charges located at the lattice sites. The theory was extended to lattices of the zinc blende type by Mieher$^{(23)}$ with the result that the quadrupolar transition probabilities between Zeeman levels n and m are given by

$$W_{nm} = c|Q_{nm}|^2 T^{*2} E(T^*) E_{n-m}(\infty) \qquad (2.28)$$

where

$$c = \sqrt{3}/(8\pi d^2 v^3 a^3) \ .$$

d is the density, v is the velocity of sound in the crystal, and a is the lattice constant; Q_{nm} is the matrix element of the quadrupolar operator; $E_{n-m}(\infty)$ is a function describing the angular dependence of the transition probabilities and includes details of the lattice; T* is the reduced temperature T/θ_D; E(T*) is a function computed by Van Kranendonk which increases from zero for T* = 0 to unity when $T > \theta_D$.

With the assumption that at any time the spin system can be described by a spin temperature, T_1 is given by the general relationship

$$\frac{1}{T_1} = \tfrac{1}{2}\Big[\sum_{n,m} (E_n - E_m)^2 W_{nm}\Big] \Big/ \sum_n E_n^2$$

where E_n are the Zeeman energy levels ($-\gamma\hbar H_o n$). This leads to the expression

$$\frac{1}{T_1} = \frac{1}{40} f(I)(eQ)^2 cT^{*2}E(T^*)\left|E_1(\infty) + 4E_2(\infty)\right|$$

with

$$f(I) = \frac{2I + 3}{I^2(2I - 1)}.$$

Such an equation is not specific to zinc blende crystal lattices because all the structure parameters are included in the terms $cE_{n-m}(\infty)$. From Mieher's calculated values of $E_{\pm 1}(\infty)$ and $E_{\pm 2}(\infty)$ an isotropic relaxation time is predicted, which is given by

$$\frac{1}{T_1} = Af(I)\left|\frac{e^2\gamma Q}{r^5}\right|^2 T^{*2}E(T^*) \tag{2.29}$$

where

$$A = \frac{3305c}{40} = \frac{1983}{\pi d^2 v^3 a^2} .$$

The term ($e^2\gamma Q/r^5$) is a measure of the strength of the electric quadrupole interaction between nuclei, r being the nearest-neighbour separation and γ a scalar.

The weakness of the above expression is that any indirect contributions to the nulcear quadrupole coupling are included only through the multiplying factor γ. In ionic crystals the electron charge cloud surrounding each nucleus is distorted from spherical symmetry by the electric field gradient arising from the other ions. This leads to an additional contribution to the nuclear quadrupole coupling, the magnitude of which can be estimated from the value of the Sternheimer anti-shielding factor(3,24) for the particular ion. However, compounds with a zinc blende type lattice structure are strongly covalent. Consequently, any numerical estimate of γ also has to include an empirical factor relating the covalent lattice to the point charge model.

In the alkali halides detailed consideration of the effects of anti-shielding(25) and covalent bonding(26) has improved the quantitative agreement with experiment, as have calculations on the effect of overlap distortion of the ionic electron distribution(27). These extensions of the relaxation theory differ only in the mechanisms, which produce the field gradient at the nucleus: although the magnitude of the relaxation time is altered, Van Kranendonk's predicted temperature dependence is unaffected.

The ionic model has been further extended to include the interaction between the nuclear quadrupole moment and the electric field gradients due to the oscillating electric dipoles associated with optical modes of vibration(28). Modification of the Debye approximation to include this effect alters the absolute magnitude of the spin-lattice coupling for any ion(29.30). However significant departures from the form of Van Kranendonk's function $T^{*2}E(T^*)$ have only been found at low temperatures(30,31). Generally, experiments on the alkali halides(29-32) and several III-V compounds(23) have demonstrated that Van Kranendonk's model still provides a good account of the temperature dependence of the relaxation time. This behaviour reflects the fact that the Raman relaxation processes involve an integrated effect of the lattice vibrational spectrum. As a result the temperature dependence of the relaxation rate is relatively insensitive to the precise form of the phonon distribution function.

CHAPTER 3

NARROWING THE NUCLEAR RESONANCE SPECTRUM BY MACROSCOPIC SAMPLE ROTATION

3.1 INTRODUCTION

In Chapter 2 the various line-broadening interactions which exist in solids, and metals in particular, have been considered. In many liquids and solids the situation is different: motion of the nuclear spins averages out the secular line broadening mechanism. The internal motion may be described by a correlation function $f(\nu)$ with a mean correlation time τ_c. If τ_c is short and less than T_2 (the characteristic time describing the dephasing of spins in the rotating frame) the spin vectors will execute a random walk in the rotating frame and only slowly accumulate a phase difference relative to the mean resonance frequency ν_o. In the extreme case the secular interactions become so inefficient that the width of the resonance spectrum is determined by the homogeneity of the magnetic field across the sample and lifetime broadening.

The above discussion is concerned with microscopic motion within a particular sample. Similar arguments apply when studying the effect of a macroscopic rotation of the sample about a unique axis, but there are a few important differences. Unlike random internal motion, macroscopic rotation only causes averaging over the plane of rotation and not over inter-nuclear distances. Macroscopic motion is a very slow process by molecular standards and involves a single frequency of motion. Although Fourier analysis gives rise to a series of spinning sidebands, no modulation component is present at the Larmor frequency and no spin-lattice relaxation processes are introduced directly. Nevertheless spin diffusion is rendered more inefficient(33,34) and hence also T_1 relaxation via paramagnetic impurities. Rotation at a frequency corresponding to the chemical shift between two resonance lines has been shown(35) to introduce a cross-relaxation mechanism between nuclear spins which alters the spin-lattice relaxation time.

In studying the effect of motion on the nuclear spin system it is convenient to divide the secular Hamiltonian into two parts, a time-average component $\bar{\mathcal{H}}$ and a time-dependent component with zero mean $\mathcal{H}^{1}(t)$. Although the Zeeman interaction is unaffected by motion the various line-broadening interactions can be similarly treated. Hence

$$\mathcal{H} = \mathcal{H}_Z + \bar{\mathcal{H}}_D + \bar{\mathcal{H}}_Q + \bar{\mathcal{H}}_S + \bar{\mathcal{H}}_J$$

and

$$\mathcal{H}^{1}(t) = \mathcal{H}^{1}_D(t) + \mathcal{H}^{1}_Q(t) + \mathcal{H}^{1}_S(t) + \mathcal{H}^{1}_J(t) \quad .$$

This division is only properly applicable to those cases where the motion is rapid, i.e. $\tau_c < T_2$. Therefore the motional averaging processes considered below are subject to this criterion.

3.2 ISOTROPIC MOTION

We first consider the effect of rapid isotropic reorientation on the general tensor interaction $\underline{A}.\underline{T}.\underline{B}$ where $\underline{A}$ and $\underline{B}$ are motionally invariant spin operators and $\underline{T}$ is a second rank coupling tensor. The time average of this interaction is given by

$$\overline{\underline{A}.\underline{T}.\underline{B}} = \underline{A}.\overline{\underline{T}}.\underline{B} \quad .$$

It is a general property that $\underline{T}$ can be divided into a symmetric tensor $\underline{T}^*$ and an antisymmetric tensor $\underline{T}^\dagger$. If T_{pp} are the principal values of the tensor $\underline{T}^*$ and $\lambda_{p\ell}$ are the direction cosines of the principal axes (p = 1,2,3) with respect to the laboratory reference frame (ℓ,m,n) then

$$T^*_{\ell m} = \sum_{p=1,2,3} \lambda_{p\ell}\lambda_{pm}T_{pp} \tag{3.1}$$

where subscript ℓm is used to imply summation over all axes, ℓ, m and n. Under the condition of rapid isotropic reorientation the time dependence of $\underline{T}$ only arises out of the motion of the principal axes, the principal values remaining constant. The isotropic average of $T^*_{\ell m}$ is given by

$$\begin{aligned} T^*_{\ell m} &= \sum_p \overline{\lambda_{p\ell}\lambda_{pm}}\, T_{pp} \\ &= \sum_p \frac{1}{3}\, \delta_{\ell m}\, T_{pp} \quad . \end{aligned}$$

Hence

$$\overline{\underline{T}}^* = \frac{1}{3}\,\mathrm{Tr}\,\underline{T}^* \quad . \tag{3.2}$$

The antisymmetric component $T^\dagger$ is given by

$$T^\dagger_{\ell m} = \sum_{a,b} \lambda_{a\ell}\lambda_{bm}\, T^\dagger_{ab} \tag{3.3}$$

where a,b refers to any pair of axes of a convenient co-ordinate system in the molecule. This expression can be rewritten as

$$T^{\dagger}_{\ell m} = \sum_{a>b} (\lambda_{a\ell}\lambda_{bm} - \lambda_{am}\lambda_{b\ell})T^{\dagger}_{ab} \quad .$$

Isotropic averaging results in there being no preferred direction so that $\overline{T}^{\dagger}_{\ell m} = 0$ and as a result

$$\underline{A}.\overline{\underline{T}}.\underline{B} = \frac{1}{3}\,\mathrm{Tr}\,\underline{T}\;\underline{A}.\underline{B} \quad . \qquad (3.4)$$

Because intermolecular interactions are subject to diffusional motion as well as rotation in practice the inter-nuclear distances change, causing the principal values of I to vary with time. This results in an even more complete averaging process.

It has been shown that rapid isotropic reorientation of the nuclear spins averages out tensor interactions between spins to scalar values. Because the quantities $Q_{\alpha\beta}$ of equation (2.4) are only functions of spin operators and not of any angular factors, secular quadrupole interactions are similarly averaged. Thus all secular line-broadening interactions represented by traceless tensors are reduced to zero.

We now consider the effect of macroscopic sample rotation following the approach of previous examinations(36,37).

3.3 THE DIPOLAR INTERACTION

The truncated form of the dipolar interaction is given by

$$\mathcal{H}^{T}_{D} = \tfrac{1}{2}\sum_{i<j}^{N} \gamma_i\gamma_j \frac{\hbar^2}{r^3_{ij}}[\underline{I}_i.\underline{I}_j - 3I_{iz}I_{jz}](3\cos^2\theta_{ij} - 1) \quad . \qquad (3.5)$$

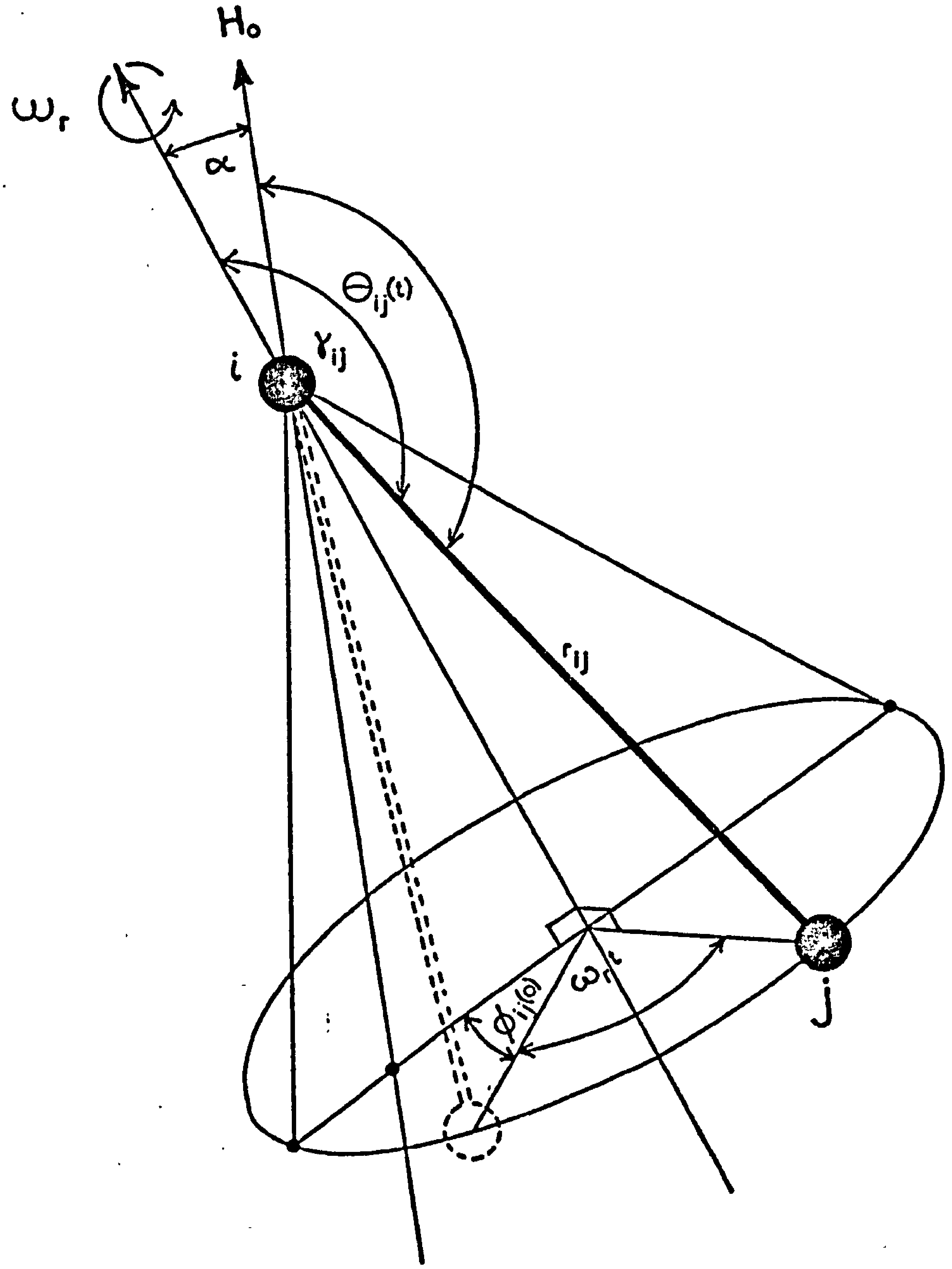

FIGURE 3.1. : Co-ordinate system for a rotating pair of nuclear spins

Motion of each nuclear pair imparts a time dependence to θ_{ij} leaving the other terms of this expression unaffected. For a macroscopic rotation at angular velocity ω_r about an axis inclined at an angle α to the applied magnetic field (Figure 3.1) it can be shown that

$$\cos\theta_{ij}(t) = \cos\alpha\cos\gamma_{ij} + \sin\alpha\sin\gamma_{ij}\cos(\omega_r t + \phi_{ij}) \tag{3.6}$$

where γ_{ij} is the angle between the rotation axis and $\underline{r}_{ij}$. If $\cos^2\theta_{ij}(t)$ is expressed as the sum of a time-averaged part $\overline{\cos^2\theta_{ij}(t)}$ and a time-dependent part $\cos^{2\prime}\theta_{ij}(t)$ then

$$\begin{aligned}\overline{\cos^2\theta_{ij}(t)} &= \cos^2\alpha\cos^2\gamma + \tfrac{1}{2}\sin^2\alpha\sin^2\gamma \\ &= \frac{1}{6}(3\cos^2\alpha - 1)(3\cos^2\gamma - 1) + \frac{1}{3}\end{aligned} \tag{3.7}$$

and

$$\begin{aligned}\cos^{2\prime}\theta_{ij}(t) &= \tfrac{1}{2}\sin^2\gamma_{ij}\sin^2\alpha\cos 2(\omega_r t + \phi_{ij}) \\ &\quad + \tfrac{1}{2}\sin 2\alpha\sin 2\gamma_{ij}\cos(\omega_r t + \phi_{ij}) \quad .\end{aligned} \tag{3.8}$$

Upon substitution into equation (3.5) the time-averaged Hamiltonian is given by

$$\bar{\mathcal{H}}_D = \frac{\hbar^2}{4}(3\cos^2\alpha - 1)\sum_{i<j}\frac{\gamma_i\gamma_j}{r_{ij}^3}[\underline{I}_i\cdot\underline{I}_j - 3I_{iz}I_{jz}](3\cos^2\gamma_{ij} - 1) \quad . \tag{3.9}$$

Similarly the time-dependent Hamiltonian is given by

$$\mathscr{H}_D^{I\prime}(t) = \frac{3\hbar^2 \sin^2\alpha}{4} \sum_{i<j} \frac{\gamma_i\gamma_j}{r_{ij}^3}[\underline{I}_i\cdot\underline{I}_j - 3I_{iz}I_{jz}]\sin^2\gamma_{ij}\cos 2(\omega_r t + \phi_{ij})$$

$$+ \frac{3\hbar^2 \sin 2\alpha}{4} \sum_{i<j} \frac{\gamma_i\gamma_j}{r_{ij}^3}[\underline{I}_i\cdot\underline{I}_j - 3I_{iz}I_{jz}]\sin 2\gamma_{ij}\cos(\omega_r t + \phi_{ij})$$

(3.10)

The time-averaged truncated dipolar Hamiltonian can be seen to be of exactly the same form as equation (3.5) but reduced by a factor $(3 \cos^2\alpha - 1)/2$. It follows that when α equals the magic angle, $\cos^{-1}(1/\sqrt{3})$, this term is reduced to zero. When α is set at 90° the effective dipolar coupling between spins is reduced by a half.

The time-dependent Hamiltonian consists of a term periodic in ω_r and a second term periodic in $2\omega_r$. These give rise to the characteristic satellite lines which are observed either side of the central resonance spectrum. The first term disappears when α equals 90° so the satellite lines then only occur at multiples of $2\omega_r$.

The above results apply to powders as well as single crystals, and have been shown(38) to be equally applicable to spectra that are already partially narrowed by restricted internal motion such as molecular reorientation.

3.4 THE QUADRUPOLE INTERACTION

In equation (2.6) the first order quadrupole Hamiltonian in a solid was shown to be of the form

$$\mathscr{H}_Q = \frac{e^2qQ}{4I(2I - 1)} \left(\frac{3 \cos^2\theta - 1}{2}\right)\left[3m^2 - I(I + 1)\right]$$

where θ is the angle between the principal reference frame and H_o.

Upon macroscopic rotation $\mathscr{H}_Q$ becomes dependent upon the time average $\overline{(3\cos^2\theta - 1)}$. From equation (3.7)

$$\overline{(3\cos^2\theta - 1)} = \tfrac{1}{2}(1 - 3\cos^2\alpha)(1 - 3\cos^2\gamma) .$$

Therefore when α is equal to the magic angle the quadrupole Hamiltonian is averaged to zero. Although this result is dependent upon the condition of axial symmetry stated in Section 2.2.2, Cunningham and Day(39) have applied a more rigorous analysis to the problem and find that the interaction is reduced to zero whatever the value of η.

3.5 FREQUENCY SHIFT MECHANISMS

From Section 2.2.3 both the chemical shift and Knight shift interactions can be written in the form

$$\mathscr{H}_S = \sum_j \gamma_j \hbar H_o I_{jz} \sigma_{jzz} .$$

In the principal reference frame

$$\sigma_{jzz} = \sum_{p=1,2,3} \lambda_{pz}^2 \sigma_{pp} \qquad (3.11)$$

where λ_{pz} are the direction cosines of the principal axes with respect to H_o and σ_{pp} are the principal values.

Macroscopic sample rotation about an axis at an angle α to H_o and at angles β_p to the principal axes results in

$$\lambda_{pz}(t) = \cos\alpha \cos\beta_p + \sin\alpha \sin\beta_p \cos(\omega_r t + \phi_p(0)) \qquad (3.12)$$

where $\phi_p(0)$ is the azimuthal angle of the principal axis p at $t = 0$. The resulting time-averaged Hamiltonian is given by

$$\bar{\mathscr{H}}_S = \hbar H_o \sum_j \gamma_j I_{jz}\left[\tfrac{1}{2}\sin^2\alpha \operatorname{Tr} \underline{\sigma}_j + \tfrac{1}{2}(3\cos^2\alpha - 1)\sum_p \sigma_{jp}\cos^2\beta_{jp}\right]. \qquad (3.13)$$

The time-dependent term $\mathscr{H}'_S(t)$ consists of two terms periodic in ω_r and $2\omega_r$ which again give rise to rotational sidebands either side of ω_o. When $\alpha = \cos^{-1}(1/\sqrt{3})$ the time-averaged Hamiltonian reduces to

$$\bar{\mathscr{H}}_S = \hbar H_o \sum_j [\gamma_j I_{jz} \operatorname{Tr} \sigma_j/3] \qquad (3.14)$$

as is the case for liquids. In this way anisotropic Knight shift and chemical shift interactions may be averaged out. The corresponding line-broadening effect present in polycrystalline samples is therefore reduced to zero.

3.6 INDIRECT SPIN-SPIN INTERACTION

The indirect spin-spin interaction Hamiltonian is given by

$$\mathscr{H}_J = \sum_{i<j}^{N} \hbar \underline{I}_i \cdot \underline{J}_{ij} \cdot \underline{I}_j \quad .$$

In metals the second rank tensor $\underline{J}$ may be separated into a scalar J and a symmetric traceless tensor $\underline{J}^*$ (see Section 2.2.4). Following equation (3.1) the symmetric tensor interaction is given by

$$J^{*}_{ij\ell m} I_{i\ell} I_{jm} = \sum_{p=1,2,3} \lambda_{ijp\ell} \lambda_{ijpm} T_{ijpp} I_{i\ell} I_{jm} \,. \tag{3.15}$$

Summation over repeated suffixes ℓ, m and n is again implied. The expression may be truncated in a similar way to the normal dipolar interaction by omitting non-secular spin terms which do not contribute directly to the observed spectrum. Then

$$J^{*T}_{ij\ell m} = -\tfrac{1}{2} J_{ij3}\left[(3\lambda^2_{ij3n} - 1) + \eta_{ij}(\lambda^2_{ij2n} - \lambda^2_{ij1n})\right] \times (\underline{I}_i\underline{I}_j - 3I_{iz}I_{jz}) \tag{3.16}$$

where the asymmetry parameter η_{ij} is defined as

$$\eta_{ij} = (J_{ij2} - J_{ij1})/J_{ij3} \quad \text{with } J_3 > J_2 > J_1 \,.$$

The direction cosines λ_{pn} become time-dependent when the sample is rotated such that as equation (3.7)

$$\overline{\lambda^2_{ijpn}} = \frac{1}{6}(3\cos^2\alpha - 1)(3\cos^2\beta_{ijp} - 1) + \frac{1}{3}$$

where β_{ijp} are the angles between the principal axes of $\underline{J}^*$ and the axis of rotation. When α is set to the magic angle, $\overline{\lambda^2_{ijpn}}$ is 1/3 for all three values of p and the time-averaged tensor $\overline{\underline{J}}^*$ is reduced to zero. Hence rapid rotation about the magic angle effectively transfers the anisotropic part of the indirect coupling interaction to the spinning sidebands in exactly the same manner as the normal dipolar interaction. The isotropic scalar term J is of course unaffected by rotation.

3.7 THE EFFECT OF ROTATION ON THE NUCLEAR LINESHAPE

We have shown that sample rotation at the magic angle averages out internal line-broadening interactions, although this result does presuppose a sufficiently rapid rotation rate. We now consider the form of the resulting spectrum.

The Hamiltonian describing the nuclear spin system may be written as

$$\mathcal{H} = \mathcal{H}_Z + \mathcal{H}_p + \mathcal{H}_m$$

where $\mathcal{H}_p$ is the sum of the secular perturbations and $\mathcal{H}_m$ is the motional Hamiltonian representing the kinetic energy. From equation (2.18) the second moment of the nuclear lineshape about the centre frequency is given by

$$M_2 = \frac{-\mathrm{Tr}\left[\mathcal{H}_p + \mathcal{H}_m, I_x\right]^2}{\hbar^2\ \mathrm{Tr}\left[I_x\right]^2} .$$

In the absence of $\mathcal{H}_p$, the orientation of the nuclear spins in the external magnetic field is independent of position or any relative motion between spins. Consequently $\mathcal{H}_m$ commutes with I_x. The second moment of any resonance spectrum is therefore unaffected by any sort of motion. However, as $\mathcal{H}_m$ does not commute with $\mathcal{H}_p$, it can be shown(40) that the fourth moment is increased and the lineshape altered in such a way as to narrow the central component and enhance the wings.

Detailed calculations for the cases of both uniformly rotating and randomly reorientating nuclear pairs confirm the above arguments(41,42). In liquids rapid random reorientation can be thought of as forming a continuum of sidebands which become unobservably weak; hence resulting in the characteristic Lorentzian lineshape. For macroscopic sample rotation at the magic angle the central component of the absorption spectrum is flanked by a series of sidebands at integer multiples of ν_r. As the rotation rate is increased these sidebands move further out and become less intense. When ν_r is greater than the linewidth the intensity of the satellites falls as ν_r^{-2n} for the nth satellite, thus preserving the total second moment. Both the central component and the satellites have a finite width which decreases with increasing spinning frequency(43,44).

Accurate adjustment of the magic angle is an important criterion in achieving a minimum linewidth. A reduction of the dipolar linewidth to 1% of its original value requires that the magic angle is set to an accuracy of better than half a degree. Such an adjustment can best be performed empirically by direct observation of the FID from the rotated sample. With the assumption that there is no antisymmetric component of the spin-spin interaction the fully resolved central spectrum for any solid rotated about the magic axis is determined by the Hamiltonian

$$\mathcal{H} = -\hbar \sum_j \gamma_j (1 - \sigma) I_{iz} H_o + \sum_{ij} J_{ij} \underline{I}_i \cdot \underline{I}_j \ , \qquad (3.17)$$

the same as that relating to fluids in high resolution NMR.

In practice complete resolution of the central line from the first spinning sidebands flanking it either side is dependent upon the frequency of rotation. The faster the sample is spun the greater likelihood there is of attaining some rotationally invariant limit. There have been several suggestions as to the manner in which the residual dipolar broadening of the central spectrum varies with rotation rate(33,34,38,45,46). However experimental observations are inconsistent with all of the simple relationships predicted. Undoubtedly the precise form of the dependence is determined by the line-broadening interactions present in the sample and hence the shape of the static absorption spectrum. Generally the experimental lineshape narrows slowly until the rotation frequency is about equal to the static half-width of the absorption curve. It then narrows rapidly and later more slowly until a rotationally invariant limit is reached.

We remark at this point that it was shown in Section 3.4 that first order quadrupole broadening can be removed by rotation about the magic angle. However, the rotation rates required for this effect are normally considerably in excess of those which can be achieved experimentally. If the quadrupole interaction is due to imperfections in otherwise cubic solids it results in long tails on the frequency spectrum which do not appreciably affect the linewidth. Dipolar broadening may then still be narrowed by magic angle rotation, even though the quadrupolar broadening remains unaffected.

In the limit any residual linewidth besides depending upon $\overline{\mathcal{H}}$ is subject to the normal field inhomogeneity and T_1 broadening mechanisms. Rapid rotation serves to average out part of the contribution from field inhomogeneities but only in a plane perpendicular to the axis of rotation. The rotor systems employed here could only be accommodated in a large magnet pole gap so the field gradients along the axis of rotation could be significant in determining the width of the narrowed central lineshape.

CHAPTER 4

EXPERIMENTAL ROTATION SYSTEMS

4.1 INTRODUCTION

The technique of magic angle sample rotation has been used to observe fine structure in the NMR spectra of materials, which is otherwise obscured by dipolar broadening(47). The rotation rates employed have to be approximately the same as the static linewidth, and complete removal of the tensor broadening interactions requires rates considerably in excess of this value. To this end it has been necessary to use systems of rotation which are capable of extremely high spinning frequencies. The highest rotation rate ever recorded is 1.5 MHz, using a fine metallic wire supported magnetically(48). Obviously similar forms of suspension are excluded by the limitations imposed by NMR, so small gas turbine systems are normally employed.

In the course of the work reported here three different such turbine systems were constructed and used, which we shall call the conical, foil bearing and Prague systems. Although the conical rotors(19) have been developed in the laboratory over a period of some years, the foil bearing rotors represented a new approach to the high speed rotation technique. Some time was spent on the development and successful adaptation of these rotors for use in conjunction with NMR measurements. The third type of gas turbine was constructed following the design used by a group of experimentalists in Prague(50). A study of this type of turbine showed that it apparently offered no advantages over the other rotor systems. Because of the non-trivial nature of the problem we include below a short discussion of some of the criteria relevant to the design of gas turbine systems for use in conjunction with NMR.

4.2 ASPECTS OF ROTOR DESIGN

4.2.1 MATERIALS

The materials from which the rotors and the surrounding rig are constructed must not upset the NMR measurements either by affecting the homogeneity of the magnetic field or by causing stray pick-up in the detection coil. The rotor itself cannot be made from any metal because the speed of rotation in the external field is then severely restricted by induced eddy currents.

4.2.2 SIZE

The size of the complete rotor system is limited by the magnet gap. However the sample volume must be such that a reasonable signal-to-noise figure can be attained with the NMR equipment available. Although this condition varies greatly depending upon the NMR sensitivity of the particular nuclei under investigation most turbine systems used are capable of carrying a sample of volume between 0.1 and 1.0 cc.

The sensitivity of the system is considerably enhanced by winding the detection coil co-axially about the rotor. The filling factor is maximized in this way but it should be remembered that, if the same coil is used in the transmitter circuit, the H_1 field produced is not perpendicular to H_o.

4.2.3 STRESSES

The rotor has to withstand the large internal stresses generated by rapid rotation. Considering the simplified case of an infinitely long hollow tube (and hence ignoring axial stresses) the radial and tangential stresses are given by(51)

$$\sigma_r = \rho\omega_r^2 \frac{3+\mu}{8} \left[a^2 + b^2 - r^2 - \frac{a^2b^2}{r^2}\right]$$

$$\sigma_t = \rho\omega_r^2 \frac{3+\mu}{8} \left[a^2 + b^2 - \frac{1-3\mu}{3+\mu} r^2 + \frac{a^2b^2}{r^2}\right] \tag{4.1}$$

where ω_r is the angular velocity, μ is the Poisson ratio and ρ is the density of the rotor material; a and b are the internal and external radii respectively. Therefore the maximum tangential stress acts at the inner edge of the tube. The radial stress is zero at the surfaces and has a maximum value at a radius given by $\sqrt{ab}$.

For the case of a solid rod a is zero and the maximum stresses act at the centre where

$$\sigma_t = \sigma_r = \rho b^2 \omega_r^2 \frac{3+\mu}{8} \quad . \tag{4.2}$$

These stresses are proportional to the squares of both the external radius and the spinning frequency.

4.2.4 THE PROBLEM OF WHIRL AND ROTOR BALANCE(52)

Probably the simplest rotor system would take the form of a cylinder supported by one or more journal bearings, but most journal bearings suffer from instabilities. There is usually some sort of resonant response when the spinning frequency corresponds to the natural frequency of the rotor in its bearing constraints. However, very often the critical factor is a vibration called 'half-speed whirl'. Whirling arises because when a rotating cylinder is displaced from its equilibrium position the restoring force from the bearing does not act straight back towards the centre but at an angle towards the direction of rotation. Half-speed whirl occurs at a frequency exactly half the rotor running speed. Although the amplitude of the whirling motion may be small, this vibration is sharply resonant where the natural frequency of the rotor is close to this value. Then it invariably leads to rapid failure of the bearing supports.

Any imbalance of the rotor gives rise to an out-of-balance disturbance at the rotation frequency. Although machining tolerances are important, the inclusion of a sample can often cause a drastic rotor imbalance. The most reliable systems are those in which these factors are not critical.

4.2.5 THE DRIVING JETS

Assuming that a rotor is efficiently supported, its rotation speed is determined by the velocity of the gas passing through the driving jets. Using simple convergent nozzles the maximum exit velocity is limited to the sonic velocity of the gas in the region of the nozzle exit(53). Higher rotation speeds may in principle be achieved by using supersonic gas nozzles, but the design and manufacture of these involves advanced engineering concepts.

The problem may also be overcome by using a propelling gas in which the velocity of sound is much higher. The maximum velocity of the rotor is then determined by other factors - usually mechanical - before the sonic limit is reached.

4.3 THE CONICAL ROTOR SYSTEM

4.3.1 DESCRIPTION

This rotor system is based on the type originally described by Henriot and Huguenard(54) and by Beams(55,56). The conical-shaped rotor base sits in a stator in which there are a series of jets. The gas passing through these jets serves both to lift the rotor off the base stator and to drive it round. Because of the Bernoulli forces the rotor does not fly out of the stator, but is supported by a cushion of air.

The present system, shown in Figure 4.1, is a compromise between sample size and the higher rotation speeds possible with smaller diameter rotors. The rotors have a series of 20 flutes cut to a depth of 0.030" at an angle of approximately 30° to the vertical axis. In the past much effort has gone into optimizing the number, position and size of the jets in the stator(57,58). The most efficient combination of rotor and stator has been found to vary with each individual rotor. Generally the best results were achieved here using stators with 23 0.015" diameter jets set in a single ring. Each jet was drilled at an angle of 60° to a vertical line through the apex of the stator and in a plane tangential to the rotor flutes at each point.

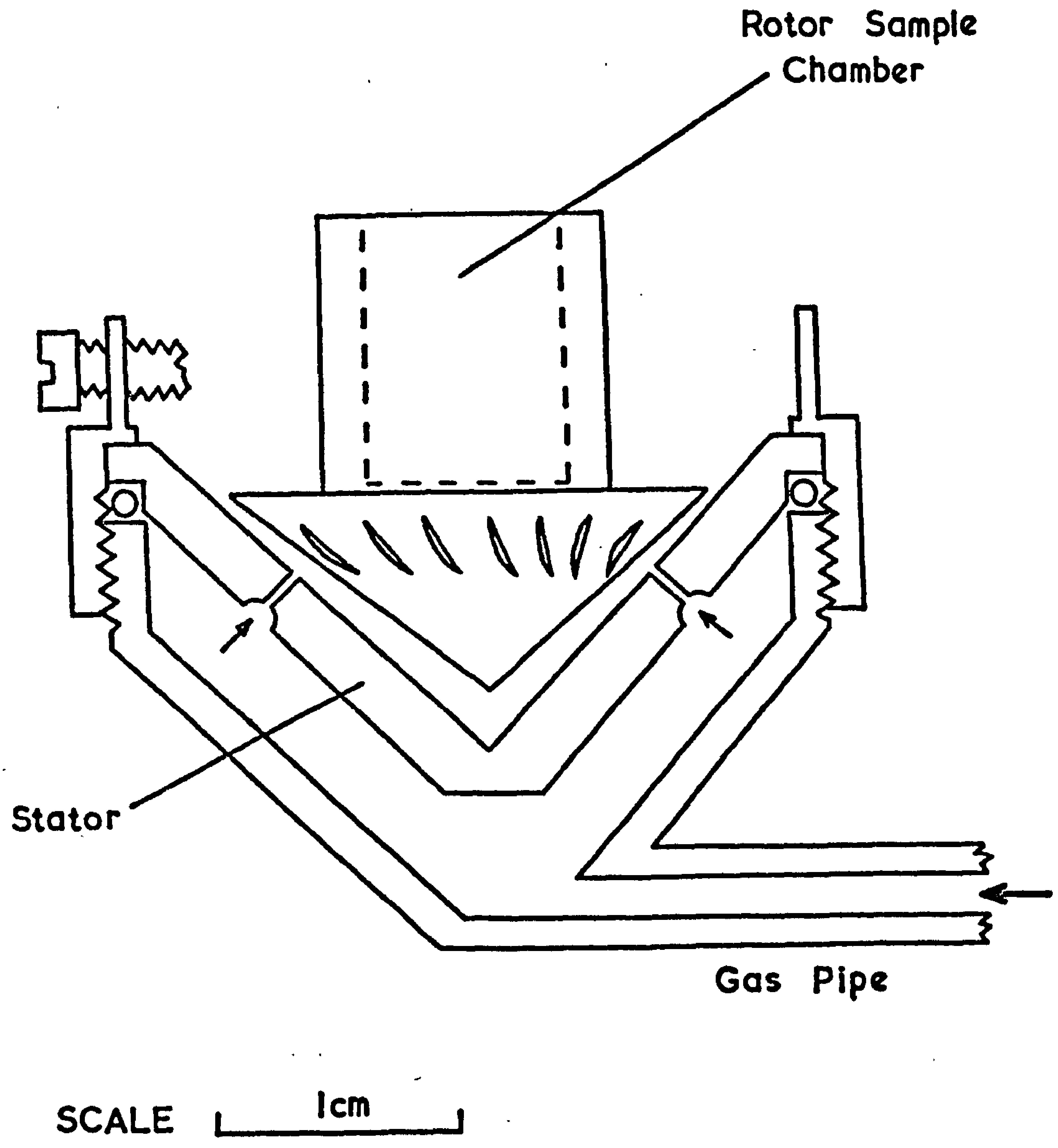

FIGURE 4.1 : The conical rotor system

4.3.2 EXPERIMENTAL DETAILS

At a spinning frequency of 5 kHz the velocity of the rotor flutes is close to the velocity of sound in air. Both hydrogen and helium are capable of propelling rotors to considerably greater speeds, but because sparks are often produced when a spinning rotor touches the metal stator, helium is the gas used on the grounds of safety. By using a compressor it would have been possible to collect and recycle helium after use(59). However, in practice such an arrangement was not found to be very satisfactory because the gas soon became 'dirty'. With the pulse spectrometer used in this work it was only necessary to maintain rotation frequencies for relatively short periods - particularly for metals with their short spin-lattice relaxation times. Helium could then reasonably be taken directly from a cylinder and vented to the atmosphere. Unfortunately it proved extremely difficult to start the rotors spinning with helium as the driving gas. The reason for this was unclear, but attributed to the low gas density, the large masses of the metallic specimens and the lack of dynamic balancing. Figure 4.2 shows the rotation rates that have been achieved by a solid nylon rotor when propelled by compressed air and helium.

The conical rotors start more easily with their axes of rotation vertical, but will rotate about any direction - even upside down. Consequently a normal electromagnet was employed in this work and the rotors spun about an axis inclined at 54^{o} 44' to the horizontal magnetic field.

The single radiofrequency coils were wound on nylon formers and held in position about the rotor superstructure by screws

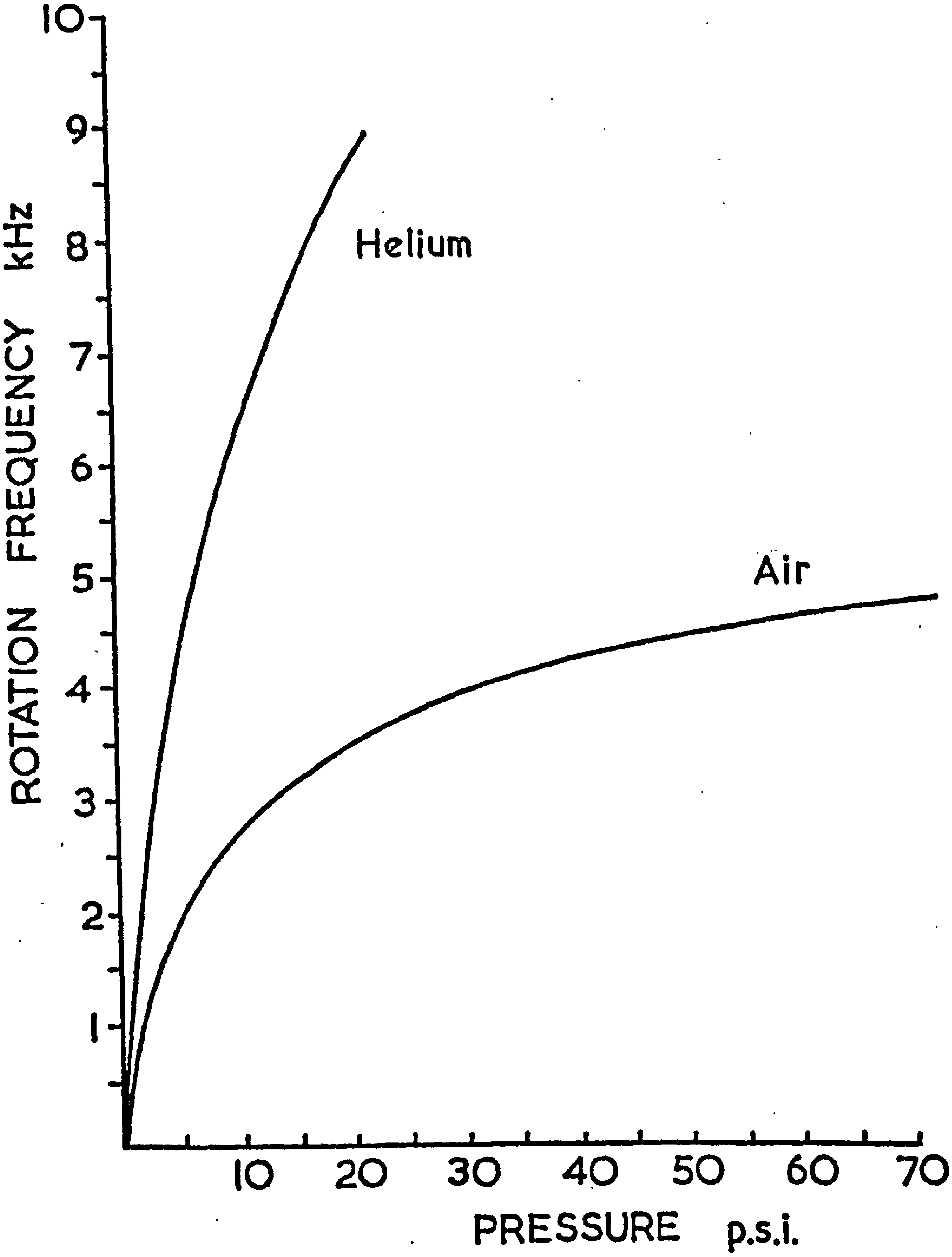

FIGURE 4.2. : Rotation rates attained by a solid nylon conical rotor when driven by air and helium

through the stator clamping ring. The presence of the coils affected the running characteristics of a particular rotor. Using coils such that the mean clearance between the rotor and former was approximately 1 mm, the rotors were most stable when running very close to the coil at one point.

For test purposes the spinning rate was determined by using a Dawes 1205A high frequency stroboscope, but this was not possible when the rotor was enclosed in the spectrometer probe assembly. The rotors emit a characteristic note at the frequency of rotation. Therefore in the audio range the rotation frequency could be measured by listening for beats against the note emitted by a loudspeaker coupled to an audio oscillator. Beyond the frequency range 2-6 kHz this technique became inconvenient because of the difficulty of detecting beats by ear. At higher speeds the rotation rate could be determined either by direct observation of the FID or by a corresponding measurement of the separation between spinning sidebands of the transformed lineshape.

4.3.3 ROTOR MATERIALS

Solid nylon rotors have been run up to speeds of 10 kHz, but the strength of the rotors is substantially reduced by the machining of the sample chamber. At speeds above 4 kHz there is considerable radial growth of the walls of the sample chamber and at higher speeds they soon burst. To-date the use of other commercially available materials (e.g. brands of tufnol, reinforced nylon, etc.) has failed to result in any significant improvement, although some success has been achieved in the past by using a glass cloth wrap(59).

The rotors used in this work were manufactured from glass fibre rods produced in the laboratory. Continuous 20 end roving pre-impregnated s glass E747, made by U.S. Polymeric Inc. and generously supplied by British Aerojet Ltd. was wound under a resin mix: Epikote 828/Epikote JPA/BDMA accelerator using a coil winder especially adapted for the purpose(59). The resulting rods were cured in a temperature-controlled oven. Rotors manufactured from the material produced from a simple hoop winding pattern of the glass fibres were unsatisfactory because the axial strength provided by the resin mix was insufficient to withstand speeds in excess of 5 kHz. To overcome this problem the coil winder was further modified to produce 30° helical windings. Although the material so produced had the required axial strength the pointed outer edges of the rotors tended to delaminate upon impact with the stator. Generally, the most reliable rotor materials were those produced by combining an initial helical winding pattern with a hoop wound outer ring. Rotors manufactured from a composite material made by hoop winding the glass fibre rovings on to a thin tube of glass cloth wrap proved equally robust.

4.4 THE FOIL BEARING ROTOR SYSTEM

4.4.1 INTRODUCTION

A foil bearing is formed between a flexible member and a rigid surface. Considering Figure 4.3 the foil is wrapped around the circular shaft and held under tension. As the shaft is rotated gas is drawn between the shaft and the foil by viscous drag. In a central region both the gap and the pressure are uniform: the

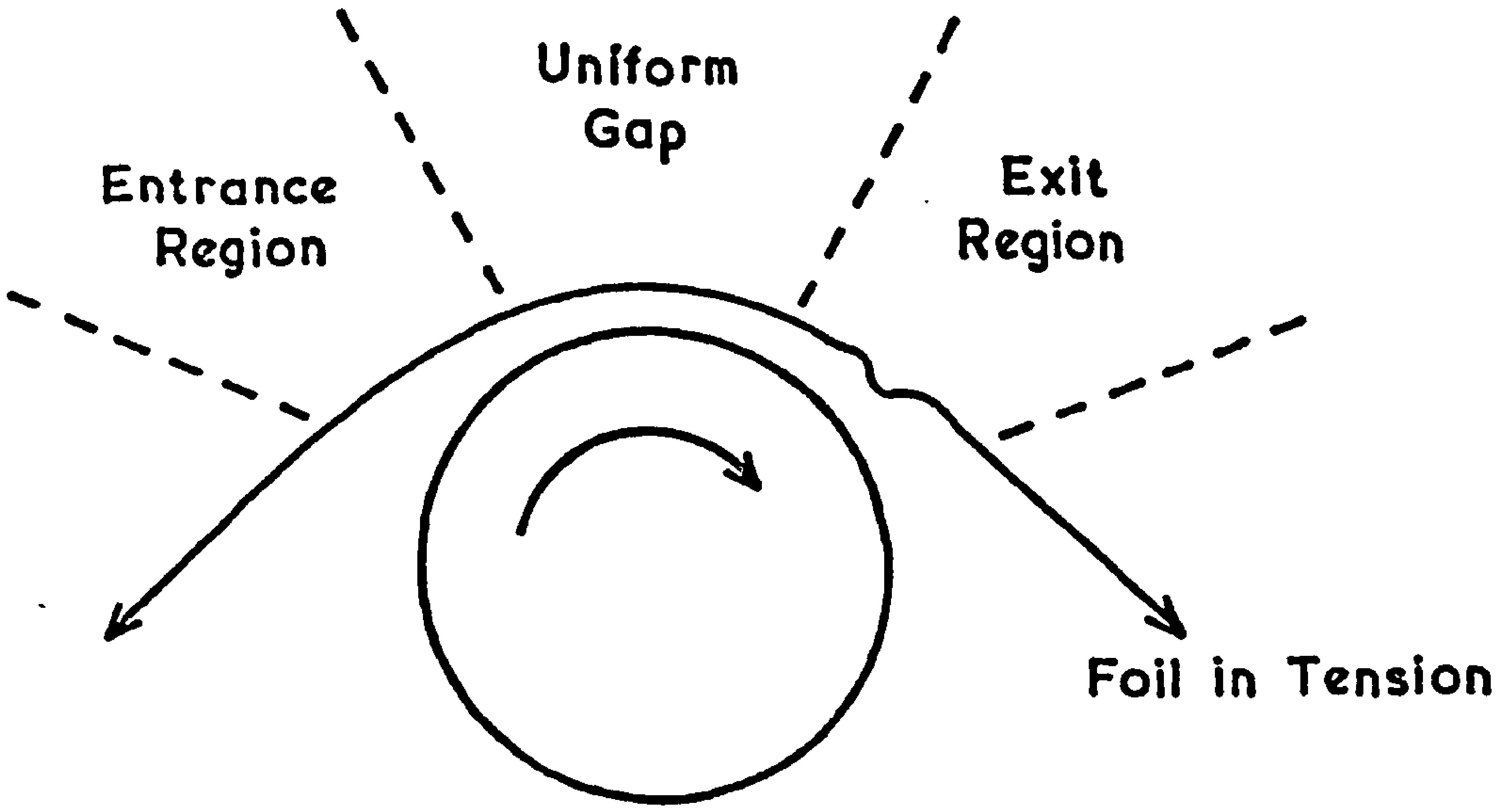

FIGURE 4.3. : The action of a self acting foil bearing

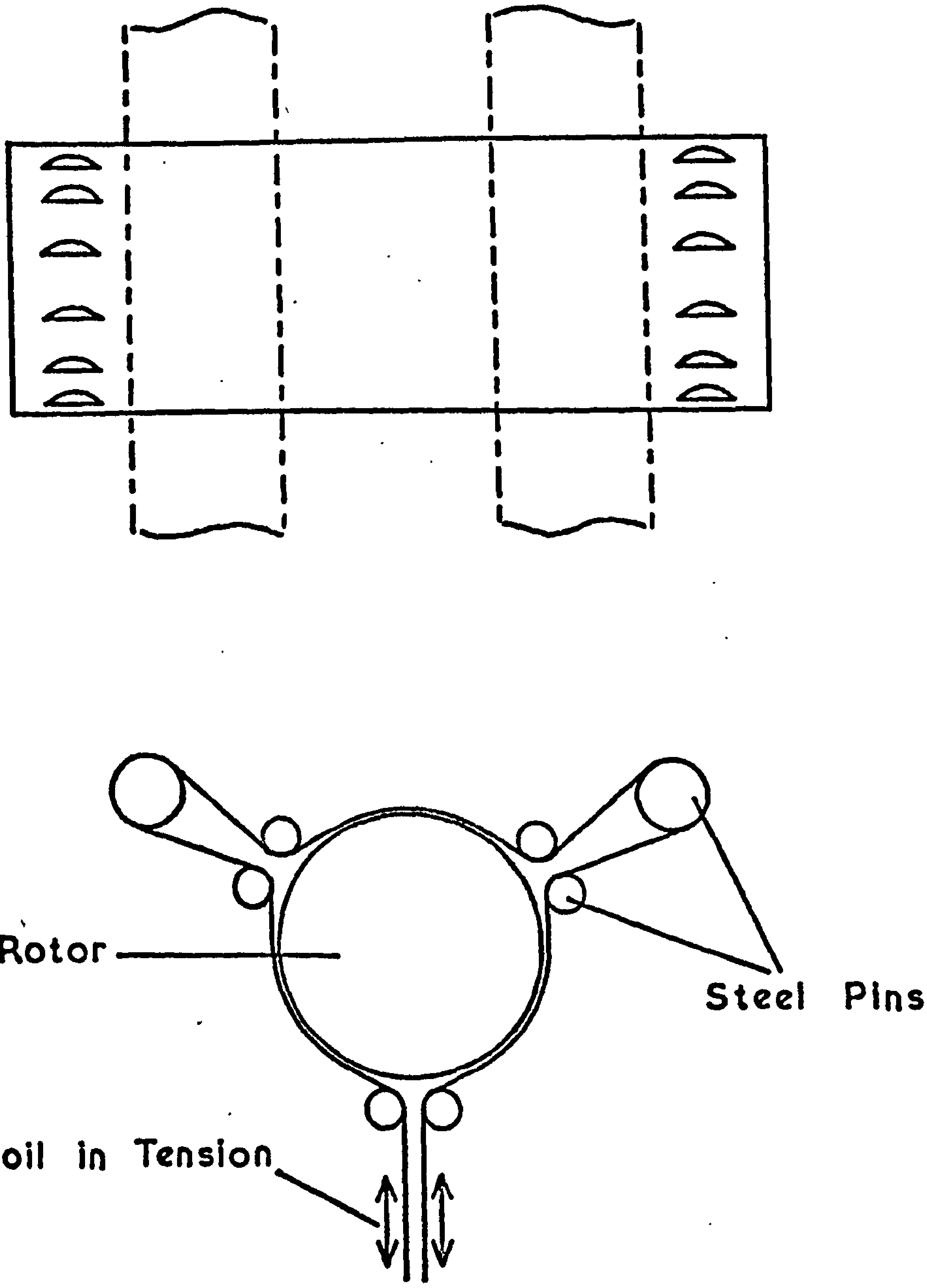

FIGURE 4.4. : The cylindrical titanium foil bearing rotor
(three times size)

gap then diverges and the pressure is reduced. The bearing formed in this way always acts perpendicularly to the surface of the rotor so the system is free from the problems of fractional speed whirl. Because the foil is flexible the bearing is unaffected by a certain degree of misalignment or imbalance in the rotor(60).

A preliminary investigation into the feasibility of attaining high rotation frequencies by using a three pad foil bearing rotor system was undertaken by the Gas Bearing Advisory Service at Southampton University(61). Considerable success was achieved with metallic rotors and a cylindrical titanium rotor (shown in Figure 4.4) reached a rotation speed of 15 kHz when propelled by helium. A second type of rotor with smaller diameter bearing axles placed at the extremities attained a speed of 11 kHz. However with non-metallic bearing surfaces the rotors failed to run reliably if at all.

4.4.2 THE ROTOR

Experience with foil bearings has shown that the use of a polished bearing surface is a most important criterion for their reliable operation. Larger diameter bearings tend to be slightly less susceptible to small surface irregularities - the mean bearing pressure is lower so there is greater clearance between the foil and the rotor. Against this the rotationally induced stresses are also greater so the rotor arbors have to be stronger mechanically.

Various non-metallic materials have been used for the rotor axles including several types of tufnol, nylon, glass, glass fibre and ceramic. Those rotors which did run either became unstable at rotation speeds around 4 kHz or suffered mechanical failure. Attempts were made to improve the efficiency of the smaller diameter bearings by both sheathing and coating the surfaces with metal. Under test such rotors ran reliably at speeds up to 10 kHz without failure. However when placed in the electromagnet, it was found that the quantity of metal needed to secure a good mechanical bond to the non-metallic arbor was sufficient to result in considerable eddy current damping. Therefore the problem has been to find a suitably strong, polished, non-metallic material from which to make the bearing axles.

The only such materials with which there has been any degree of success to-date are glass and alumina ceramic. Using two short axles glued into a glass fibre body glass disintegrated at rotation frequencies around 6 kHz. Slightly higher speeds were possible with alumina axles, but the rotors then became extremely unstable. From the successful running of rotors with solid metal and glass arbors it was obvious that the circularity of the bearing axles was not too important. However, the accurate alignment of the two axles in the rotor body was found to be critical to the attainment of higher rotation rates.

Various simple positioning jigs were tried out but the necessary degree of alignment was only realized by using a cylindrical assembly made from hardened steel as shown in Figure 4.5. Alumina rods obtained from Degussit were cut square to length and diamond ground to a tolerance of 0.0005" on the diameter, so as to be a close fit in the jig. They were glued into the rotor body with araldite epoxy and polished afterwards with Hyprex 6-w-45 diamond compound. The rotor bodies were machined from helically wound glass fibre,

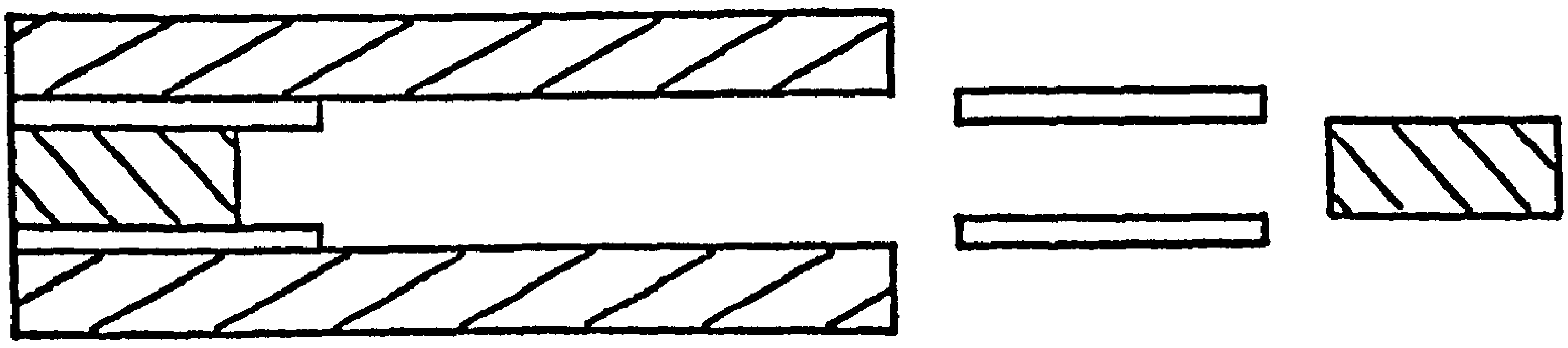

FIGURE 4.5 : The hardened steel jig used for aligning the ceramic foil bearing axles in the rotor bodies (actual size)

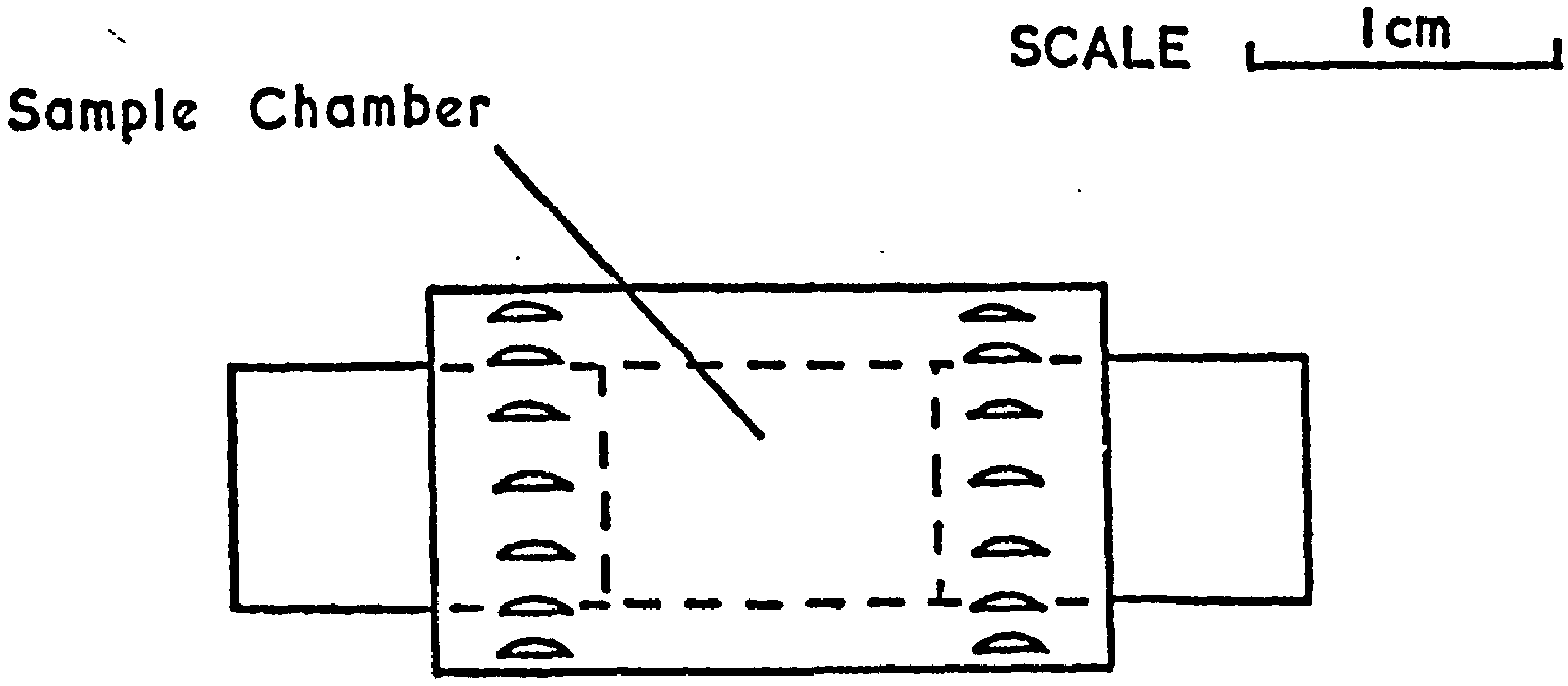

FIGURE 4.6 : The small axled foil bearing rotor

the manufacture of which was described in Section 4.3.3. Rotors constructed in this way (shown in Figure 4.6) have been run at speeds up to 9 kHz without instability. However at speeds above 7 kHz the axles are subject to mechanical failure.

The cause of these failures is not fully understood. The tensile strength of this material is approximately 2650 kg/cm^2 (62) while the radial stress predicted by equation (4.2) is 500 kg/cm^2 at 7.5 kHz. Attempts to reduce the stress concentration by rounding off the outside edges of the axles and the internal edges between the axles and body failed to improve the situation. The rotors became warm after they had been running for some time. Thermal stresses produced in the axles, as determined by simple theory(63), would appear to be an order of magnitude too small to explain failure, but experimental evidence lends weight to such an explanation. The rotors became hotter at higher rotation speeds and failure occasionally occurred even after the rotors had been spinning at a stable speed for several minutes.

4.4.3 THE SUPPORTING RIG

In the original design the bearing tapes were positioned about the rotor axle by three pairs of aluminium pins and tensioned by weights. Other methods of tensioning such as clamping the tapes around rubber bushes and the use of simple springs generally proved inferior especially at higher rotation speeds. Once the bearing tapes had 'bedded in' the degree of tensioning failed to affect the performance of the rotors to any great extent. Normally the rotors started more easily and ran slightly faster with a minimum of tension but at higher rotation rates they were most stable when the tension was increased to about 40 gm. The tape used was 0.005" thick glass reinforced PTFE obtained from Tygadure Ltd. Thinner tape was less able to withstand the rigors of the rotors starting and stopping and thicker tape tended to be too stiff. Metal tapes have proved more successful for rotors with larger diameter axles.

The driving jets were constructed from brass or aluminium with two or three equally spaced about each set of rotor flutes. For starting a simple on/off switch was used with an air pressure of around 100 psi. The rotors then quickly accelerated to a stable spinning speed. The most efficient drive was achieved using a nozzle diameter of 0.025". The rotor flutes were cut to a depth of 0.025" with 24 in each set. By placing the rotor so that the propelling gas impinged against the curved face of the flutes it was found that the rotors were sufficiently constrained axially to make superfluous the use of any separate positioning jets.

In theory the three-pad foil bearing is ideal for its purpose because it supports the rotor equally in all directions about the axis of rotation. However a two-pad system was found to be equally efficient. This considerably facilitated the construction of a rig capable of supporting the rotors within the magnet gap. Because the tapes had to be free to move, the foil guides were rounded with a polished surface. They were glued separately on to the two halves of the rig after machining. The full experimental rig is shown in Figure 4.7, and Figure 4.8 shows the rotation rates achieved in it by a solid aluminium rotor.

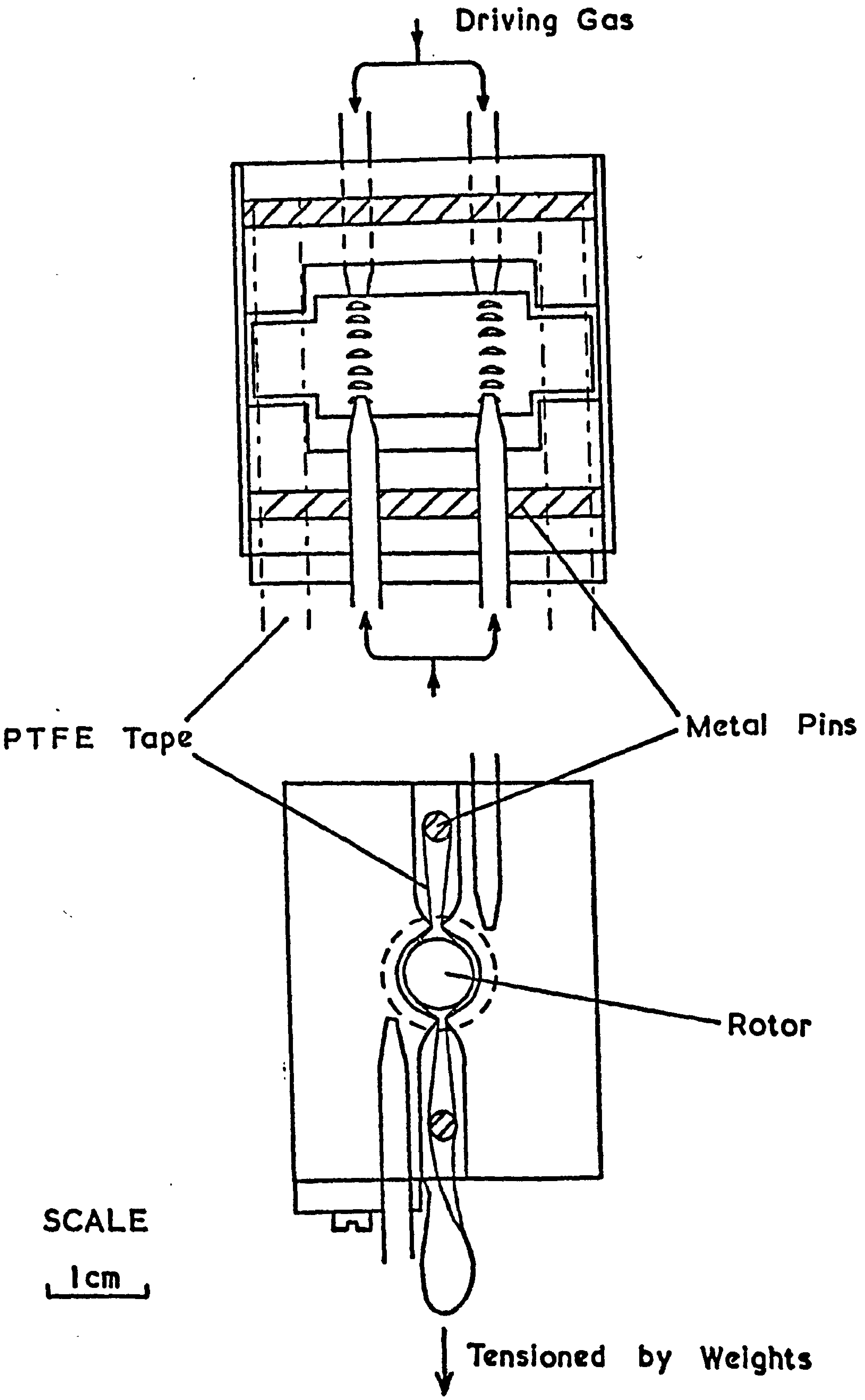

FIGURE 4.7 : The experimental rig for supporting the foil bearing rotors

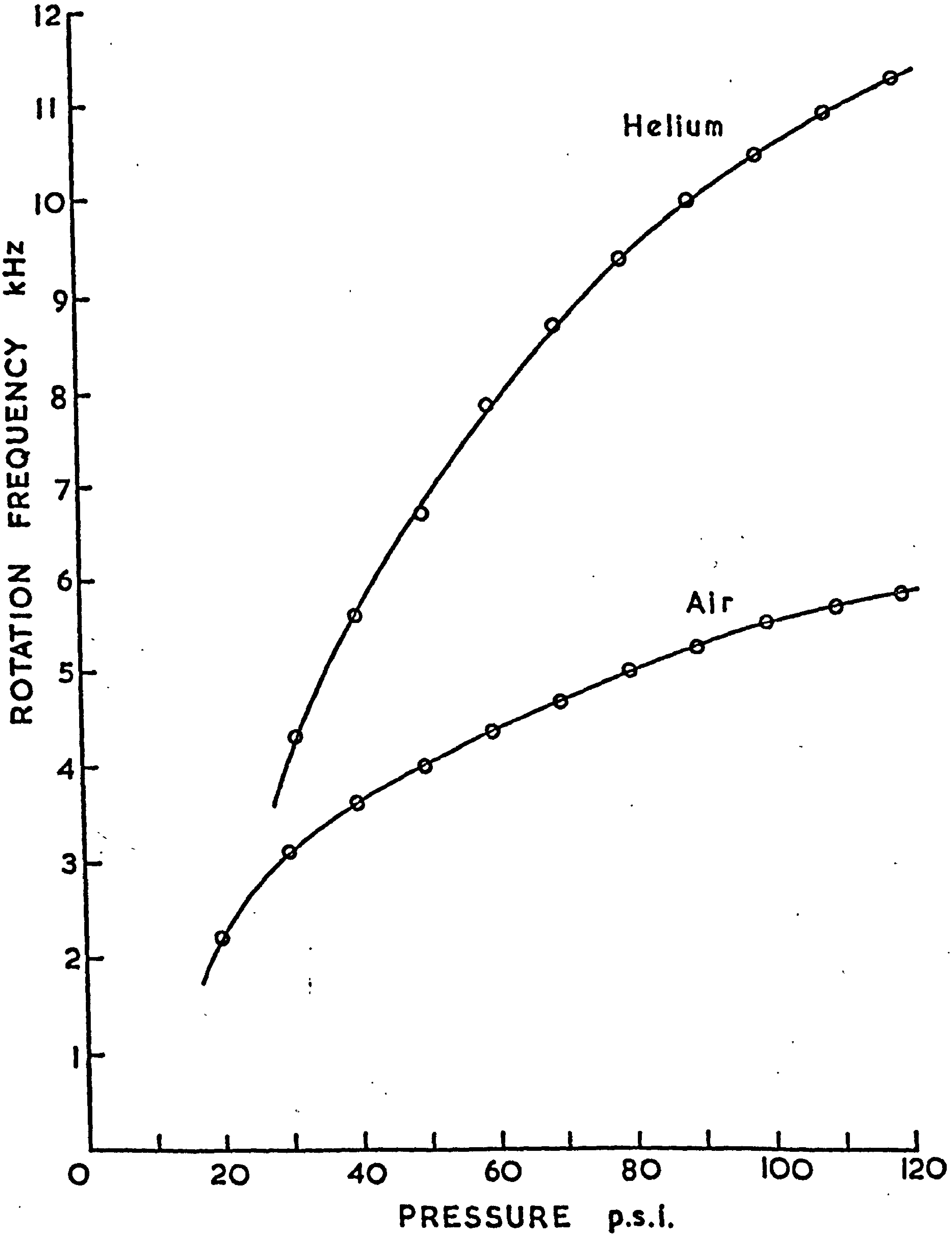

FIGURE 4.8 : Rotation rates attained by a metal foil bearing rotor for air and helium driving gas

4.4.4 COMMENTS

For completeness we include at this point a few general comments about the foil bearing rotor system.

It was found that at speeds up to 7 kHz the foil bearing rotors were extremely reliable. Every rotor constructed as described in Section 4.4.2 rotated stably even with full-sized liquid samples. Not all the conical rotors would rotate, even on air. Although it is not a normal requirement of any NMR rotation system, it is worth noting that the Bernoulli rotors would not spin with liquid samples of any reasonable volume.

Because of the heating effect upon rotation, use of the foil bearing system appears to be limited to those cases where the temperature of the sample is relatively unimportant. As the attainment of rotation rates above 7 kHz was limited only by the failure of the alumina axles, silicon nitride might well prove a more suitable axle material. Its tensile strength is typically the same as alumina, but its density is only about 2.6 gm/cm^3 compared to 3.8 gm/cm^3. The coefficient of thermal expansion in silicon nitride is half that of alumina(64) so upon rotation both the induced thermal and mechanical stresses should be less. If the use of this or any other material does result in a considerable improvement in performance it might prove possible to use a much simpler rotor design in a foil bearing, such as a single hollow tube.

4.5 OTHER TURBINE SYSTEMS

4.5.1 THE AXLE SUPPORTED ROTOR

This rotor system has been used by a number of workers(34,39,44). The hollow cylindrical rotor with a snap-on lid is supported about its axis by a fine phosphor-bronze wire and propelled by a single gas jet impinging against a ring of flutes about the rotor circumference. Using compressed helium rotation rates of 8 kHz have been reached. However these rotors are apparently only capable of stable operation when the diameter/length ratio is greater than one, which limits the volume of the sample chamber. Unfortunately the filling factor of the rf coil is relatively poor in this system.

4.5.2 THE PRAGUE ROTOR SYSTEM

A rotor of a more conventional design has been used for the measurement of proton magnetic resonance(50,65). The rotor is suspended in two externally pressurized conical gas bearings and driven by two pairs of jets placed against flutes on the main body, as shown in Figure 4.9. Using rotors machined from polymers rotation speeds of 10 kHz have been achieved but, for samples placed in hollow glass or sapphire rotors of internal diameter 3.5 mm the speeds were limited to 5 kHz. These spinning frequencies were reportedly dependent on machining tolerances of less than 0.003 mm.

An investigation has been carried out on a similar system directly copied from this design. When propelled by compressed air at a pressure of 100 psi a solid nylon rotor reached a spinning

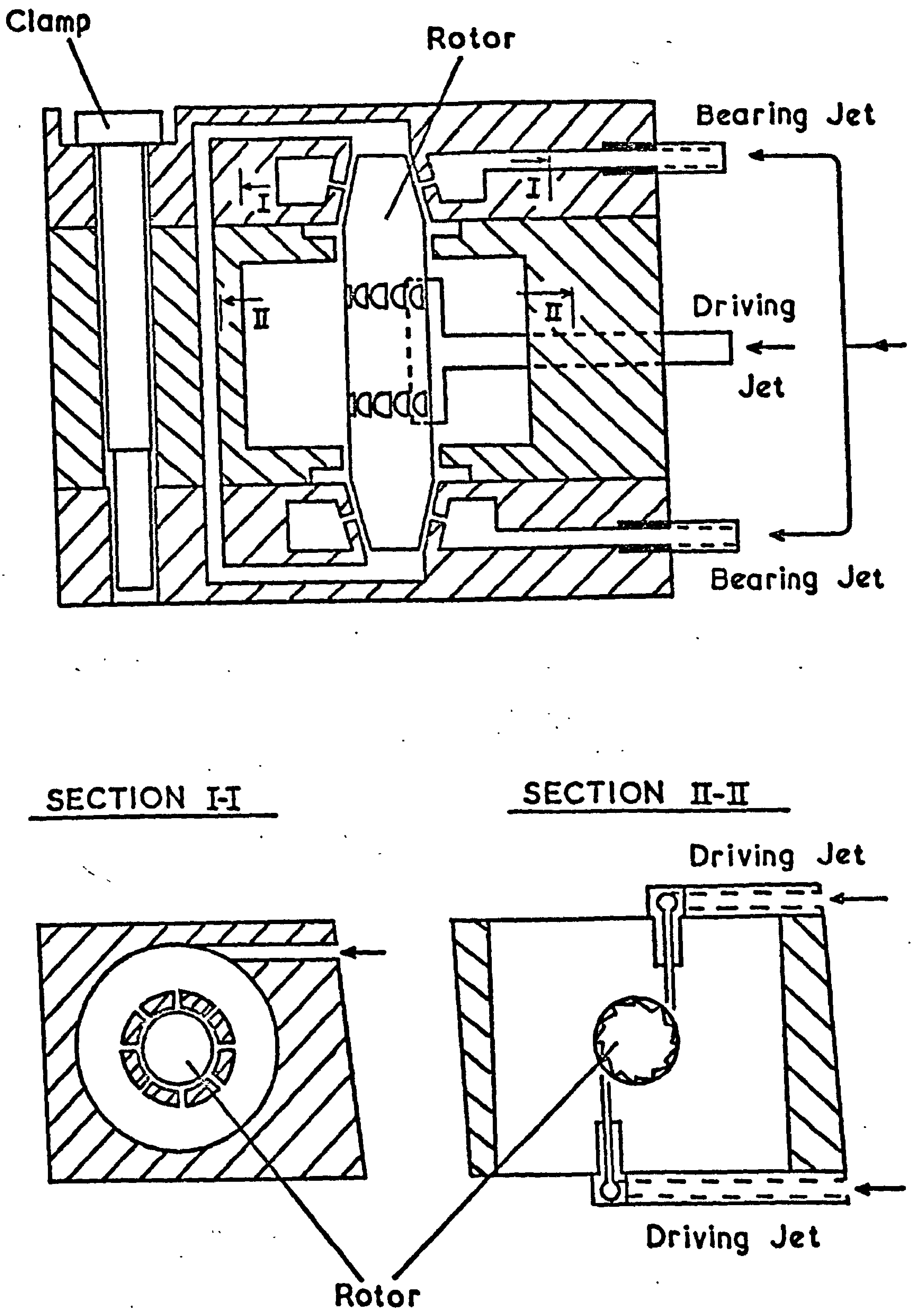

FIGURE 4.9 : The 'Prague' rotor system (twice size)

rate of 6 kHz. Higher speeds were achieved by using helium. The rotors would spin at all frequencies down to 20 Hz and were largely unaffected by altering the clearance between the rotor and the bearing: characteristics which were remarkably different from the original system.

The sample-carrying capacity of the Prague rotor system is inferior to the conical and foil bearing rotors. The only obvious advantage of the rotors produced in the laboratory was their stable operation at very low frequencies. As this is not a normal requirement of an NMR system, work was discontinued on this type of rotor in favour of the foil-bearing design.

CHAPTER 5

EXPERIMENTAL PROCEDURE

5.1 EQUIPMENT

The variable frequency pulse spectrometer used in this work was a Bruker B-KR 322s, a schematic diagram of which is shown in Figure 5.1. The rf is generated to an accuracy of 1 part in 10^8 by the Schmondal frequency synthesiser and split into two main channels. DC gating pulses are supplied by four separate pulse units feeding in pairs to each channel. The resulting rf pulses are amplified to a peak power of 500 W and output to the transmitter coil is the probe head. Induced transients in the receiver coil are passed via a tuned preamplifier and a variable attenuator to a wide band main amplifier before diode or phase sensitive detection. The resulting signal is amplified in a final stage postamplifier.

The spectrometer was augmented by a Bruker B-KR 300z 15 pulse gated integrator (PGI). This was used to measure signal amplitudes at fixed points on the detected transient decay curves. Gate sampling times between 0.5 μs and 10 ms could be used and the integrator time constant was adjustable between 10 μs and 100 s. The output voltage level was displayed on a Solatron LM 1420.2 digital voltmeter (DVM).

Signal averaging was undertaken by a Data Laboratories DL 102 200 point signal averager. In this instrument input voltages within

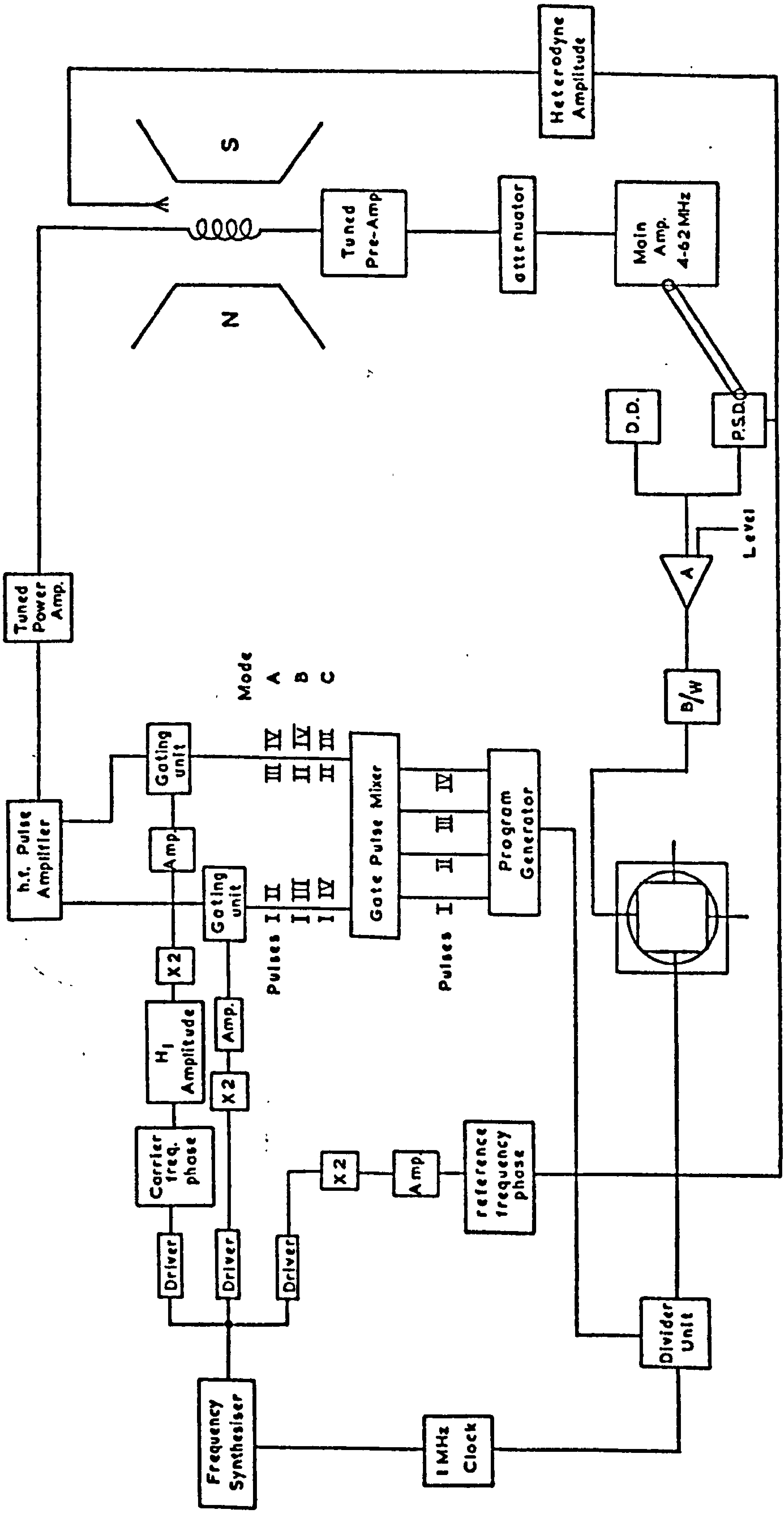

FIGURE 5.1 : Block diagram of the Bruker B-KR 322 s pulse spectrometer (59)

the range ±1 V are digitised to a 7 bit resolution and summed in a 16 bit register. The time interval per point is variable between 2 μs and 50 ms and the averaged signal may be displayed on an oscilloscope to 7 bit accuracy. In the particular experimental set-up used the full 16 bit output of each register was read out through a Data Laboratories 1002/100c interface coupled to a Data Dynamics teletype.

The M12 electromagnet used in this work had originally been part of an RS 2 high resolution CWNMR spectrometer manufactured by AEI. The maximum period of time over which the signal could be accumulated in the signal averager was in some cases limited by the slight drift in the magnetic field.

5.2 MODIFICATION OF THE SPECTROMETER PULSE PROGRAMMER

The four pulse units of the spectrometer are located in interchangeable plug-in units. Each unit consists of two monostable flip-flops; one for determining the pulse length and one for determining the delay time with respect to the previous pulse. However, because the delay times are set via decade counters, they are correct only when the pulse delay time is less or equal to that of the preceeding pulse. Such a condition means that some simple pulse sequences cannot be performed using the standard spectrometer.

To overcome this problem a Mullard FJK 101 integrated monostable circuit was set-up to provide a positive DC pulse of continuously variable duration between 0.5 μs and 120 ms compatible with the internal logic of the spectrometer. The complete circuit was mounted in an aluminium box with a plug connector so as to be interchangeable with any of the plug-in pulse units. The monostable circuit was triggered by the leading edge of the preceding pulse. The trailing edge of the resulting pulse then triggered the delay on the next pulse unit, so the total delay time was the sum of the two settings. In this way pulse sequences requiring three pulses could be performed even when the delay time between the first and second pulses was shorter than that between the second and third. Such is the case for the Jeener and Brockaert pulse sequences as described in Sections 5.7 and 5.8.

5.3 VARIABLE TEMPERATURE MEASUREMENTS

For measurements other than at room temperature the temperature of the sample could be controlled using a Bruker B-ST 100/700 temperature control system. In this system nitrogen gas is passed through a heat exchanger immersed in liquid nitrogen and then to a glass dewar probe insert via a heater. The temperature of the gas immediately underneath the sample tube in the insert is monitored by a copper-constantan junction connected to the control unit. This automatically adjusts the current to the heating coil so that the temperature of the junction corresponds with that selected.

The low temperature measurements on the cuprous halides were performed using a small gas flow cryostat. The assembly shown in Figure 5.2 was supported in a glass dewar in the magnet gap. Although the Bruker control unit was used to adjust the flow of cooling gas the temperature immediately above and below the sample was measured independently via two calibrated copper-constantan thermocouples and a DVM. The lowest temperature was attained by

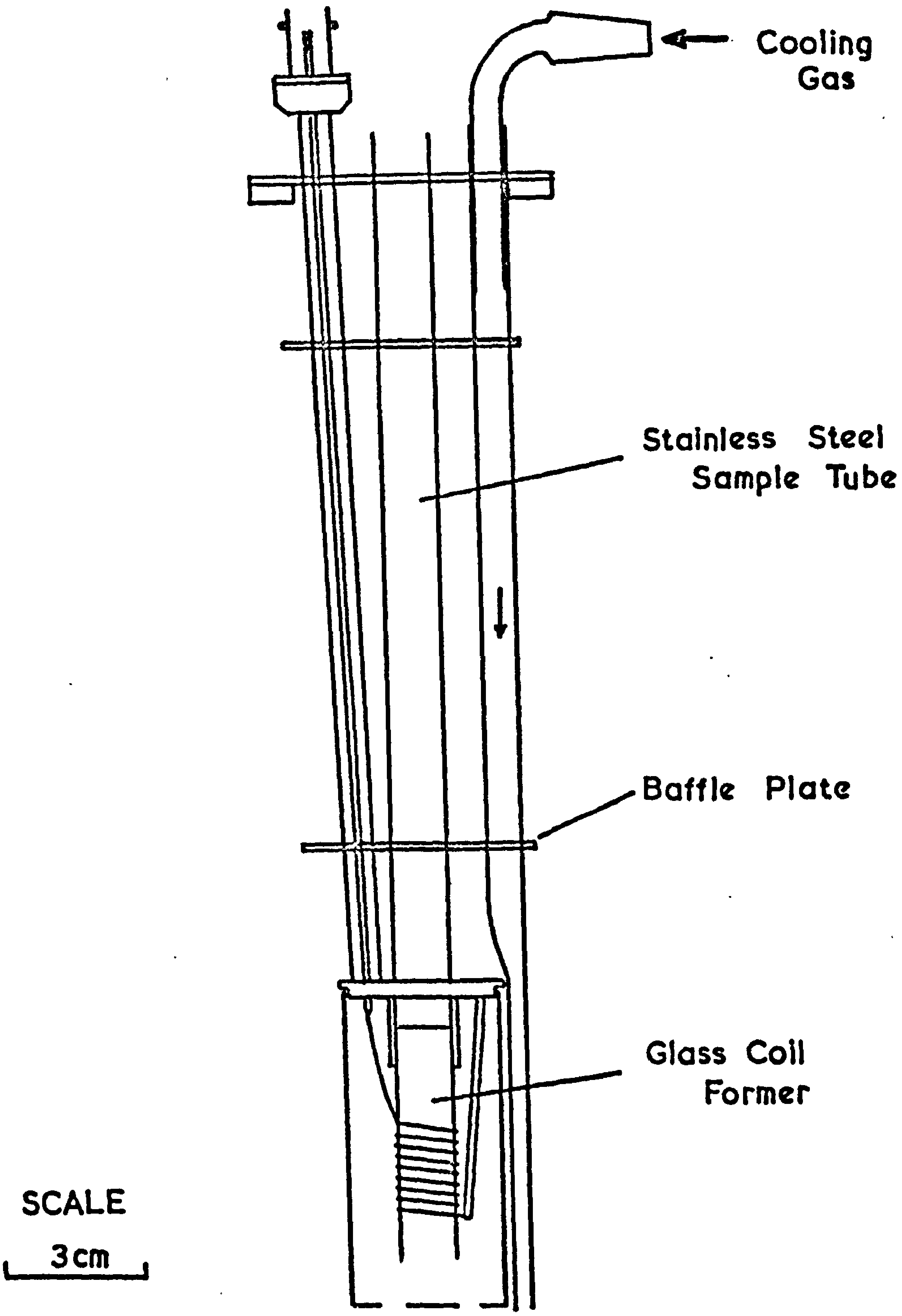

FIGURE 5.2 : The gas flow cryostat used for cuprous halide measurements

sealing the aluminium can surrounding the coil and submerging it directly into liquid nitrogen.

5.4 THE PROBE HEADS

5.4.1 THE DESIGN OF THE TUNED CIRCUITS

A tuned PNMR transmitter circuit is required to produce a high power H_1 field in the sample from an rf pulse. The Fourier transform of a rectangular rf pulse forms a distribution of frequencies about the driving frequency the width of which is of the order of the inverse of the pulse width. By making H_1 large it follows from equation (1.9) that the pulse length is short. All nuclei will then be excited equally, even in solids having broad spectral distribution functions.

After the exciting rf pulse the tuned receiver tank circuit has to recover quickly to enable the small nuclear transient signal to be amplified and detected. The importance of having only a short 'dead time' during which the receiver is blocked arises because that part of the signal near zero time makes a large contribution to the wings of the transformed lineshapes. If the signal induced in the receiver coil of a series resonant circuit is $V \sin \omega t$, then the voltage appearing at the receiver input is $QV \sin \omega_o t$ where Q, the quality factor, is given by $\omega_o L/R$. The ringing in this circuit decays exponentially with a time constant $2Q/\omega_o$(66). It follows that the two conditions of maximum signal and minimum dead time are incompatible and a compromise has to be adopted.

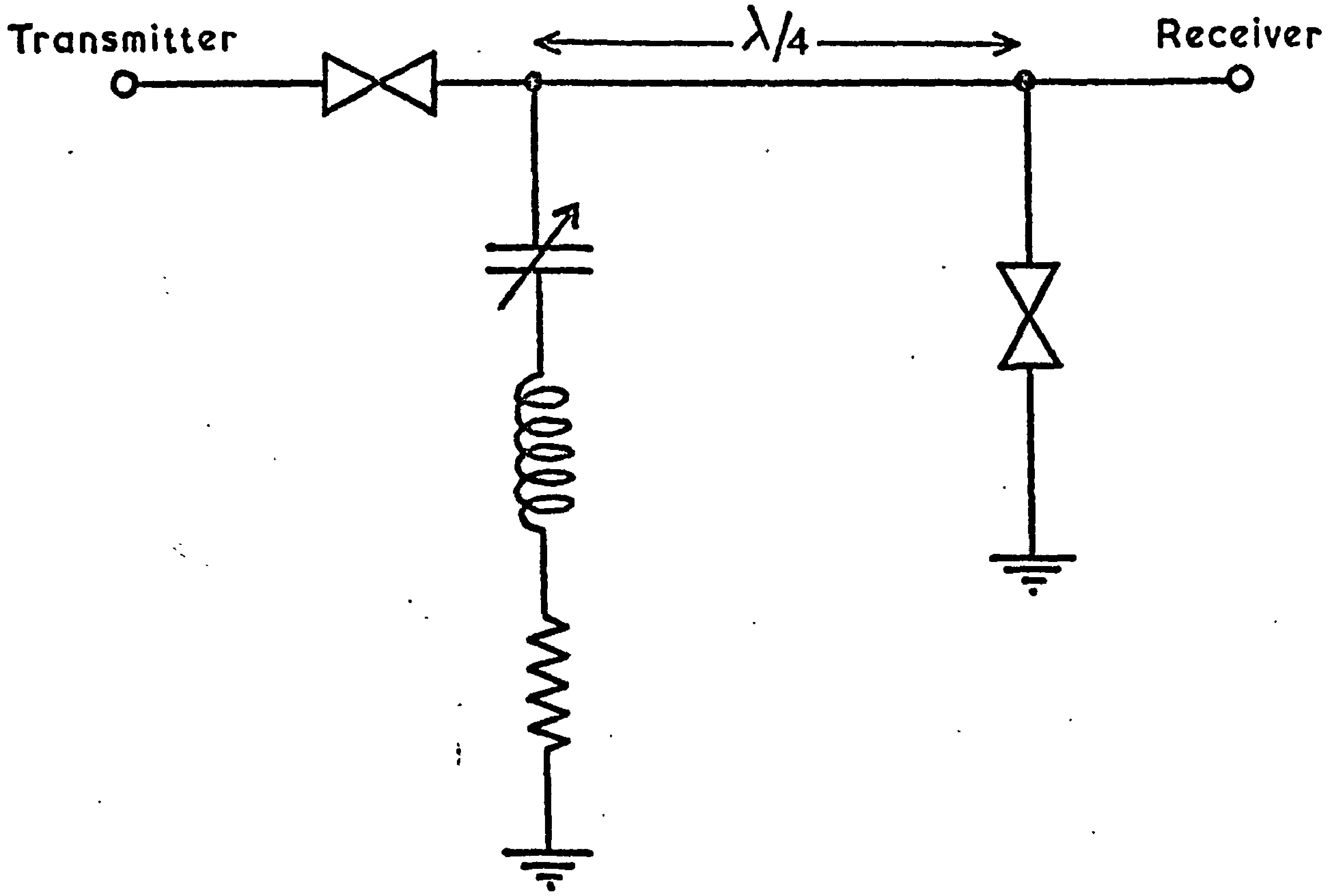

FIGURE 5.3 : The single coil probe head circuit

The Bruker probe system employs separate transmitter and receiver coils wound orthogonally. However for the rotor probe heads and the gas flow cryostat it was found more convenient to use a single coil system as shown in Figure 5.3. In the arrangement used the sample coil was part of a series tuned resonant circuit. When the pulse is applied both pairs of crossed diodes conduct but, because the short circuited quarter wavelength cable acts as an infinite impedance, the receiver is isolated from the tuned circuit. When the pulse is switched off the crossed diodes become non-conducting. The quarter wavelength cable then effectively short circuits the receiver across the tuned circuit.

In each case the number of turns in the coil was set so that at the frequency required the tuned circuit had an impedance of approximately 60 ohm, the output impedance of the power amplifier. This operation was facilitated by the use of a Hewlett Packard 4815 A rf vector impedance meter. Although the coils possessed an intrinsic resistance a small value resistor was sometimes added to the series circuit. This had the effect of shortening the receiver dead time by reducing the Q factor. The amplitude of the nuclear transient signal at the receiver input was also reduced, but this was not usually too important because of the use of signal averaging techniques.

5.4.2 MECHANICAL CONSTRUCTION

For the gas flow cryostat the electromagnet was opened out to its full 3" pole gap. Copper wire was found to interfere with the copper resonances so the coil was wound from 36 SWG silver

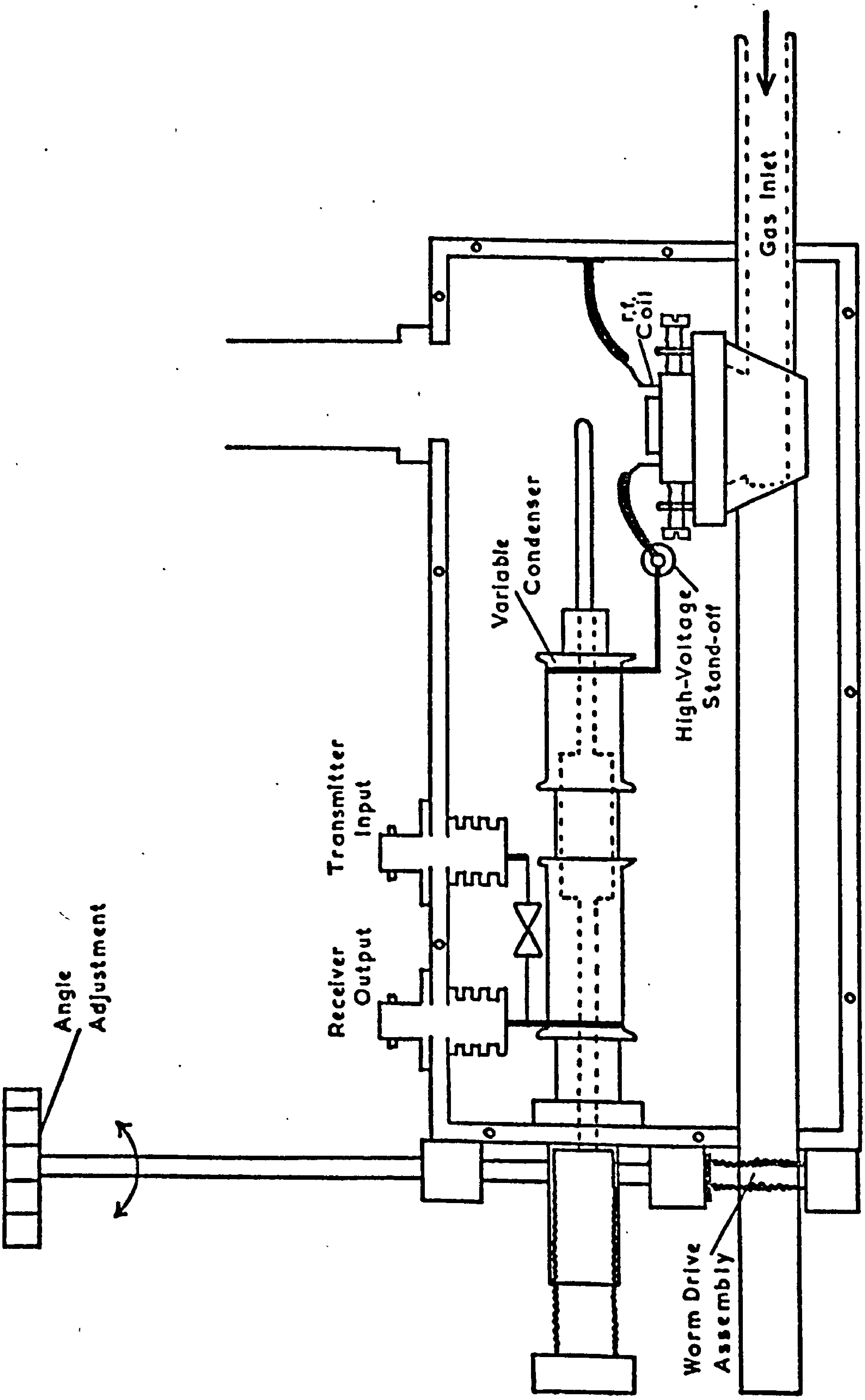

FIGURE 5.4 : The spectrometer probe head for the conical rotors

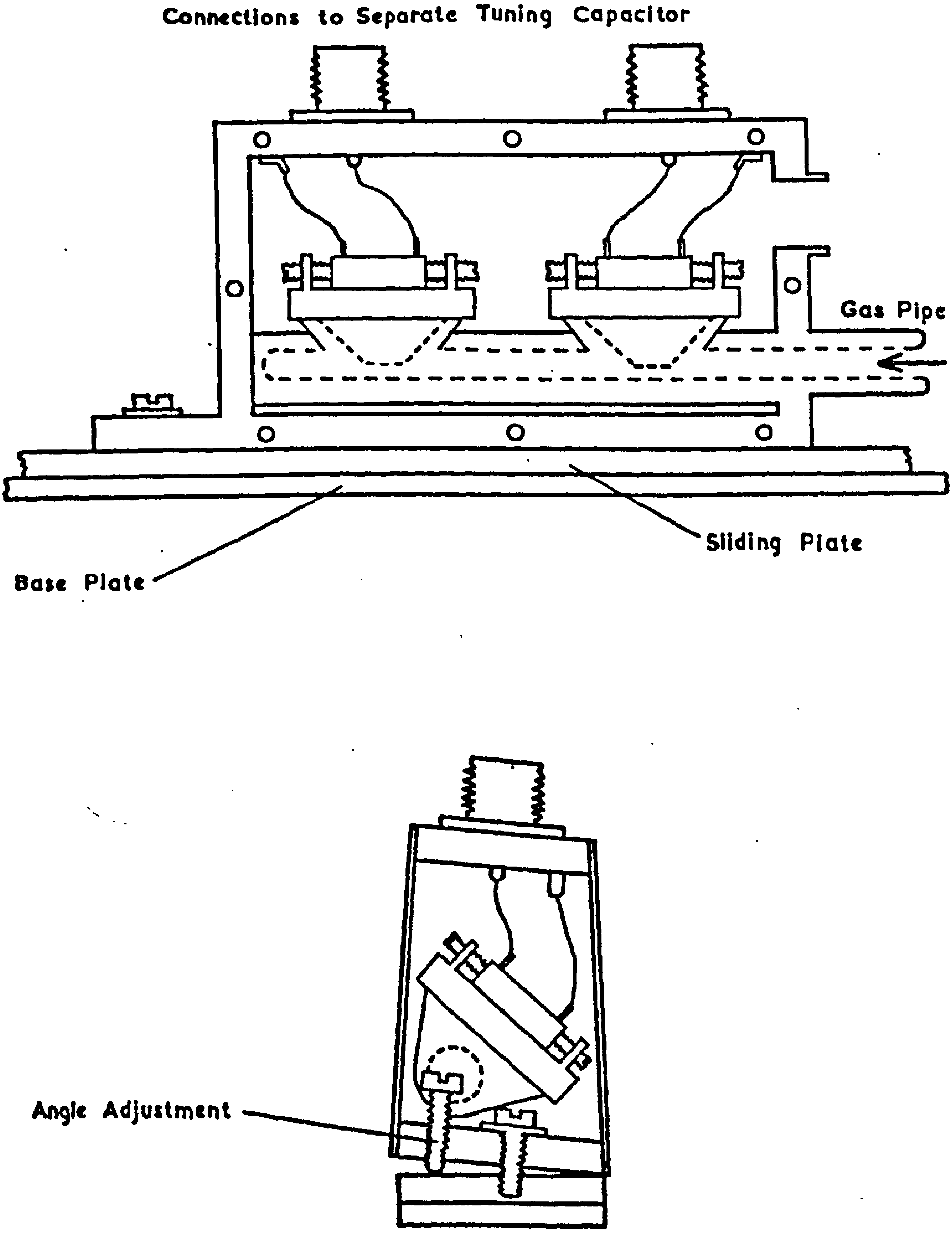

FIGURE 5.5 : The double rotor spectrometer probe head

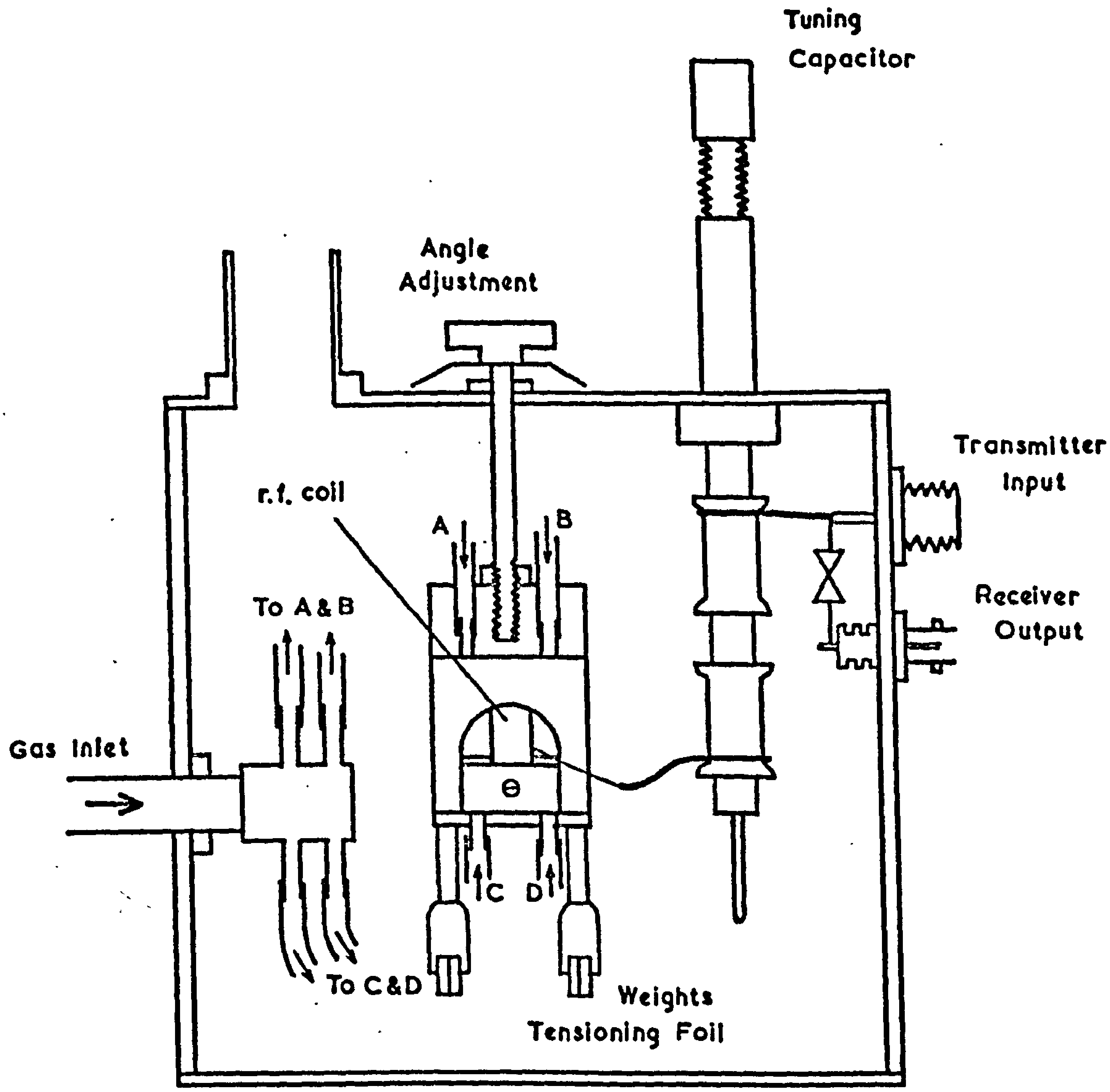

FIGURE 5.6 : The spectrometer probe head for the foil bearing rotors

wire. The tuning capacitor, identical to those used in the rotor bosses had a tuning range of 6-30 pF. It was placed in an aluminium box and connected to the coil by a short co-axial cable and a shielded small diameter stainless steel tube. Because of the stray capacitance introduced into the tuned circuit the inductance of the coil was fairly critical. For the measurements of the spin-lattice relaxation times in the cuprous halides which were performed at 12.5 MHz it was optimized to a value of 3.25 μH.

The rotor probe heads were designed for a 2" magnet gap. They were constructed mainly from dural and those parts of the body near the rf coil were coated with varnish to eliminate mechanical vibrations set up by the rf pulse. The three types of probe head used are shown in Figures 5.4, 5.5 and 5.6. Adjustment of the magic angle was achieved in a different manner in each case. For the conical rotor system the rotors were canted at an angle in the box. Fine adjustment was performed by a worm drive onto the stator mounting in the single box and a simple screw system in the double box. In the foil bearing system the rig was adjusted in the horizontal plane by rotation of the supporting rod.

5.5 KNIGHT SHIFT MEASUREMENTS

Accurate determinations of resonance frequencies were made by employing the Bruker phase sensitive detector. Assuming that the nuclear lineshape is symmetric about the Larmor frequency ν_o, then from consideration of the rotating frame it can be seen that the frequency of the reference signal may be adjusted so that the temporal behaviour of the magnetization is observed directly. The phase can then be set so that the transverse magnetization is completely nulled out. If, however, the reference frequency is different from ν_o the FID is modulated by beats at the frequency difference and the null condition cannot be achieved. For asymmetric spectra the spins fan out unevenly about any axis in the rotating frame. As a result it is impossible to measure the centre frequency by direct observation of the transient signals.

Experimentally the most homogeneous position in the magnet gap was first found by using a suitable liquid specimen. A direct comparison between the resonance frequencies of liquid samples could be made by fine adjustment of the frequency synthesiser. For weaker signals this operation was facilitated by a reduction of the receiver bandwidth and the use of the DL 102 signal averager.

The precise Knight shift measurements undertaken depended upon the narrowing of the resonance spectrum by rapid sample rotation at the magic angle. Experimental Knight shifts are often determined against liquid reference samples, but the conical rotors used for this particular work would not rotate with liquid samples of any reasonable volume. Therefore it was not possible to place the metal and the reference specimen together in the same rotor as has been done previously(67). Instead a different procedure was adopted using the double rotor box shown in Figure 5.5. The accuracy achieved was a significant improvement over previous Knight shift estimates on the same metals. A short account of the procedure adopted is included below.

A rotor was placed in one stator and the liquid reference sample was put in an equivalent position in the second 'dummy' stator. The assembly could be slid through the magnet pole gap on top of a rigidly mounted base plate and locked into position. Hence, without moving the main support or stopping the rotors spinning, the two samples could be placed in exactly the same position in the external field and their resonant frequencies determined. Two identical sample coils were used which were connected alternately to the external tuning capacitor. Any difference in the magnetic field at the two stator positions was measured by replacing the rotor with a second identical reference sample. Normally the stator and clamping ring were made from dural, but for the Knight shift measurements on aluminium the stators were made from copper and the clamping rings from nylon.

5.6 FOURIER TRANSFORM PROCEDURES

As stated in Section 1.3 the absorption spectrum may be obtained by Fourier transformation of the measured FID. This requires that the detected signal is directly proportional to the transverse magnetization in the rotating frame, i.e. that the receiver system is linear. A simple check of the gain linearity was carried out using different sample volumes and keeping the receiver attenuation constant. There was no measurable variation in the shape of the recorded FID, or the transformed lineshapes. The gain constancy with frequency was checked by keeping the spectrometer controls unchanged and comparing the resonance spectra obtained at different values of the applied magnetic field. Over quite a wide range of resonant frequencies (>> linewidth) there was again no change in the recorded lineshapes.

The transient nuclear signals were recorded by using the DL 102 signal averager. In the experimental arrangement used each scan through the 200 memory channels was triggered off the leading edge of the gating pulse to the transmitter and the detected FID following the rf pulse was DC coupled into the averager. No on-line Fourier transform capability was available, so the contents of the averager's memory were output to the teletype and recorded onto paper tape. Fourier transformation of the recorded data was undertaken with the University's ICL 1906A computer. The program used for this purpose basically operated from the numerical summation

$$f(w) = \frac{1}{\pi} \sum G(t) \cos \omega t \ \delta t \quad .$$

Second moment values were determined from the transformed spectra by a simple summation procedure written into the computer program.

Asymmetric nuclear lineshapes such as those arising from anisotropic Knight shift interactions were obtained by setting the reference frequency to the phase sensitive detector well outside the resonance spectrum. The transient response to the rf pulse was then recorded along a single detection axis in the rotating reference frame. After a correction for the reference phase the decay signals were transformed using the same summation procedure as above. This results in a symmetric frequency distribution with the asymmetric absorption lineshape mirrored about ν_{ref}.

The time origin of the recorded decay shapes was taken as the centre of the rf pulse for all measurements. This position has been determined theoretically(68) and was confirmed for the rotating samples by direct observation of the spinning beats on the FID.

5.7 FITTING THE DEAD-TIME POINTS

Before computation it was necessary to define that portion of the transient nuclear signal that was lost during the intrumental dead time. The dead time after the rf pulse was typically 10 μs for the Bruker probe system, but slightly longer for the single coil circuits. The characteristic FIDs from the spinning samples were long, so of the full decay shapes recorded in the store of the signal averager only the first one or two data points were lost. These could be estimated fairly accurately from the subsequent behaviour of the FID. The dead time points of the signals recorded off resonance were estimated by extrapolating the beats of the detected decay shapes back to the centre of the rf pulse. The phase of the first data point of the correct full decay signal was then set empirically so as to give a flat baseline on the transformed lineshape.

The attainment of reliable second moment values for the aluminium samples depended upon the accurate prediction of the form of the FID near the time origin. To assist in this task the behaviour of the transverse magnetization near zero time was investigated using the solid echo pulse sequence and a three pulse sequence proposed by Jeener and Brockaert(69). The procedure adopted consisted of plotting out the first few detected points of the FIDs: those points lost were then computed so that the initial part of the decay curve mirrored the decay envelopes obtained from the two pulse sequences as described below.

5.7.1 THE SOLID ECHO PULSE SEQUENCE

For a dipolar coupled spin system it may be shown(70,71) that at resonance the transient response following a $90\text{-}\tau\text{-}90_{90}$ pulse sequence is given by the power series

$$M_y^*(t' - \tau) = 1 - M_2 \frac{(t' - \tau)^2}{2!} + M_4 \frac{(t' - \tau)^4}{4!} + M_{4\varepsilon} \frac{6t'^2\tau^2}{4!} + \ldots$$

t' is the time measured from the second pulse, τ is the time between the two pulses and $M_{4\varepsilon}$ is an error term defined by Mansfield(71). It follows from equation (2.20) that when the product $t'\tau$ is small the response following the second pulse closely resembles the FID.

In practice the pulse lengths and the detection axis of the PSD were adjusted for maximum signal. The phase of the second pulse was set so that the response from a single such pulse was zero, and τ was fixed so that the echo maximum occurred immediately after the dead time of the second pulse. The echo shape was then recorded with the signal averager.

5.7.2 JEENER AND BROCKAERT 'ZERO TIME' SEQUENCE

The results obtained from the aluminium samples with the solid echo sequence were confirmed in part by using a $90_{90}\text{-}t\text{-}90_{-90}\text{-}\tau\text{-}90_{90}$ pulse sequence. In this sequence the magnetization in the rotating frame $M_y^*(t)$ is transferred back to the z direction by the application of the second pulse 180° out of phase with the first. After a time $\tau > T_2$ the transverse magnetization has disappeared so that, providing $\tau \ll T_1$, the amplitude of any point on the FID following a third 'read' pulse is then directly proportional to $M_y^*(t)$.

The delay τ was set using the delay unit described previously and the signal intensity after the third pulse was monitored with the PGI. The form of the FID was found by stepping out the time t between the first and second pulses. However, the effectiveness of this pulse sequence was limited to times (t) greater than the width of the 90° pulses.

5.8 MEASUREMENT OF RELAXATION TIMES

5.8.1 SPIN-LATTICE RELAXATION TIME (T_1)

Both 180-τ-90 and 90-τ-90 pulse sequences were used to measure spin-lattice relaxation times. In these sequences the first pulse removes the magnetization from the z direction and the amplitude of the FID following the second pulse determines that fraction that has returned after a time τ. Assuming a single relaxation time the exponential recovery envelope plotted out in this way is of the form

$$\frac{V[0] - V[\tau]}{K} = \exp(-\tau/T_1) \tag{5.1}$$

where $V[0]$ is the signal magnitude following a single 90° pulse; K takes the values $V[0]$ and $2V[0]$ for the 90-τ-90 sequence and 180-τ-90 sequence respectively. T_1 may then be found from the linear graphical plot: $\ln[V[0] - V[\tau]]$ versus $-\tau/T_1$.

From equation (5.1) it follows that after a time $\simeq 5T_1$, the magnetization has returned to equilibrium along the z axis and the sequence may be repeated. In practice the PGI was used to measure the signal amplitude at a fixed time after the second pulse. Once a constant value was recorded the pulse separation τ was changed and the procedure repeated.

5.8.2 DIPOLAR RELAXATION TIME (T_{1D})

Measurements of T_{1D} (or more accurately T_{1S}) were undertaken using the $90-\tau-45_{90}-t'-45_{90}$ pulse sequence of Jeener and Brockaert(69). In this sequence two rf pulses 90° out of phase are used to transfer Zeeman order into observable amounts of dipolar order. We include below a simple explanation as to the effect of this pulse sequence on the nuclear spin system.

The first 90° pulse aligns the spins along the y* axis in the rotating frame. After a time $t \sim T_2$ the spins have dephased so that the fast spins point along the +x* axis direction and the slow spins along the -x* direction. The second pulse along y* turns the fast spins along the -z direction and the slow spins along the +z direction. Once the remaining transverse magnetization has decayed to zero this corresponds to a state of dipolar order, i.e. an absorption spectrum which is absorptive above ν_o and emissive below. Although this explanation is based on two 90° pulses the transfer of order is most efficient when the second pulse length is reduced to 45°. A third pulse, again 45°, is used to detect the amount of dipolar order after a time t'.

Experimentally the sequence was set up in the same manner as described by Tunstall and Brown(72) and will not be reiterated here. The delay unit described in Section 5.2 was used to step out the time t' between the second and third pulses and the amplitude of the resulting echo was monitored with the PGI. The value of T_{1D} was obtained by plotting ln V(t') versus $-t'/T_{1D}$.

5.9 SAMPLE PREPARATION

5.9.1 CUPROUS HALIDES

Three cuprous halides exist in the solid state, CuCl, CuBr and CuI (CuF is unstable at ordinary temperatures$^{(73)}$). Reagent grade specimens of each of these compounds were used together with pure specimens of CuBr and CuI obtained from Alfa Inorganic. In each case about 1 cm^3 of polycrystalline material was sealed into glass phials under vacuum. At low temperatures induced piezoelectric vibrations in the crystallites caused severe distortion of the detected decay curves and hampered the determinations of T_1. In order to overcome this problem thin aluminium foil was wound around the samples to act as a Faraday shield. Mechanical vibration in the foil was suppressed by coating the surface with low temperature varnish.

5.9.2 METALS

The penetration of an rf field into a plane conducting surface is governed by the equation

$$H(d) = H(0) \exp(-d/\sigma)$$

where σ, the skin depth, is given by

$$\sigma = \rho/\pi\nu\mu \quad .$$

ρ is the resistivity, ν is the frequency of radiation and μ the permeability of the sample.

Because of the small skin depths at rf frequencies, NMR measurements are usually performed on samples of fine powder or thin foil. In the CW method the resonance lineshapes from bulk metallic samples are distorted by a linear mixing of the absorption and dispersion(74) modes and similar phase errors become apparent with the pulse technique(75). Measurements have been reported on single crystal specimens including aluminium(76), but the interpretation of the results involves some empirical assumptions being made about the degree of lineshape distortion. In this work good rf penetration was ensured by using fine powder specimens with dimensions approximately equal to the skin depth.

Most of the metal powders were obtained commercially, but the pure aluminium powders were prepared in the laboratory. In one process 2 mm diameter aluminium wire was fed through a Metallisation Mark 16 metal spraying pistol at a rate of 4 ft s^{-1} and the resulting powder collected in a large container of water. The pressures of the gas supplies to the pistol were found to be critical to the attainment of the fine powder required and were optimized to the following values:

Propane	40 psi	Oxygen	38 psi	Air	70 psi.

After repeated washes with analar grade methanol the collected powder was rinsed with acetone and dried. It was then passed through a series of filters. Typical yields were as shown below:

GRAIN SIZE µm	% OF TOTAL WEIGHT
> 76	10
44-76	40
37-44	15
< 37	35

These powders were prepared from two grades of aluminium wire. The purer grade was obtained from Johnson Matthey Chemicals and had a quoted maximum impurity content of 50 ppm, the majority constituent of which was magnesium. The other grade of wire was as supplied directly by Metallisation Limited for industrial use and had a purity of approximately 99.5%.

In a second method of sample preparation a tungsten carbide coated file was used to file powder from a 5 9's pure aluminium ingot obtained from Koch-Light Laboratories. After sieving, the powder was passed several times through a high inhomogeneous magnetic field in an attempt to remove all ferromagnetic impurities.

The aluminium specimens were annealed by subjecting them to a temperature of 250°C for a period of two hours, under a vacuum of better than 2×10^{-6} torr. No problems of sintering were experienced, so the powders were annealed loose in small glass boats and then allowed to cool down overnight.

Surface oxidation of the metals afforded electrical insulation between neighbouring crystallites in the loose powders. However, with the exception of aluminium, the stresses induced by rapid rotation of the powder samples resulted in a welding together of the individual grains. To overcome this effect the powders were combined with a low viscosity resin mix - araldite 753/HY 951 hardener. In order to maximize the specimen density the uncured mixture of resin and powder was centrifuged in cylindrical teflon moulds. After curing under an infra-red lamp, the solid slugs of powder and resin formed at the bottom of the moulds were machined to size, etched with acid and then pressed into the rotor sample chambers.

CHAPTER 6

MEASUREMENTS ON THE SPIN-LATTICE RELAXATION TIMES IN THE CUPROUS HALIDES

6.1 INTRODUCTION

The work described in this chapter deals with T_1 measurements on samples of the three solid cuprous halides. Interest in these compounds first arose from their use as reference samples in the accurate measurement of the Knight shift of ^{63}Cu and ^{65}Cu in metallic copper by the macroscopic rotation technique(67). Accurate values of their chemical shifts were obtained at the same time(77). It was decided to extend the investigation of these compounds to the measurement of their spin-lattice relaxation times.

The cuprous halides have a zinc blende structure, the copper and halogen atoms lying on separate FCC sites displaced from each other by one-quarter of the distance along the body diagonal. Hence each atom is surrounded tetrahedrally by four atoms of the opposite kind. Despite the lack of any secular quadrupole interaction in crystals having cubic symmetry, time dependent quadrupole interactions arise from the distortion of the nuclear symmetry by lattice phonons. The nuclear spin relaxation mechanism generated by the lattice vibrational modes proves to be dominant over a large temperature range in these compounds.

6.2 RESULTS AND DISCUSSION

As stated in Section 2.3.5 Mieher's expression for the spin-lattice relaxation time arising from the Raman two phonon process in zinc blende type lattices is given by

$$\frac{1}{T_1} = A\, f(I)\left(\frac{e^2\gamma Q}{r^5}\right)^2 T^{*2}\, E(T^*) \qquad (6.1)$$

where $A = 1983/\pi d^2 v^3 a^3$ and $f(I) = (2I + 3)/I^2(2I - 1)$. The function $E(T^*)$ was originally evaluated by Van Kranendonk(22) and the results confirmed experimentally by Mieher(23). Values of this function in the range $T^* = 0.1$ to $T^* = 1.0$ are tabulated below.

T*	0.1	0.2	0.3	0.4	0.5	0.6	0.7	0.8	0.9	1.0
E	0.044	0.318	0.569	0.719	0.804	0.860	0.895	0.918	0.934	0.947

The low and high temperature expansions of $E(T^*)$ are

$$T^* \lesssim 0.02 \qquad E = 1.4 \times 10^4\, T^{*5}$$

$$T^* \gtrsim 0.5 \qquad E = 1 - 0.056/T^{*2}.$$

The five powder samples used are described in Section 5.9 and the experimental method is described in Chapter 5. Equation (6.1) was found to describe correctly the temperature dependence of the experimental spin-lattice relaxation times in these samples. Figure 6.1 shows the T_1 values of the two copper isotopes in the different specimens and the results from the two bromine isotopes are shown in Figure 6.2. The full lines are calculated from Van Kranendonk's function $[T^{*2}E(T^*)]^{-1}$ by choosing values of the Debye temperature

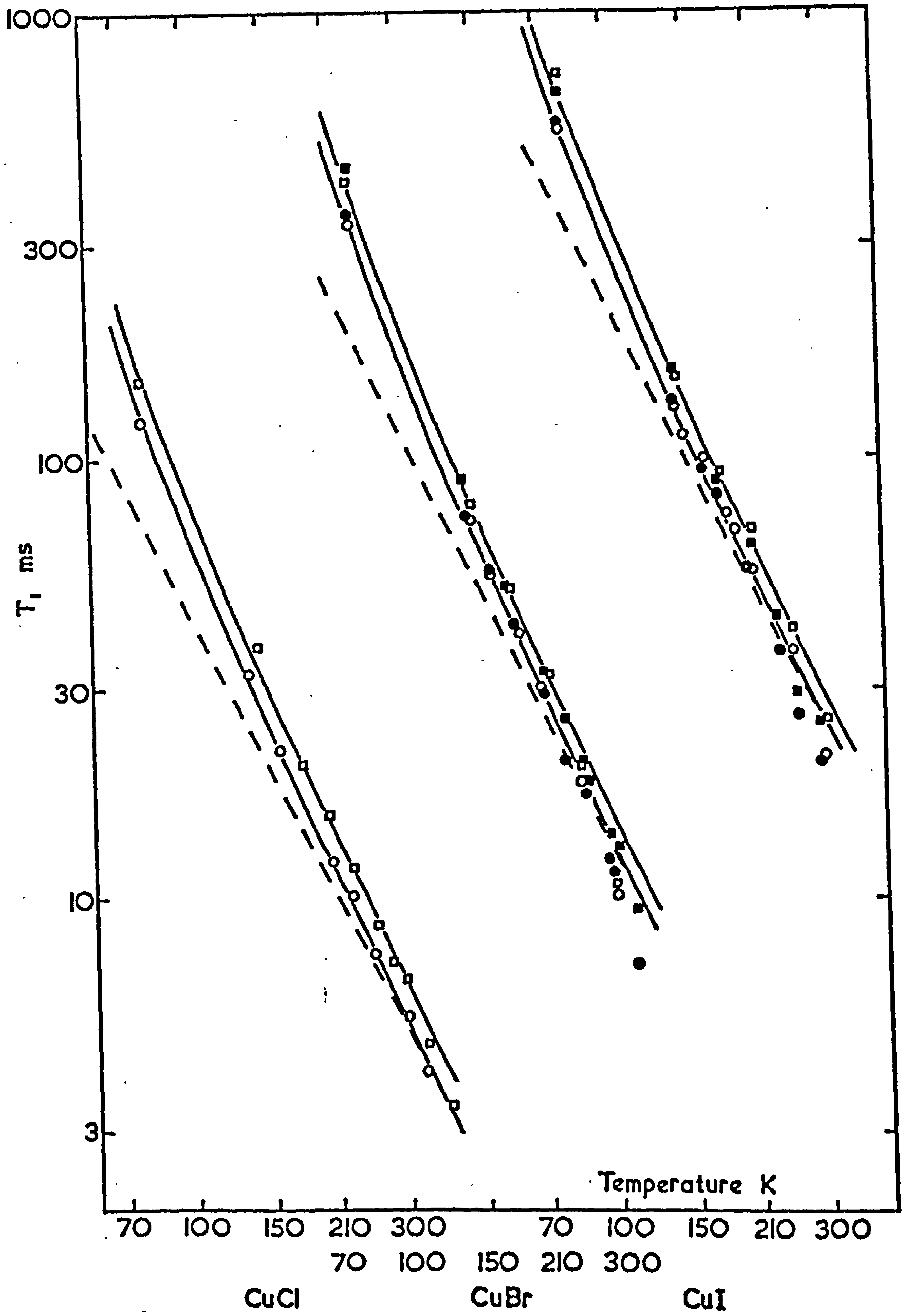

FIGURE 6.1 : Measured T_1 values of ^{63}Cu (circles) and ^{65}Cu (squares) in CuCl, CuBr and CuI. Measurements on the purer specimens are shown blocked in. The full lines are theoretical according to the expression in equation 6.1

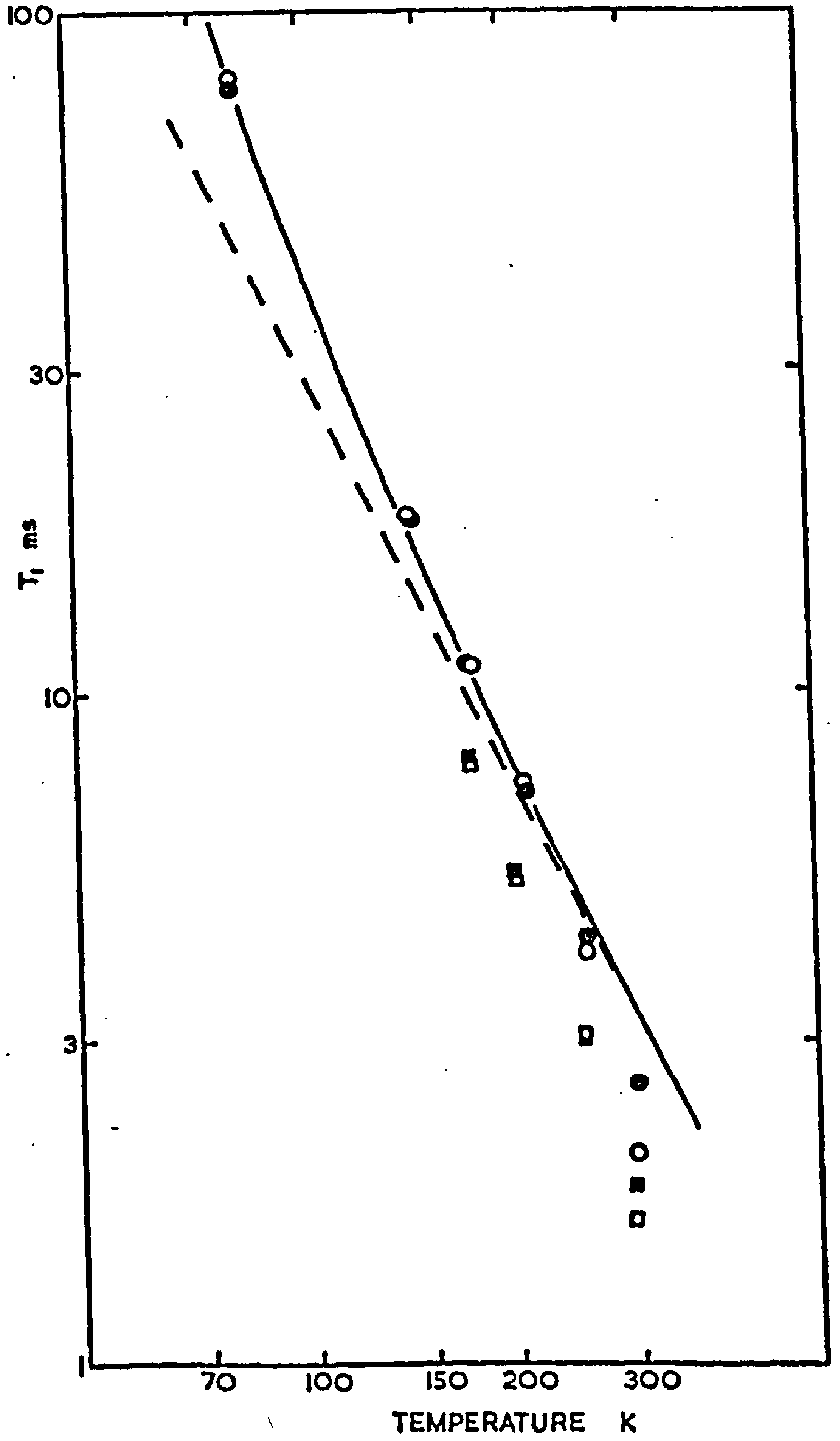

FIGURE 6.2 : Measured T_1 values of ^{79}Br (squares) and ^{81}Br (circles) in CuBr. The blocked in points again refer to the purer specimen. The full line is theoretical according to the function given in equation 6.1. The broken line shows the T^{-2} dependence at higher temperatures

in each case so as to give the best fit to the experimental data. The same values of θ_D were used for both ^{63}Cu and ^{65}Cu in each halide and also for ^{81}Br in the samples of cuprous bromide.

From Figures 6.1 and 6.2 it can be seen that although at lower temperatures Van Kranendonk's function fits the data well, at higher temperatures the T_1 values from all three halides fall progressively below the theoretical curves. This probably arises from a contribution to the overall spin-lattice relaxation time from increasingly rapid ionic diffusion, as has been noted elsewhere(78,79). Nevertheless the general tendency for T_1 to decrease asymptotically to a T^{-2} behaviour at higher temperatures, but deviate from such a temperature dependence at lower temperatures is still apparent.

The values of T_1 from the two specimens of cuprous bromide are in very close agreement for ^{63}Cu, ^{65}Cu and ^{81}Br over the entire temperature range. The same is also true of the copper isotopes in the two cuprous iodide specimens of differing purity, showing that over the range of measurements the recorded T_1 values were largely insensitive to sample purity or origin.

The Debye temperatures found for each of the three cuprous halides are shown in Table 6.1. The choice of value of θ_D needed to secure agreement between theory and experiment is not critical so there is an uncertainty of approximately ±25 K in the values quoted. Previous estimates of θ_D as found from T_1 measurements on pure single crystals of CuCl and CuBr(80) and a powdered sample of CuI(81) are included in the same table. The Debye temperatures given by Domngang and Wucher for CuCl and CuBr are in reasonable agreement with those quoted here, but there is some discrepancy in the two values for CuI. This may simply reflect the insensitivity

TABLE 6.1. DEBYE TEMPERATURES GIVING BEST THEORETICAL FIT TO EXPERIMENTAL T_1 VALUES

SAMPLE	DEBYE TEMPERATURE θ_D K	PREVIOUS ESTIMATES θ_D K
CuCl	275 ± 25	300 ± 30
CuBr	275 ± 25	280 ± 20
CuI	240 ± 30	170 ± 30

of the theoretical curve to the precise choice of θ_D. No other experimental estimates of the Debye temperatures in the cuprous halides could be found in the literature. Specific heat measurements will not in any case lead to identical values of θ_D, because the functional dependence on the lattice dynamics is slightly different from that of the quadrupolar relaxation rate. In the Debye theory specific heats are evaluated from integral expressions of the form

$$T^3 \int_0^{\theta_D/T} \frac{\rho(x)x^2e^x}{(e^x - 1)^2}\, dx$$

whereas Van Kranendonk's calculated transition probabilities are given by

$$T^3 \int_0^{\theta_D/T} \frac{\rho^2(x)e^x}{x^2(e^x - 1)^2}\, L_n(cTx/\theta)dx$$

with $x = h\nu/kT$ and $c = (6\pi^2)^{1/3}$. The functions L_n are complicated and depend upon the particular lattice type.

Guenther and Hultsch(79) have reported measurements on the spin-lattice relaxation times of ^{63}Cu in the cuprous halides over the temperature range 77-600 K, but no estimates of Debye temperatures were included. Indeed their results indicated that for all three compounds, in the temperature range 77-300 K, the temperature dependence was best described by a relationship of the form $T_1 = cT^{-x}$ where x takes the values 1.7, 2.0 and 2.1 for CuI, CuBr and CuCl respectively. The results for CuCl and CuBr are a reasonable approximation to the functional form of equation (6.1) for temperatures above about $\frac{1}{2}\theta_D$. However, Guenther and Hultsch's low temperature experimental T_1 values for all three cuprous halides, and CuI in particular, are shorter than those reported here. This suggests a possible contribution to the measured spin-lattice relaxation times from paramagnetic impurities, perhaps an excess of copper ions as they themselves note in the case of CuI.

From equation (6.1) it follows that in each of the halides the ratio of T_1 for ^{65}Cu to that for ^{63}Cu should be equal to $(^{63}Q/^{65}Q)^2$. From pure quadrupole resonance measurements $(^{63}Q/^{65}Q)^2$ is equal to 1.168 ± 0.001(82). Table 6.2 lists the ratio of T_1 values for ^{65}Cu and ^{63}Cu as found over the temperature range of the theoretical fit to Van Kranendonk's function. The results from all three cuprous halides can be seen to be in satisfactory agreement with the theory.

Over the limited temperature range of measurements on ^{79}Br the ratio of T_1 values for ^{81}Br and ^{79}Br was 1.35 ± 0.10. The value for $(^{79}Q/^{81}Q)^2$ as derived from direct measurement of the ratio of the quadrupole moments is 1.433 ± 0.002(83). The agreement between the two values is reasonable.

The ratio of the measured T_1 values for ^{63}Cu and ^{81}Br in CuBr was also independent of temperature. Domngang and Wucher(80)

TABLE 6.2. RATIO OF T_1 VALUES FOR ^{65}Cu AND ^{63}Cu OVER TEMPERATURE RANGE OF THEORETICAL FIT TO VAN KRANENDONK'S FUNCTION

SAMPLE	RATIO T_1Cu^{65}/T_1Cu^{63}
CuCl	1.18 ± 0.10
CuBr	1.19 ± 0.05
CuI	1.18 ± 0.05

reported that in their pure single crystal sample the ratio of T_1 values for the copper and bromine isotopes varied. However, this variation only really became apparent at liquid nitrogen temperatures and below. The form of this behaviour was attributed to the different relative contributions to the overall spin-lattice relaxation times of optical phonons, which are not taken specific account of in the Debye model of the lattice phonon spectrum. The quadrupole moment ratios of the copper and bromine isotopes have been determined separately to a considerable degree of accuracy but there is some uncertainty in the absolute values of Q. Using the quoted values for ^{63}Cu and ^{81}Br respectively of -0.16 ± 0.03(84) and 0.28 ± 0.02(83) in units of 10^{-28} m^2 the ratio $(^{63}Q/^{81}Q)^{-2}$ is equal to 3.1 ± 1.6. The experimental value found over the measured temperature range was 4.0 ± 0.3, in reasonable agreement with the figure of 4.3 determined by Domngang and Wucher at the higher temperatures of their range of measurements. The theoretical and experimental ratios agree to within the large error limits imposed by the uncertainty in the values of Q. However, unlike the comparison of relaxation times for the two copper or two bromine isotopes it cannot be assumed that anti-shielding, covalency and other effects are identical at the different ionic sites. Thus the factors γ will in principle differ for the two nuclei. The theory is satisfied if the ratio ${}^{81}\gamma/{}^{63}\gamma$ has the value 1.14 ± 0.30.

In the simple ionic model of the crystal lattice the magnitude of the effective quadrupolar coupling for any nucleus is determined by the Sternheimer anti-shielding factor γ_∞(3). Theoretical values of γ_∞ depend to some extent upon the calculation procedure adopted but for the copper and bromine ions may be taken as -15 and -123 respectively(85). It follows that the ratio of the corresponding γ values - given by $(1 - \gamma_\infty)$ - is in disagreement with the previously determined figure of 1.14. Experimental estimates of the anti-shielding factors for the halide ions differ quite considerably from the theoretical values. However, even when an average experimental value of -35 is taken for Br^-(86) there is still a considerable discrepancy in the ratio ${}^{81}\gamma/{}^{63}\gamma$ predicted by anti-shielding effects alone and that found from measurements of T_1. In view of the fact that the cuprous halides are covalent the disagreement is perhaps hardly surprising.

A detailed comparison of T_1 values between the different cuprous halides is precluded by the absence of any reliable values for γ as well as by the lack of any reported data on the velocity of sound in these compounds. Nevertheless by making some simplifying assumptions an approximate calculation can be made. The values of T_1 for ${}^{63}Cu$ in the three halides at a temperature of 200 K are listed in Table 6.3. This temperature is chosen because,

TABLE 6.3. DEPENDENCE OF T_1 ON LATTICE PARAMETER a

SAMPLE	T_1 (ms) at 200 K	a (10^{-10} m)	a^{13} (10^{-121} m^{13})	T_1a^{-13} (10^{118} m^{-13} s)
CuCl	12.4	5.406	3.37	3.7
CuBr	31	5.691	6.58	4.7
CuI	59	6.043	14.31	4.1

although E(T*) has almost reached unity for all three halides, it is below the point at which ionic diffusion contributes to the overall relaxation time in any of the samples. From equation (6.1) and with the assumption that E(T*) is the same for each halide, the relaxation times obey the relationship

$$T_1 \propto d^3v^3\gamma^{-2}\theta_D^2a^{13} \quad .$$

The velocity of sound v is given by $\sqrt{C/d}$ where C is the appropriate elastic constant. Hence

$$T_1 \propto d^{\frac{1}{2}}C^{3/2}\gamma^{-2}\theta_D^2a^{13} \quad .$$

Although the value of $d^{\frac{1}{2}}$ increases by 17% from CuCl through CuBr to CuI$^{(87)}$, θ_D^2 (from the values reported above) decreases by 24%. Consequently the product $d^{\frac{1}{2}}\theta_D^2$ remains approximately constant. The variations of C and γ over the range of cuprous halides are not known but may reasonably be assumed to be small. In that case the five-fold increase in T_1 from CuCl to CuI must be attributed to the change in the factor a^{13}. Using the values of lattice parameter a quoted by Wyckoff(88) (but ignoring effects due to the thermal expansion of the lattice) the product $T_1 a^{-13}$ as listed in Table 6.3 can be seen to be constant to within ±12%. Therefore the range of T_1 values between the cuprous halides appears simply to reflect the strong dependence of the quadrupole interactions on the interatomic distance.

The above finding is somewhat in contradiction to that recorded by Guenther and Hultsch(78). They interpreted a decrease in the ratio of their calculated to measured T_1 values over the cuprous halides as being consistent with the reported variation in the degree of covalent bonding in these compounds: CuCl being the most covalent and CuI the least. An increased amount of covalency in the lattice bond is usually associated with a paramagnetic shift in the resonance frequency(26). However chemical shift measurements(77,78) do not show such a correlation in the cuprous halides.

Evaluation of the absolute agreement between theory and experiment depends upon the accuracy to which the individual components of equation (6.1) are known. In calculating the spin-lattice relaxation time of ^{63}Cu in CuCl at 200 K the following values were used: $I = 3/2$, $d = 4.14 \times 10^3$ kg m^{-3} (87), $a = 5.406 \times 10^{-10}$ m (88), $Q = -0.16 \times 10^{-28}$ m^2 (84), $E(T^*) = 1$. In the absence of any better estimate the velocity of sound v was taken as 3.5×10^3 m s^{-1} as reported for AgCl(89). The resulting value for T_1 is then $9.46 \times 10^3\ \gamma^{-2}$ s compared to the measured value of 12.4 m s. It follows that a value of $\gamma \sim 10^3$ is required to secure agreement between experiment and theory. Similar values for γ have been determined from T_1 measurements on some alkali halides(22,90). This provides further evidence that refinements to Van Kranendonk's and Mieher's theories, other than those arising from simple anti-shielding considerations alone, are needed to achieve quantitative agreement with experiment.

One line of approach to the solution of this discrepancy is the more recent development by Van Kranendonk and Walker(21). Their detailed consideration of a second order anharmonic Raman relaxation process has thrown doubt onto the absolute importance of the direct Raman relaxation mechanism. The second order process takes place via a combination of the direct single phonon spin-lattice coupling and the cubic anharmonic lattice forces: in effect the Raman change in phonon energy corresponding to a transition between nuclear spin states is preceeded by an intermediate single phonon state. The theory as developed for the point charge model of NaCl type crystal lattices leads to the expression

$$W_{aR} = 27\gamma_G^2 \frac{c_1^2 + 4c_2^2}{d_1^2 + 4d_2^2} W_{1R} \qquad (6.2)$$

where W_{aR} and W_{1R} are the anharmonic and first order Raman relaxation rates respectively; c_1, c_2, d_1 and d_2 are spin-lattice coupling constants and γ_G is the Grüneisen constant. For the alkali halides, the anharmonic relaxation mechanism given by equation (6.2) predicts relaxation times a factor of 100 shorter than the first order Raman process, which brings theory and experiment into much closer accord. Although the appropriate values of c_{12} and d_{12} for the more covalent zinc blende lattice are unknown, a relaxation mechanism of similar magnitude would obviously secure a similar agreement in the cuprous halides. The temperature dependence of the anharmonic Raman process is identical to the first order process. Consequently the lack of knowledge of the overall values of γ prevents any definite conclusion as to the validity of the indirect second order process in the cuprous halides.

CHAPTER 7

EXPERIMENTAL RESULTS ON ALUMINIUM METAL

7.1 INTRODUCTION TO THE MEASUREMENTS UNDERTAKEN

The results reported in this chapter deal with a series of measurements on aluminium of various NMR parameters. Although many of the parameters are well documented in the literature there has been some discrepancy in the past between experiment and theory, particularly over the values of second moment and T_{1D}. The macroscopic rotation technique has proved useful previously in the determination of accurate values of chemical shifts(47,77) and Knight shifts(67) and has been applied here with similar success.

Because of the limitations imposed by the small skin depths, powdered samples are normally used for NMR observations. An important aspect of the work reported below was the preparation of the specimens of aluminium powder, as described in detail in Section 5.9. In this chapter the three different annealed powder samples prepared in the laboratory will be referred to as follows:

(a) - powder prepared from the 99.995% pure wire by the metal spraying technique;

(b) - powder prepared from the nominally 99.5% pure wire by metal spraying;

(c) - powder filed from a 99.999% pure ingot.

A fourth type of aluminium powder (d) was used unannealed in the Knight shift measurements. This was obtained commercially from Koch-Light Laboratories and had a quoted purity of 99% with a particle size of 8-15 μm.

7.2 THE ACCURATE DETERMINATION OF THE ALUMINIUM KNIGHT SHIFT

7.2.1 INTRODUCTION

Knight shift values provide a direct comparison of the magnitudes of the internal magnetic fields present at the sites of a particular nuclear species in the metallic state and in a chosen reference material. Most information about the metallic state would be obtained by using an isolated atom as the reference, but this is obviously not practical. Consequently measured Knight shifts depend to some extent on the chemical shift interaction present in the reference sample. For many metals the experimental isotropic Knight shift is largely attributable to the direct contact term given by equation (2.10). However, very often further terms - as discussed briefly in Section 2.2.3(b) - also have to be considered in order to obtain absolute agreement between theory and experiment.

Previous experimental estimates of the Knight shift of aluminium at room temperature(76,91-95) have all been in the range 1.50 to 1.68×10^{-3}, the generally accepted value being 1.61×10^{-3}. In most cases the reference sample was an aqueous solution of $AlCl_3$. Ultimately any Knight shift determination is dependent upon the accuracy of the measurements of frequency or magnetic field and the precision with which the centre of the nuclear resonance spectra of the metal and reference can be defined. The width of the

Lorentzian NMR lineshape of $AlCl_3$ solution depends in the first instance upon the homogeneity of the external magnetic field. On the other hand the ^{27}Al resonance line is approximately Gaussian with a width of about 9 kHz. Even if the line centre is located to an accuracy of 2% of the width, the greatest accuracy to which the Knight shift can be determined in a magnetic field of around 1 tesla is $\pm 0.02 \times 10^{-3}$.

Aluminium has a cubic structure at room temperature with only one naturally occurring isotope. The broadening of the resonance line from a pure annealed powdered specimen of this metal arises from the magnetic dipolar interaction between nuclei. The rapid rotation technique can be used therefore to narrow the resonance lineshape. This enables the line centre and hence the Knight shift to be determined to a correspondingly greater accuracy.

7.2.2 MEASUREMENTS

Experimental measurements were undertaken following the procedure described in Section 5.5. Using compressed air, rotors containing the aluminium powder samples were spun about the magic angle at spinning frequencies of about 4 kHz. At these speeds the width of the resonance lineshape is reduced by a factor of approximately 15. (Typical FIDs and Fourier transformed lineshapes obtained from static and rotating pure powder specimens are included in Figures 7.1 and 7.2 respectively.) The reference material used was a saturated aqueous solution of 99.999% pure $AlCl_3$ as supplied by Johnson Matthey Chemicals. The solution was enclosed inside a nylon container, the internal dimensions of which were identical to those of the rotor sample chamber. All measurements were recorded at room temperature (295 K) in a magnetic field of 1.35 T. With the PSD in quadrature phase at high gain, resonance frequencies could be determined precisely from the detected signal by fine adjustment of the dial settings on the frequency synthesiser.

In obtaining each Knight shift value a series of comparisons of the resonance frequencies of the metal and reference material were made. After a small correction of up to 10 Hz to account for a very slight difference in the magnetic fields at the rotor and the reference sample (see Section 5.5) the Knight shifts were calculated from the equation $(\nu_m - \nu_r)/\nu_r$. Several separate determinations were made, changing the samples used and also varying slightly the rotation rate and the magnetic field. From eight different series of measurements the mean value of the aluminium Knight shift was 1640.0 ppm and the extreme values were 1638.9 and 1640.7 ppm. The estimated possible error in the measured resonance frequency of each sample was ±5 Hz. Similar errors in determining the magnitude of the applied correction lead to an overall estimate of the total possible error in each determination of $(\nu_m - \nu_r)$ of ±20 Hz. Hence with ν_r equal to 15 MHz the maximum possible error in any single Knight shift estimate was approximately ±1.3 ppm.

Three specimens of aluminium powder were used in the measurements: (a), (b) and (d). Powders prepared from the two grades of aluminium wire ((a) and (b)) were sieved so that the maximum particle size was limited to 44 μm. Originally the powder specimens were encapsulated in epoxy resin in the manner described in Section 5.9. This was later found to be unnecessary so the powders were packed directly into the rotor sample chambers which were then sealed at the top with epoxy glue. There was no measurable difference in the Knight shift values obtained from any of the three powder samples whether they were encapsulated in the resin or not.

Various aqueous solutions of $AlCl_3$ were also compared, but the value of the reference frequency ν_m was found to be unaffected by concentration or by use of 99% reagent grade $AlCl_3$ instead of the pure salt. In fact no change in resonant frequency was observed even when aqueous solutions of reagent grade $AlBr_3$ were substituted. The value of the aluminium Knight shift quoted above is therefore largely insensitive to the concentration of impurities in the metal sample or the choice of reference solution.

We now consider other factors which might affect the Knight shift value obtained.

7.2.3 POSSIBLE FACTORS INFLUENCING THE EXPERIMENTAL KNIGHT SHIFT VALUE

(a) Temperature. Although at first sight all measurements were undertaken at laboratory temperature, the temperature of the rotors could not be monitored precisely. Due to cooling upon expansion the temperature of the driving gas immediately after passing through the jets in the stator was several degrees below room temperature. However, as would be expected, any variation from room temperature of the temperature of the samples was found to be small - less than 3 K. The temperature dependence of the aluminium Knight shift is relatively small. The most recent reported measurements by Kushida and Murphy(96) and El-Hanany and Zamir(95) indicate that an error of about 15 K would be required to produce an uncertainty of 1 ppm.

Consequently any resulting inaccuracy in the Knight shift value quoted here is much smaller than the experimental error.

(b) Pressure. For those specimens of aluminium powder encapsulated in resin the magnitude of the rotationally induced stresses can be estimated using the expressions given in Section 4.2.3. The maximum stresses in a rotating solid cylinder occur at the rotation axis where $\sigma_t = \sigma_r = 1/8(3 + \mu)\rho b^2\omega^2$. The density of the aluminium powder slugs was found to be 1.6 g cm^{-3}. The precise value of μ is unknown but can be assumed to be less than but approximately equal to $\frac{1}{2}$. Consequently at a rotation speed of 4 kHz the maximum pressures generated within the specimen are approximately 0.8×10^7 N m^{-2}. The same stress equations cannot automatically be applied to those powder samples packed directly into the rotors. However with the assumption that the metal powder can be considered as an isotropic viscous fluid, it can be shown by elementary calculation that the radial stress generated in the specimen is approximately $\frac{1}{2}\rho r^2\omega^2$ (59). The maximum stress acts therefore at the periphery of the sample. At the rotation speed employed of 4 kHz (and substituting the density of aluminium metal for ρ) this pressure is given by 1.4×10^7 N m^{-2}.

Kushida and Murphy(96) found that for a hydrostatic pressure of 10^9 N m^{-2} the fractional increase in the aluminium Knight shift was 1.31%. Hence, with the assumption that rotation and hydrostatic pressures are comparable in their effects, the expected variation in the Knight shift at the highest rotationally generated stress is 0.3 ppm. The mean pressure shift will lie within this value. It follows that such effects have a negligible influence on the experimental Knight shift value obtained.

(c) Bulk Susceptibility Effects. The magnetic field experienced at any nuclear site is modified slightly from the applied external field by the bulk susceptibility of the sample material. The effective magnetic field H'_o is given by(97)

$$H_o\left[1 + \left(\frac{4\pi}{3} - \alpha\right)\chi_v\right] \tag{7.1}$$

where χ_v is the magnetic susceptibility per unit volume and α is a numerical factor depending upon the shape of the sample. For a spherical sample $\alpha = 4\pi/3$ so $H'_o = H_o$ whereas for an infinitely long rod $\alpha = 2\pi$. In the case considered here the sample is a cylinder inclined at an angle of 54^o 44' to the applied magnetic field and with a length slightly greater than the diameter. An exact calculation of the effect of bulk susceptibility for the aluminium powder samples is precluded by ignorance of the appropriate value of α for this configuration. However, an estimate of the induced magnetic field can be made by approximating the sample to a prolate ellipsoid aligned perpendicularly to the magnetic field. If the ratio of the polar to equatorial axes is set as 3:2, α is then equal to $4\pi \times 0.38$ (98).

The quantity of metal in the centrifuged resin slugs was found to be equivalent to that of the closely packed powders in the rotor sample chambers. The amount of metal by volume was about 30% in both cases. Taking the susceptibility per unit mass for aluminium as 0.65×10^{-6} cgs units (but ignoring a small diamagnetic contribution of the resin matrix) the volume susceptibility of the metal samples is given by 0.6×10^{-6} cgs units. When the above values for α and χ_v are substituted in equation (7.1) the resulting contribution to the magnetic field, and hence the resonance frequency, is approximately 0.4 ppm. We remark in passing that a separate calculation(99) has predicted that the bulk susceptibility effect will in fact be averaged out in a sample undergoing sufficiently rapid macroscopic rotation at the magic angle. The bulk susceptibility of the saturated $AlCl_3$ reference solutions is unknown but can probably be safely neglected in comparison to the metal. It follows that the possible contribution of the sample bulk susceptibilities to the experimental Knight shift is less than the experimental error.

(d) Other Effects. For small grain aluminium powders the Knight shift has been reported to be dependent upon particle size(100), but this effect has only been detected at temperatures below 4 K and for particle sizes under 100 Å. Field dependent oscillations in the Knight shift due to the de Haas Van Alphen effect have been measured at very low temperatures(101). The magnitude of these oscillations is small and the average Knight shift value was found to be unaffected. Both of these effects should be negligible at room temperatures.

In conclusion it can be stated that neglecting the possibility of unsuspected systematic errors, the experimental value of the isotropic Knight shift was 1640 ppm with a maximum possible error in measurement of ±1 ppm. If a possible contribution due to the bulk susceptibility of the aluminium samples is included the error limits should probably be extended to +1 and -2 ppm. From a detailed theoretical calculation Shyu, Das and Gaspari(102) obtained a value for the aluminium Knight shift of 1624 ppm. Although their analysis included a core polarization correction it did not take into account any possible differences in the chemical shift interaction of the aluminium nuclei in the metal and reference compound. A considerable improvement in the accuracy of Knight shift calculations will be necessary to enable a precise comparison between theory and experiment to be made. However the value reported here of 1.640×10^{-3} does show a small but significant departure from the previously accepted estimate of 1.61×10^{-3}.

7.3 RECORDED LINESHAPES AND SECOND MOMENT VALUES

7.3.1 INTRODUCTION

Although theory is unable to predict the exact form of the absorption spectrum, a comparison between the theoretical and experimental second moments can be made. ^{27}Al is the only naturally occurring aluminium isotope. It occupies a FCC lattice, the lattice constant being 4.0496 Å. From this the dipolar second moment predicted by Van Vleck's calculation(16) is 9.18 kHz^2 (7.44 G^2). (It has also been quoted as 9.42 kHz^2 (7.63 G^2).) Previous experimental determinations on pure annealed specimens have consistently yielded values above this in the range 11.8 to 15.4 kHz^2 (9.5-12.5 G^2)(72,103-110). The discrepancy between theory and experiment is well known. In the main it has been attributed to a nuclear quadrupole interaction, but the mechanism for such an interaction has never been demonstrated conclusively.

7.3.2 MEASUREMENTS

The resonance spectra of the static aluminium powders were obtained by Fourier transformation of the detected FIDs as detailed in Section 5.6. In each case about 1 cm^3 of the loose annealed aluminium powder was placed in the standard Bruker probe system. The measurements were recorded at temperatures in the range 290-300 K using resonant frequencies of 15 and 16 MHz, but the results obtained were insensitive to these variations.

Powders (a) and (b) were sieved so as to separate the specimen particle sizes so: 37 μm, 37-44 μm, and 44-76 μm. A few drops of pure acetone were added to the largest grain specimens in order to reduce distortion of the detected signals by mechanical vibrations set up in individual crystallites. The problem could not be cured by the powders being encapsulated in resin because the widths of the resonance spectra of the cured slugs were found to be increased by this treatment. (That this broadening was due to a quadrupole interaction rather than any stress induced distribution of Knight shifts was made evident by its partial removal upon rapid rotation of the specimens about the magic angle.) Owing to the small skin depth (∿ 20 μm) the signal intensities obtained from the coarsest powders were less than those from the finer powders. However, within the limits of experimental error, the transformed lineshapes were found to be unaffected by particle size.

The observed characteristic decay shapes from powder samples, (a) and (c), were quite distinguishable from each other. (Powder (c) was filtered to a particle size of less than 44 μm.) Typical FIDs obtained from these two samples are shown in Figure 7.1 together with the corresponding lineshapes in the frequency domain. The FID and absorption spectrum of powder (b) were very similar in appearance to those obtained for (c), and are therefore not illustrated separately.

The tails of nuclear spectra in the frequency domain are determined largely by the supposition made about the behaviour of the FID

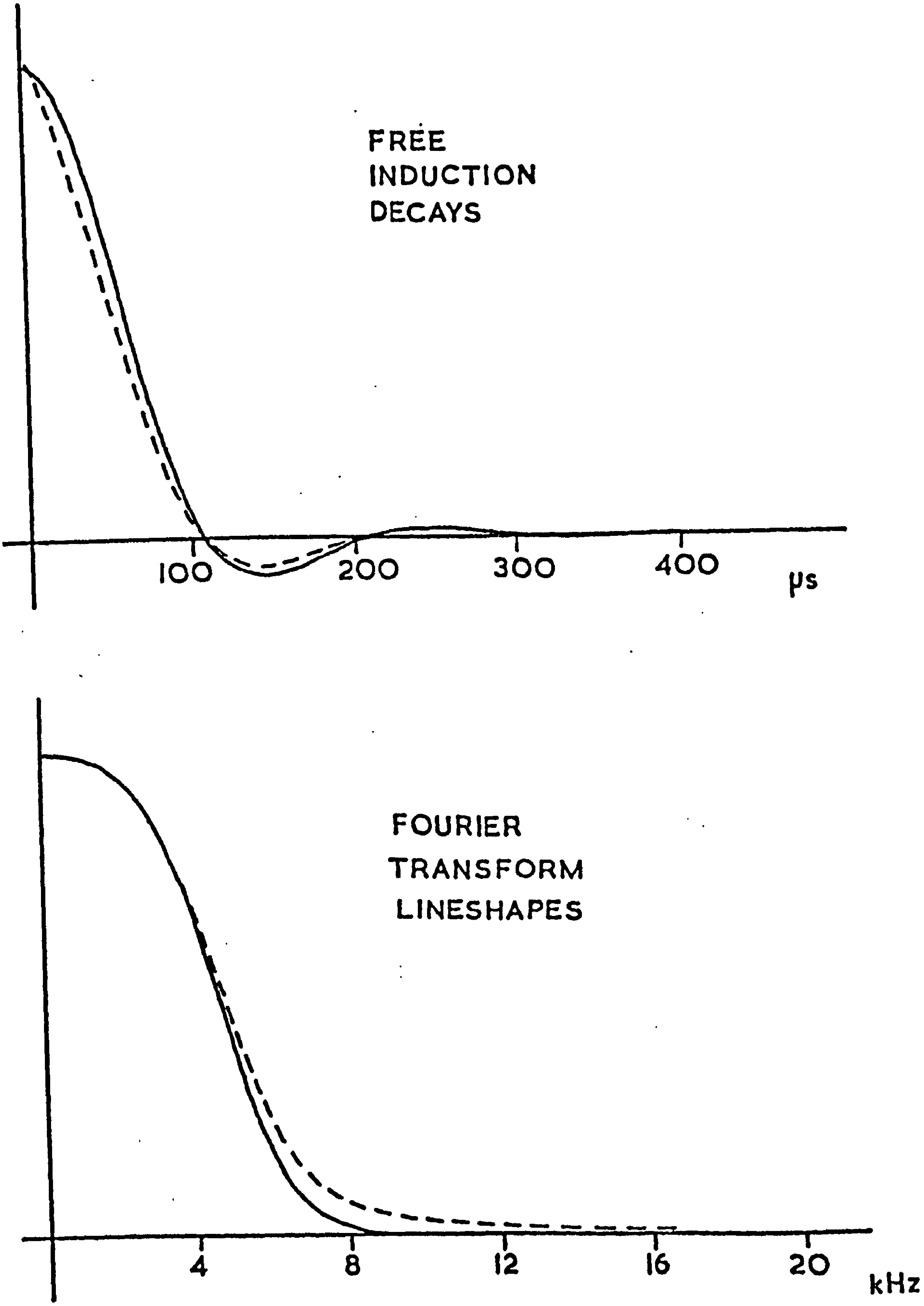

FIGURE 7.1 : ^{27}Al F.I.Ds and corresponding spectra in the frequency domain for annealed powder prepared by the metal spraying gun (full line) and filing (broken line)

near the time origin. By using the solid echo (and Jeener and Brockaert) pulse sequence it was shown that the decay curves for sample (a) were Gaussian right back to the time origin. However this was not found to be the case for the other samples. Both the FIDs and the solid echo responses became more exponential than Gaussian close to zero time. The anomalously high values of second moment measured by other workers in samples similar to (c) are regarded generally as indicating the presence of a nuclear quadrupole interaction. If this is so, the validity of the data points predicted by the solid echo sequence is brought into question. The response following the $90\text{-}\tau\text{-}90_{90}$ sequence has been calculated for those cases where the internal spin interactions arise either from the dipolar coupling between spins(71) or from the first order quadrupole broadening in an imperfect cubic crystal(111), but not a combination of the two. Nevertheless for times less than T_2 the observed solid echoes were found to follow the shape of the FIDs. Consequently the FID dead time points were estimated so that the preliminary part of the decay envelope resembled the outline of the solid echo maximum.

Experimental values of the second and fourth moments are recorded in Table 7.1. The large variation in the second moment values of the different specimens is indicative of the relative Lorentzian character of the experimental lineshapes. The errors quoted refer to the spread of measured values about the mean. The large error values given for samples (b) and (c) arise out of the variation in the tails of the transformed lineshapes caused by the uncertainty in fitting the dead time points. These estimates do not however include any consideration of the contribution to the second moment

TABLE 7.1. COMPUTED SECOND AND FOURTH MOMENTS OF ALUMINIUM POWDERS

POWDER SAMPLE	SECOND MOMENT kHz^2	FOURTH MOMENT kHz^4
99.995% pure sprayed (a)	9.4 ± 0.4	$225 \pm^{80}_{30}$
99.999% pure filed (c)	$15 \pm^{2.5}_{2}$	-
99.5% pure sprayed (b)	$18 \pm^{4}_{2}$	-

summation from those for wings of the lineshapes which are indistinguishable from the base-line. With CW spectra the moments are measured from the absorption curve with some assumption made about the shape of the wings. The absolute accuracy of the computed values depends therefore upon the validity of this assumption. In this work the resolution of the computer output describing the transformed lineshape was in each case better than 1 part in 2000 so the summation procedure was extended right out to a point where the signal intensity was 1/2000 of that at ν_o. It was then truncated. Of course if the wings of a lineshape are truly Lorentzian then the second moment is infinite.

Measurements of fourth moment were confined to sample (a) because the long wings of the transformed lineshapes of the other samples made any estimate meaningless. The ratio M_4/M_2^2 for sample (a) is equal to 2.55 whereas for a Gaussian curve the expression is identically equal to three. The error limits, arising out of the uncertainty in the lineshape tails are large, but this result does serve to illustrate that the nuclear spectrum of the sprayed powder shown in Figure 7.1 can best be described as a flat topped Gaussian. This form of lineshape is further evident from the rather unusual shape of the corresponding FID, with an apparent beat structure imposed on top of a simple transient decay to the baseline.

As a check on the reliability of the measured second moments, CW measurements were carried out on two purer samples (a) and (c). The second moment values obtained in this way agreed with the values shown in Table 7.1.

7.3.3 DISCUSSION

High values of second moment have been recorded by other workers for specimens of thin foil and both commercial and filed powders. The experimental second moment obtained here for the powder filed from a pure ingot (c) is slightly higher than most of these values, but in view of the large possible error the agreement is reasonable. (One recent determination in particular put the second moment of a 6 9s pure filed sample as 12.5 G^2 (15.4 kHz^2).)(110) The second moment of 9.4 kHz^2 measured from the 99.995% pure sprayed powder (a) is markedly lower than the above values and in close agreement with the theoretical value of 9.2 kHz^2. Taken together the tabulated results from all three samples show that the measured second moment of annealed aluminium powder is sensitive to both purity and the manner of specimen preparation; the implication being that the lineshapes obtained from those specimens prepared by filing were distorted by some form of nuclear quadrupole interaction.

Besides the anomalously high experimental second moment values, other reported measurements have lent further support to the possibility of some sort of resonant quadrupole interaction being present in filed powder and thin foil specimens of aluminium metal. Spokas and Slichter(104) reported that at higher temperatures their measurements of the Hahn echo T_2 were consistent with a nuclear quadrupole coupling to long-range, slowly varying lattice strains of some sort. Similar results obtained by Fradin and Rowland(112) have supported this contention. Anderson and Redfield(18) considered that their anomalously high measured value for the ratio of the spin-lattice relaxation time in high and low external magnetic fields (δ) arose from a quadrupolar coupling, possibly even due to the presence of impurities. More recently Tunstall and Brown(72) interpreted a measured variation of δ against temperature in terms of a quadrupolar contribution to the local internal magnetic fields and showed how agreement between theory and experiment could then be improved. However in each of these cases the precise nature of the lattice defects producing the quadrupole coupling has still to be isolated satisfactorily.

The results reported here imply that lattice strains are introduced by the cold working of the metal to produce foil or fine particles. There are two ways in which such strains might arise: either through the introduction of impurities or by a distortion of the crystal lattice. Before annealing the second moments of the sprayed and filed powders were about 50% higher than the values stated in Table 7.1. (The same reduction caused by the annealing process has been reported by other workers in filed powders(110) and cold rolled foils(105).) Therefore it would appear that annealing successfully removes some strain mechanisms but leaves others. The presence of impurities introduced by the cold working process cannot be ruled out. Such impurities might exist separately as macroscopic particles or diffuse into the grains of aluminium themselves. Certainly our use of a tungsten carbide coated file did not prevent magnetic splinters from entering the filed powder initially. A detailed chemical analysis of filed powders and cold rolled foils would help in this respect.

In conclusion we note that there was a marked difference in appearance between the individual grains of the filed powder specimens and those prepared by the metal spraying technique. Under a microscope the filed particles were very irregular in shape whereas the sprayed particles tended to be elongated spheroids. However any surface effect would presumably have to be exceptionally long-ranged in order to account for the observed amount of broadening in the nuclear resonance spectra.

7.4 VARIATION OF LINESHAPE WITH ROTATION SPEED

7.4.1 INTRODUCTION

The aluminium resonance line may be narrowed by rapid rotation at the magic angle. No scalar broadening interaction of the type discussed in Section 2.1.4 is present in aluminium. Therefore it is predicted that the theoretical limit to the reduced central spectrum will be determined only by the homogeneity of the external magnetic field and the relaxation time of the aluminium nuclei. Kessemeier and Norberg(34) have spun aluminium at speeds up to 7.5 kHz and reported that the resonance signal was narrowed by a factor of 10. Above 4 kHz they found that the FID was made up of a Gaussian initial part and an exponential tail, the time constant of which exhibited a roughly linear dependence on the rotation rate. The linewidth of static aluminium powder is approximately 8 kHz, so it is expected that rotation rates considerably in excess of this value would be required to remove completely the internal dipolar interactions.

7.4.2 MEASUREMENTS

A specimen of powder (a) was used to measure the variation in the width of the resonance spectrum with rotation speed about the magic axis. The foil bearing rotor system was employed in a magnetic field of 1.45 T. As this type of rotor became warm after it had been running for some time it was not possible to measure the sample temperature accurately, but from T_1 measurements it was estimated on average to be about 325 K. Figure 7.2 shows the decay shapes together with the corresponding lineshapes in the frequency domain for two different rotation speeds. Measurements were limited to speeds above 2 kHz because below this the spinning frequencies could not be determined to any reasonable accuracy. The variation in the half-height linewidth of the central resonance line is shown in Figure 7.3.

The experimental linewidth plotted includes contributions from lifetime broadening and homogeneity of the magnetic field. Because of the large magnet gap the homogeneity of the applied field was relatively poor. The field gradient contribution to the static linewidth was estimated to be about 80 Hz, although the effective value would have been reduced upon rotation. Assuming that the spin-lattice relaxation time of aluminium at room temperature is 6 ms, the lifetime broadening contribution to the linewidth is approximately 50 Hz.

From Figure 7.3 it can be seen that at a rotation rate of 7.7 kHz the central component of the absorption lineshape is still narrowing

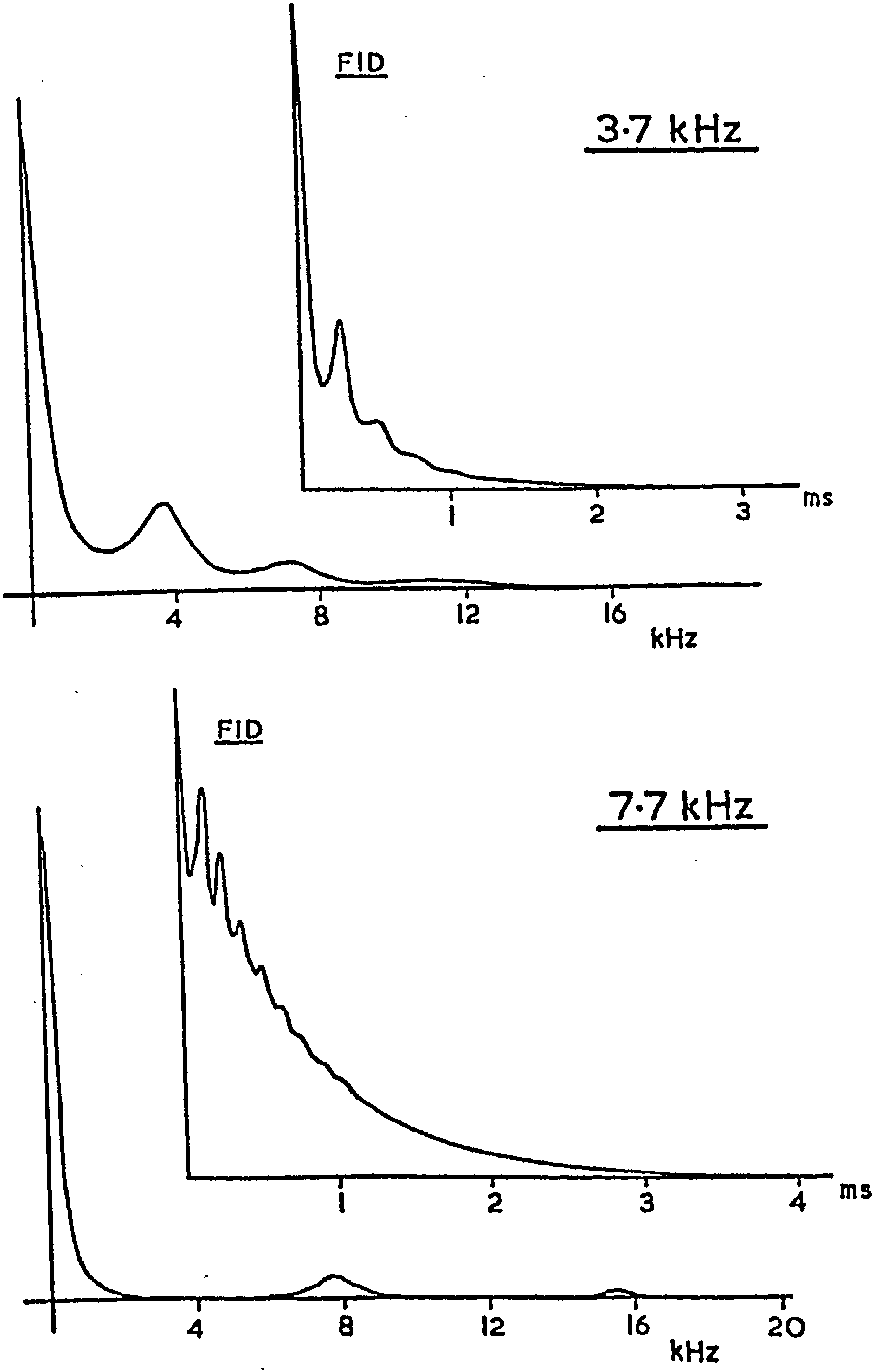

FIGURE 7.2 : ^{27}Al F.I.Ds and fourier transform lineshapes for pure annealed powder rotated at two different frequencies about the magic axis

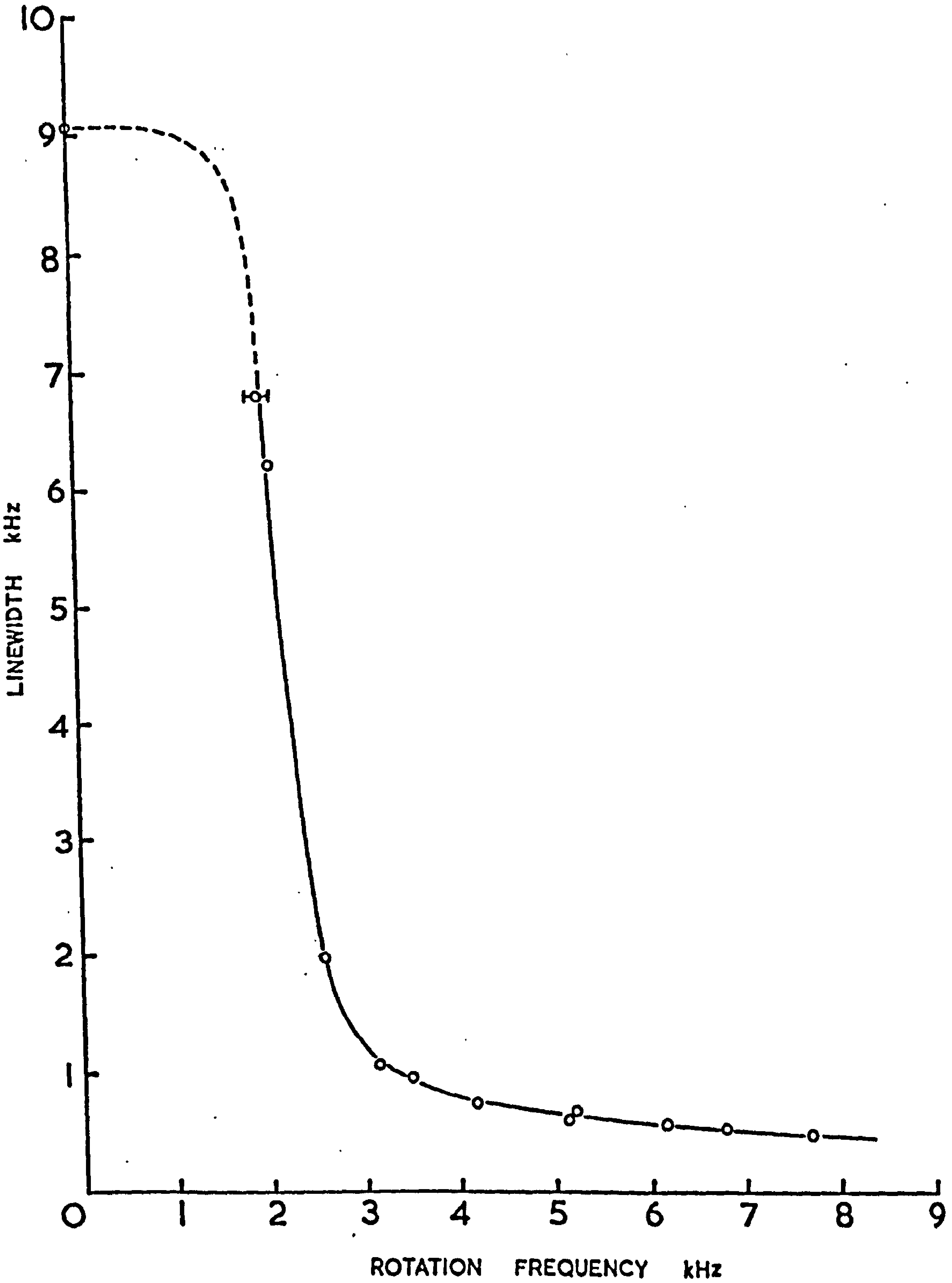

FIGURE 7.3. : The variation in the N.M.R. linewidth (measured between points of half intensity) of pure annealed aluminium powder against rotation frequency about the magic axis

even though it appears to be completely resolved from the first rotation beat. At this speed the linewidth is decreased by a factor of 20 over the static value. This is to be compared with the simple order of magnitude decrease recorded by Kessemeier and Norberg for a much smaller sample over the same range of spinning frequencies. The discrepancy probably largely reflects the different specifications of the samples used. The specimens employed in the measurements reported here were of annealed pure powder prepared by the metal spraying technique. Kessemeier and Norberg's samples were of unspecified purity and were subject to first order quadrupole interactions.

7.5 DETERMINATION OF RELAXATION TIMES

7.5.1 SPIN-LATTICE RELAXATION TIME (T_{1Z})

The powder samples used in these measurements were each sieved so that the grain size was less than 44 μm.

The spin-lattice relaxation time of powder (a) was measured as a function of rotation speed for speeds up to 4.5 kHz. For an applied magnetic field of 1.35 T and a room temperature of 295 K the measured T_{1Z} of the aluminium sample in a conical rotor spinning at the magic angle was 6.1 ± 0.2 ms, independent of rotation rate. This value is in agreement with the expression $T_1T = 1.85 \pm 0.05$ ms K as determined by Spokas and Slichter(104). Since the relaxation mechanism is via the electron-nucleus scalar contact interaction, the invariance of the relaxation time with rotation speed is to be expected.

The static spin-lattice relaxation times of samples (a), (b) and (c) were all determined using the 180-τ-90 pulse sequence. The results obtained at a temperature of 301 K in an applied field of 1.45 T are listed in Table 7.2. The errors quoted refer only to the spread of values in each case and not to any possible instrumental error or error in processing the data. The measurements were recorded within a short space of time of each other and an accurate comparison of the T_{1Z} values could be made. Although the error limits rule out any definite conclusion, the values quoted would seem to indicate that the pure filed powder (c) had a slightly shorter T_{1Z} than that prepared by spraying pure wire. The shortest T_{1Z} values occurred for the sample (b) considered to be the least pure of the three.

TABLE 7.2. EXPERIMENTAL ZEEMAN AND DIPOLAR RELAXATION TIMES

POWDER SAMPLE	T_{1Z} ms	T_{1D} ms	δ
99.995% pure sprayed (a)	6.12 ± 0.04	2.96 ± 0.05	2.07 ± 0.05
99.999% pure filed (c)	6.09 ± 0.04	2.88 ± 0.06	2.12 ± 0.06
99.5% pure sprayed (b)	6.04 ± 0.03	2.70 ± 0.05	2.24 ± 0.05

7.5.2 DIPOLAR RELAXATION TIME (T_{1D})

The dipolar relaxation times of samples (a), (b) and (c) were measured with the Jeener and Brockaert pulse sequence (see Section 5.8) in identical conditions to those existing for the T_{1Z} measurements. The results are included in Table 7.2 together with the corresponding values of δ (T_{1Z}/T_{1D}). The errors quoted again refer to the distribution of values obtained in each case.

Using the same technique Tunstall and Brown(72) measured T_{1D} and δ in samples of pure filed annealed powder over the temperature range 1.3-295 K. Although their measured δ value at room temperature was 2.25 they interpreted the recorded temperature dependence as indicating a contribution due to a quadrupolar thermal reservoir and concluded that the value of δ relating the true dipolar relaxation time to T_{1Z} was in fact 2.15 ± 0.07. From room temperature measurements of the spin-lattice relaxation in the rotating frame ($T_{1\rho}$) Fradin and Rowland(113) measured δ as 2.65. Pifer(114) used a CW slow passage saturation method and obtained a value of 2.07 ± 0.02 at 273 K. At liquid helium temperatures experimental values of δ have been consistently greater than 2.5(18,72,115).

The measurements reported here indicate that the method of sample preparation contributes to the measured values of T_{1D} and hence δ. The recorded δ value for the filed powder (c) is somewhat lower than Tunstall and Brown's uncorrected value from a similar sample at 295 K. On the other hand the value for powder (a) agrees with their corrected value to within experimental error and is in excellent agreement with that reported by Pifer. Such an occurrence may well be fortuitous, however, because no details of Pifer's samples are included. With the simplifying assumption of a spherical Fermi surface the theoretical value for δ is 2.06(72). The experimental value for the pure sprayed powder therefore fits present theory very well. It remains to be seen whether this value is independent of temperature as theory predicts.

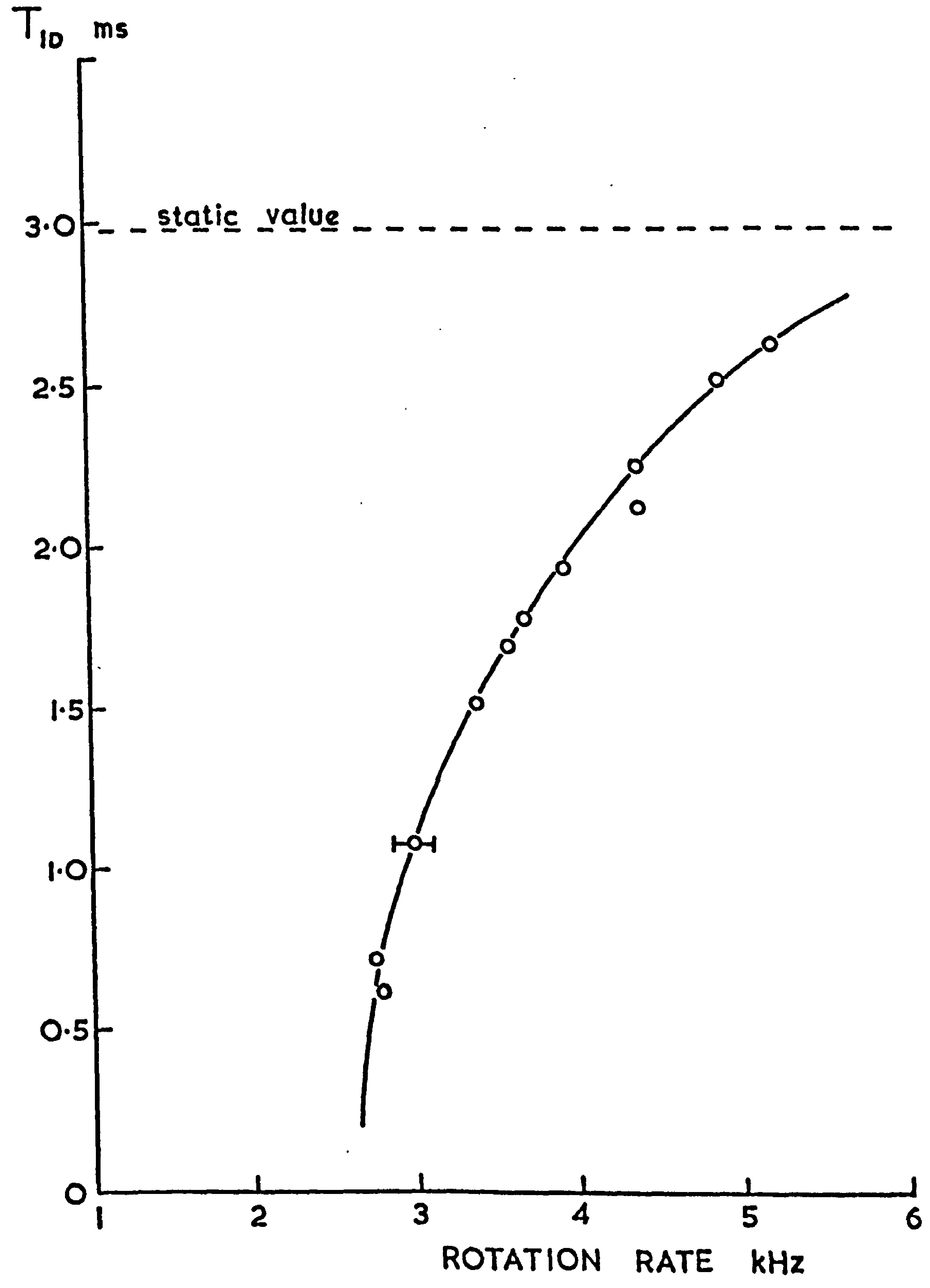

FIGURE 7.4 : The variation of 'T_{1D}' with rotation rate about an axis inclined at 90° to H_0

7.5.3 VARIATION IN 'T_{1D}' WITH ROTATION SPEED

As an interesting exercise the dipolar relaxation time of the sprayed pure powder (a) was measured as a function of rotation speed. It was found that with the rotors spinning about the magic axis, the modulation beats generated on the decay shapes distorted the signal amplitude detected after the third pulse of the Jeener and Brockaert sequence. However, by using the foil bearing rotor system it proved possible to spin the samples about an axis perpendicular to the external magnetic field. With this alignment of the rotors the detected decay signals remained relatively undistorted and results could then be obtained from the Jeener and Brockaert pulse sequence. As has been stated previously, use of the foil bearing system meant that the aluminium sample was at a somewhat higher temperature than the room, probably in the range 315-330 K.

The recorded variation in T_{1D} against spinning rate is shown in Figure 7.4. Rotation rates below 1.5 kHz could not be achieved with the foil bearing rotor system. However, it was found that in the range 1.5-2.7 kHz the relaxation times were too short to measure with the techniques employed anyway. Because of the need to keep the rotors spinning for quite a long period of time during each determination of T_{1D}, measurements were limited to a maximum spinning frequency of about 5 kHz. Compressed air could then be used as the driving gas. No detailed theoretical consideration of the form of the results has yet been undertaken.

CHAPTER 8

MEASUREMENTS ON VANADIUM, NIOBIUM AND CADMIUM METALS

8.1 INTRODUCTION

In practice the number of metals which can usefully be investigated using the magic angle rotation technique is limited. Although the more common metals all possess at least one isotope with a nuclear magnetic moment, the natural abundance of many of these is extremely low. This fact combined with low values of magnetic moment means that the resonances of a number of isotopes are extremely weak. Such isotopes are unsuited to the macroscopic rotation technique using existing equipment: indeed for many isotopes the resonance condition lay outside the range of the spectrometer. For those nuclear isotopes with spin greater than ½ existing in non-cubic lattices, quadrupole interactions lead to very broad characteristic spectra. Of those metals with cubic or near cubic lattice symmetry scandium, β-manganese, tantalum and thallium still have too large a static linewidth to be narrowed completely by the rotation rates which can be achieved at present. In the other extreme, at room temperature the secular line broadening interactions in the alkali metals are already reduced by diffusional motion. The room temperature linewidths of lead and platinum arise in large part from T_1 broadening, which is unaffected by macroscopic specimen rotation. Consequently these two metals were also excluded from the list of possible samples.

Although most metals of the lanthanide series possess at least one isotope with a magnetic moment, relatively little work has been done on the NMR spectra of the rare earth metals. This is presumably due in part to the difficulty in obtaining specimens of a sufficiently high purity. Nevertheless it is worth noting that considerations such as those described above rule out all but europium, ytterbium and perhaps lanthanum as specimens which might profitably be subjected to the magic angle rotation technique. With these metals, however, there is also the additional complication that they are readily oxidized and hence have to be kept from contact with the air.

With the experimental system available the list of metals, apart from the rare earths, which could usefully be investigated by rotation at the magic angle was found to be reduced to six: copper, tin, aluminium, cadmium, vanadium and niobium. Investigations have already been carried out on the effect of specimen rotation on the NMR spectra of copper(59) and β-tin(116). Hence, since the work on aluminium has been described in the preceding chapter, detailed in this chapter are a series of measurements on powdered specimens of vanadium, niobium and cadmium. Although samples of all three metals were spun at speeds up to 5 kHz, the static linewidths of vanadium and niobium were found to be too large to be affected by spinning rates of this magnitude.

8.2 VANADIUM

Vanadium powder with a stated purity of 99.5% and a particle size of less than 75 μm was obtained commerically from Koch-Light Laboratories. Because of the difficult nature of the annealing process for vanadium the measurements were all undertaken on unannealed specimens. The loose powder samples used in some measurements were suspended in a light oil. This served to damp out mechanical vibrations induced in the individual crystallites by the rf pulse which otherwise distorted the detected decay signals. Other measurements were performed on solid slugs consisting of the metal powder suspended in a resin matrix, the manufacture of which was described in Section 5.9.

The spin-lattice relaxation time of ^{51}V was measured in these samples. The value of T_1 obtained at a room temperature of 295 K and a resonance frequency of 15 MHz was 2.7 ± 0.1 ms. This value is in good agreement with that computed from the expression $TT_1 = 0.788$ as determined by Butterworth(117).

A typical FID recorded with the signal averager from a powder sample is shown in Figure 8.1, together with the corresponding computed spectrum in the frequency domain. (The time resolution of the measured decay envelope was set by the maximum sweep speed of the signal averager.) The two lineshapes drawn relate to two different assumptions about the form of the FID during the 12 μs dead time. An exponential fit to the first few detected data points is shown by the full line and the dashed line represents a Gaussian approximation. It is suspected that the exponential fit is closer to the true situation. Quadrupole echoes(118,119) were observed following pairs of closely spaced pulses, indicating that the absorption lineshapes were broadened by first order quadrupole interactions. This finding is consistent with the Lorentzian type wings of the frequency spectrum defined by the solid line in Figure 8.1.

The large linewidth of the resonance spectrum prevented the macroscopic rotation technique used for aluminium from being applied

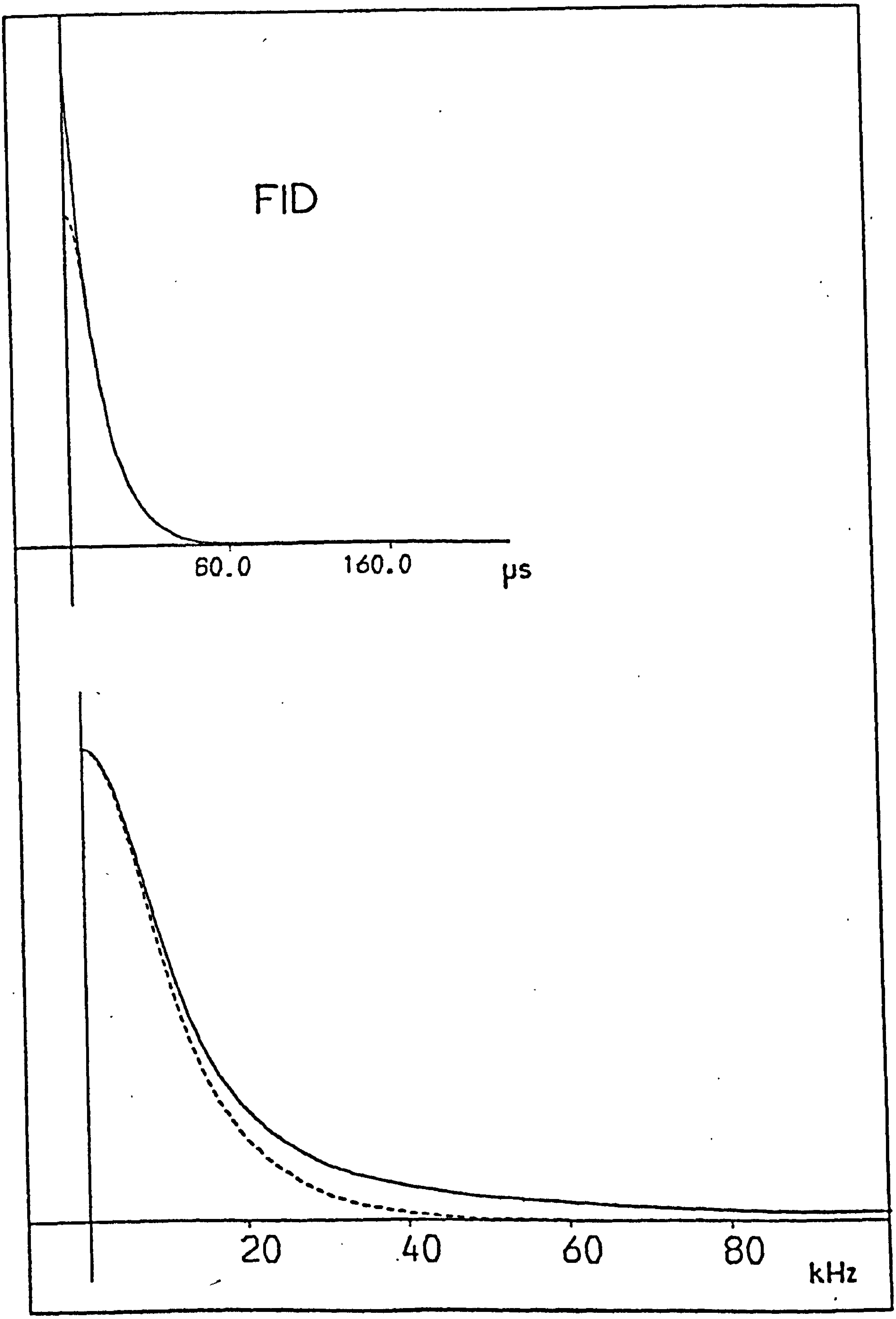

FIGURE 8.1 : The ^{51}V F.I.D. and fourier transformed spectrum. The two lines relate to two different assumptions about the shape of the F.I.D. during the instrumental dead time.

in the same way to the precise determination of the ^{51}V Knight shift. The detected FIDs (and hence the absorption spectra) of the vanadium sample slugs were found to be largely unaffected by magic angle rotation at speeds up to 4.5 kHz. However an estimate of the Knight shift was made by exchanging the metal and reference sample in the regular Bruker probe. In the frequency domain the resonance frequency is defined quite accurately by the Lorentzian type centre of the absorption lineshape. This accuracy was similarly apparent in the time domain where the large signal intensity and short T_1 enabled the null position to be set to ±60 Hz.

There is no obvious reference compound that should be used in the measurement of the ^{51}V Knight shift. In the past, values have been quoted with respect to $Nb(VO_3)_2$ (120), KVO_3 (121), $VOCl_3$ (122) and $NaVO_3$ (123) and vanadium dissolved in nitric acid(124). $VOCl_3$ was ruled out as a possible reference compound, because chemical shift measurements have shown that the ^{51}V resonance in $VOCl_3$ is shifted paramagnetically compared to most other observable vanadium compounds(125). For this work sodium metavanadate was chosen in preference to potassium metavanadate and lead metavanadate because of its greater solubility in water. Thus the Knight shift of the powdered metal was measured against a saturated solution of $NaVO_3$ in distilled water. The value obtained at a room temperature of 298 K was 5755 ± 5 ppm, where the error refers to the uncertainty in setting the null position of the metal and reference solution. This result is to be compared with the value of 5805 ± 10 ppm recorded by Drain(123) at a similar temperature. Vanadium has a large magnetic susceptibility so the discrepancy between these two figures may arise partly from a bulk susceptibility correction due to the geometry of the samples used in each case. However a calculation similar to that performed for aluminium in Section 7.2.3(c) puts the possible contribution to the experimental Knight shift measured here of no more than 5 ppm. Certainly there was no measurable difference in the resonance frequencies of ^{51}V in the loose powder specimens and the solid araldite slugs.

8.3 NIOBIUM

99.9% pure niobium powder with a particle size of less than 40 μm was obtained from Metals Research Limited. The static measurements were recorded on specimens of the loosely packed unannealed powder at room temperature using a resonant frequency of 15 MHz.

The spin-lattice relaxation time was measured using a 90-τ-90 pulse sequence, but the recovery envelope was not found to obey a simple exponential relationship. A large proportion of the magnetization recovered in a few microseconds, but a slow component had a time constant of about 1.1 ms. This form of recovery indicates that there was a significant second-order quadrupole broadening present in the powder specimens, a result which is in agreement with that recorded by Butterworth(128) in similar powdered metal samples.

The FIDs recorded from these samples were found to be almost exponential with a time constant of 11.5 ± 1.5 μs. This value is considerably shorter than that found by Butterworth from a pure foil sample, but is consistent with his measured T_2 values from powdered specimens and the large variation in linewidths reported elsewhere(127). The width of the Lorentzian lineshape defined by the exponential decay of the transverse magnetization is given by

$$\Delta\nu = \frac{1}{\pi T_2} \simeq 28 \text{ kHz}$$

which is slightly larger than the width of the vanadium resonance line. That the origin of this large linewidth was mainly quadrupolar in origin was made evident by the large quadrupolar echoes observed following for example a 90-τ-35 pulse sequence(118,119). As expected, rapid sample rotation about the magic angle at speeds of around 5 kHz failed to have any effect upon the nuclear lineshape.

There are very few compounds of niobium which can be observed by NMR. The niobium Knight shift has been measured previously with respect to Nb_2O_5 dissolved in hydrofluoric acid. However in our work the Knight shift was determined against a solution of $NbCl_5$ in pure acetone. The solution is light yellow upon the $NbCl_5$ first being introduced, but later turns brown and produces a brown precipitate. Although the ^{93}Nb resonance observed during this time varies considerably both in frequency and in T_2, after several hours it becomes constant. The Knight shift value obtained by direct substitution of the reference and metal samples into the Bruker coil was 0.768 ± 0.008%. Values quoted in the literature with respect to Nb_2O_5 in HF are 0.85(120) and 0.875%(127). In view of the unknown nature of the reference compounds, the discrepancy is not meaningful.

The large experimental Knight shifts measured for both vanadium and niobium have been explained in terms of a large orbital contribution to the hyperfine coupling in these two metals(128).

8.4 CADMIUM

8.4.1 INTRODUCTION TO THE MEASUREMENTS

Cadmium has two magnetic isotopes ^{111}Cd and ^{113}Cd which have natural abundances of 12.86% and 12.34% respectively. Both isotopes have spin ½ so,although cadmium metal has a hexagonal crystal structure, the nuclear resonance spectra are unaffected by electric field gradients caused by the deviation from cubic symmetry. At high magnetic fields the main source of broadening in powdered specimens arises from the anisotropic Knight shift interaction due to the non-s-character of the conduction electrons. Because of the asymmetry of the nuclear lineshapes, there exists some uncertainty in defining the exact centre frequency and hence the isotropic Knight shift. Rapid sample rotation about the magic axis removes this anisotropy and narrows the lineshape, thus enabling the centre frequency to be determined accurately. Under the condition of a sufficiently rapid rotation rate the residual central spectrum is determined by the isotropic part of the indirect exchange interaction between nuclear spins and by lifetime broadening. Typical spectra of static and rotated cadmium powder are shown in Figure 8.2.

The NMR sensitivity of both the ^{111}Cd and ^{113}Cd resonances in cadmium metal is less than a thousandth of that of aluminium. Although the anisotropic broadening of the nuclear lineshapes is greater at higher magnetic fields, the signal to noise ratio of the detected signals is significantly improved by the use of higher rf frequencies. Consequently measurements were undertaken employing as high an applied magnetic field as could reasonably be achieved with the M12 electromagnet. The powdered metal samples used in this work were obtained from Cerac Inc. (USA). The stated purity was 99.999% and the particle size was less than 40 μm, as compared to the value of the skin depth at 13 MHz of 30 μm.

8.4.2 KNIGHT SHIFT DETERMINATIONS

Previous room temperature estimates of the isotropic Knight shift of cadmium metal as performed against aqueous solutions of cadmium chloride and cadmium nitrate have yielded values in the range 0.39-0.43%(120,129-134). Recently however it has been shown(135) that there exists a considerable range of chemical shifts between the cadmium resonances from different aqueous solutions of cadmium salts. These chemical shifts vary not only between the different salts but also between different concentrations of the same salt. The measured Knight shift depends therefore upon the particular reference sample chosen.

The Knight shift of both isotopes was measured here using the double rotor box described in Section 5.4. Rotors containing the solid powder slugs were spun at speeds up to 4.5 kHz in a magnetic field of 1.45 T. By employing the DL 102 signal averager the reference frequency and phase of the PSD could be adjusted so as to measure the resonance frequency of the metal to an accuracy of ±20 Hz. Preliminary measurements were performed against saturated solutions of $CdCl_2$. The signal strengths were extremely poor so in order to shorten the spin-lattice relaxation time the salt was dissolved in a 1% molar aqueous solution of $MnCl_2$. Against this reference and at a temperature of 300 K the Knight shifts for ^{111}Cd and ^{113}Cd were measured as 4155 ± 4 ppm and 4154 ± 4 ppm. The errors quoted arise largely from the uncertainty in defining the centre frequency of the very weak signals from the reference solution. The resonance frequencies of the $CdCl_2$ solutions were found to vary considerably with the amount of paramagnetic doping. For example, compared to a saturated solution of $CdCl_2$ in 0.2% molar $MnCl_2$ the chemical shift of the reference solution used in the above measurements was about +15 ppm. Nevertheless the values quoted above illustrate that any isotopic dependence of the Knight shift is less than 2×10^{-3}.

A second set of measurements were made against diluted undoped solutions of $Cd(NO_3)_2$. The signal intensity was again poor, but, by pulsing rapidly and transforming the transient signal to the frequency domain, the resonance frequency could be assessed quite accurately. Choosing a solution concentration for which the chemical shift is known should in principle enable the measured Knight shift to be related to the cadmium ion in a vanishingly small dilution of the salt, i.e. to a single ion in water. Against a concentration of solution corresponding to 0.06 moles of Cd in 1 mole of water the measured Knight shifts at a temperature of 285 ± 2 K were 4321 ± 6 ppm and 4324 ± 8 ppm for ^{111}Cd and ^{113}Cd respectively. By employing the experimentally determined value for the fractional change in Knight shift with pressure(136), a calculation of the rotationally induced stresses in the metal gives a maximum possible contribution to the Knight shift of 2 ppm, well within the experimental error. The effect of the sample bulk susceptibility is negligible in comparison. The results of Kruger et al.(135) indicate that a correction factor of -46 ppm could normally be applied to relate the Knight shift values recorded above to the free ion in solution. However, this value of the chemical shift was measured at a temperature of 306 K, so the magnitude of this correction may well be inaccurate at the somewhat lower temperature of our measurements.

8.4.3 SPIN-LATTICE RELAXATION TIMES

The spin-lattice relaxation times of ^{111}Cd and ^{113}Cd were measured in the spinning and static samples. The results of 1.65 ± 0.15 ms for ^{111}Cd and 1.40 ± 0.10 ms for ^{113}Cd at a room temperature of 298 K were independent of rotation rate as expected. The measured T_1 for ^{113}Cd is considerably higher than Masuda's reported room temperature value of 0.5 ms(137), but it is in better agreement with the figure of approximately 1.2 ms recorded by Dickson(138). No measurements of the ^{111}Cd T_1 have apparently been reported in the literature. However the relaxation time measured here is consistent with the lower gyromagnetic ratio of this isotope.

It is of interest to compare the product T_1K^2T found by experiment with the theoretical value derived from the Korringa relation given by equation (2.23). In cadmium the direct contact mechanism arising from the s-type conduction electrons is assumed to dominate the Knight shift and the spin-lattice interactions. In this event the scalar R defined thus

$$RT_1K^2T = \frac{\hbar}{4\pi k_B}\left(\frac{\gamma_e}{\gamma_n}\right)^2$$

is a measure of electron enhancement of both K and $1/T_1$. At room temperature the results of Seymour and Styles(133) indicate that the experimental Knight shift increases by about 4 ppm/°K. The temperature correction acts in the opposite direction to the chemical shift correction, so it is not unreasonable to take the Knight shift of cadmium at 298 K as 0.43% to a first approximation. Substituting our experimental values for the ^{111}Cd and ^{113}Cd relaxation times at this temperature we obtain a mean value for R of 0.65. This figure is somewhat lower than the value of 0.85 recorded for the solid state by Dickson. The discrepancy arises out of the higher values of T_1 and K used in our calculation.

We note that Kruger et al. demonstrated that there is quite considerable shielding of the cadmium ions in aqueous solutions. Therefore any determination of the absolute value of R is dependent upon the experimental Knight shift being corrected for such shielding effects in both the metal and the salt.

8.4.4 VARIATION OF LINESHAPE WITH ROTATION SPEED

Careful lineshapes of the resonances of ^{111}Cd and ^{113}Cd nuclei were measured from static samples using the same resonant frequency of 13.7 MHz for both isotopes. The anisotropic Knight shift can be estimated by comparing the experimental lineshape to the theoretical frequency distribution

$$g(\nu) = K[2(\nu - \nu_o) + \alpha]^{-\frac{1}{2}}$$

given by equation (2.11). Figure 8.3 shows the ^{113}Cd absorption curve together with the theoretical powder lineshape predicted by g(ν) setting α equal to 4.4 kHz. The ^{111}Cd absorption spectrum was the same as the ^{113}Cd spectrum to within experimental error and hence gave an identical value for α. It is usual to define the anisotropic Knight shift, K_{an} as

$$K_{an} = \frac{3\alpha}{2\nu_o} \qquad (\alpha \text{ measured in frequency units}) \quad .$$

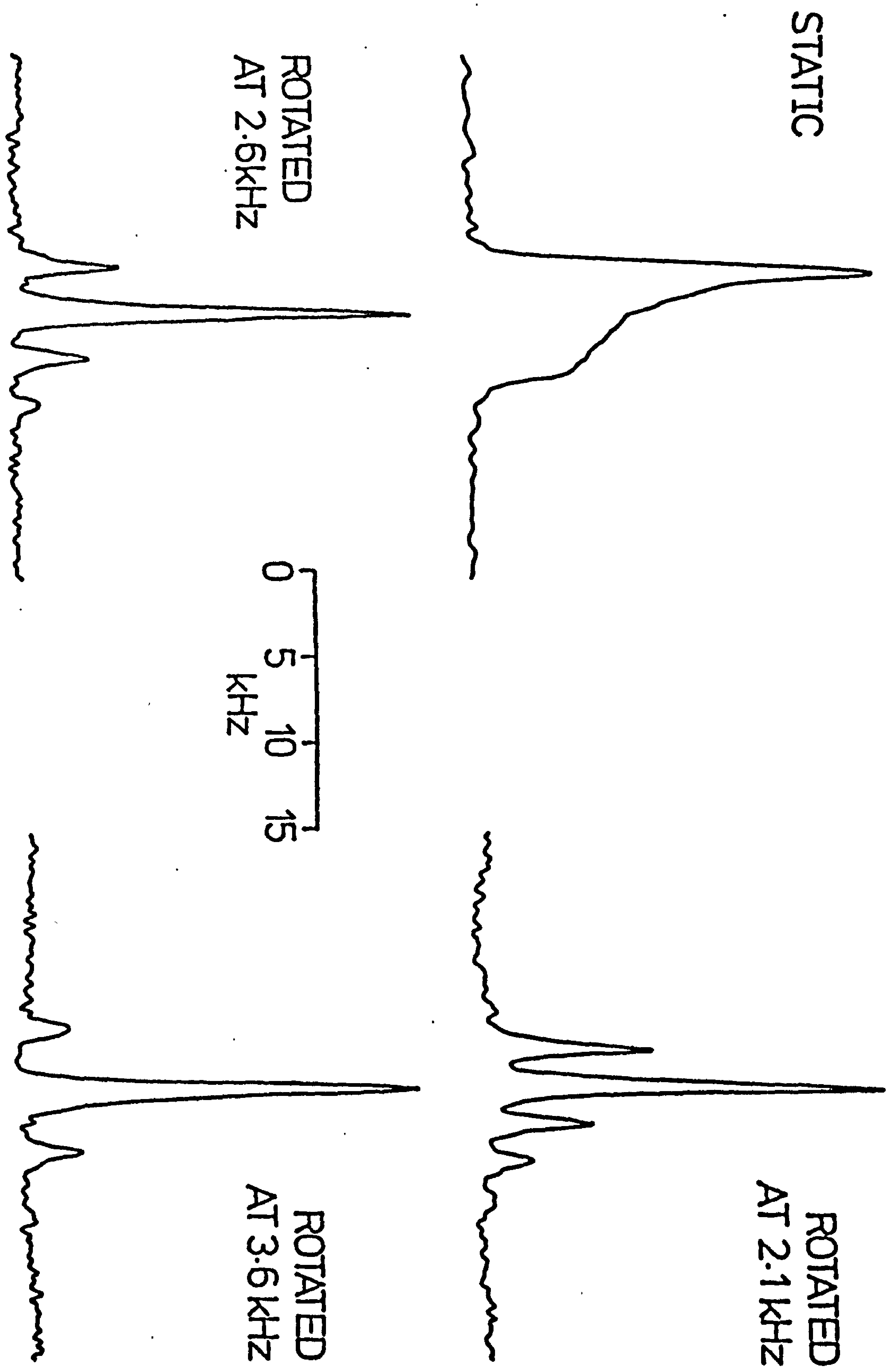

FIGURE 8.2 : The ^{111}Cd fourier transformed spectra of pure cadmium powder, static and rotated at three different frequencies about the magic axis

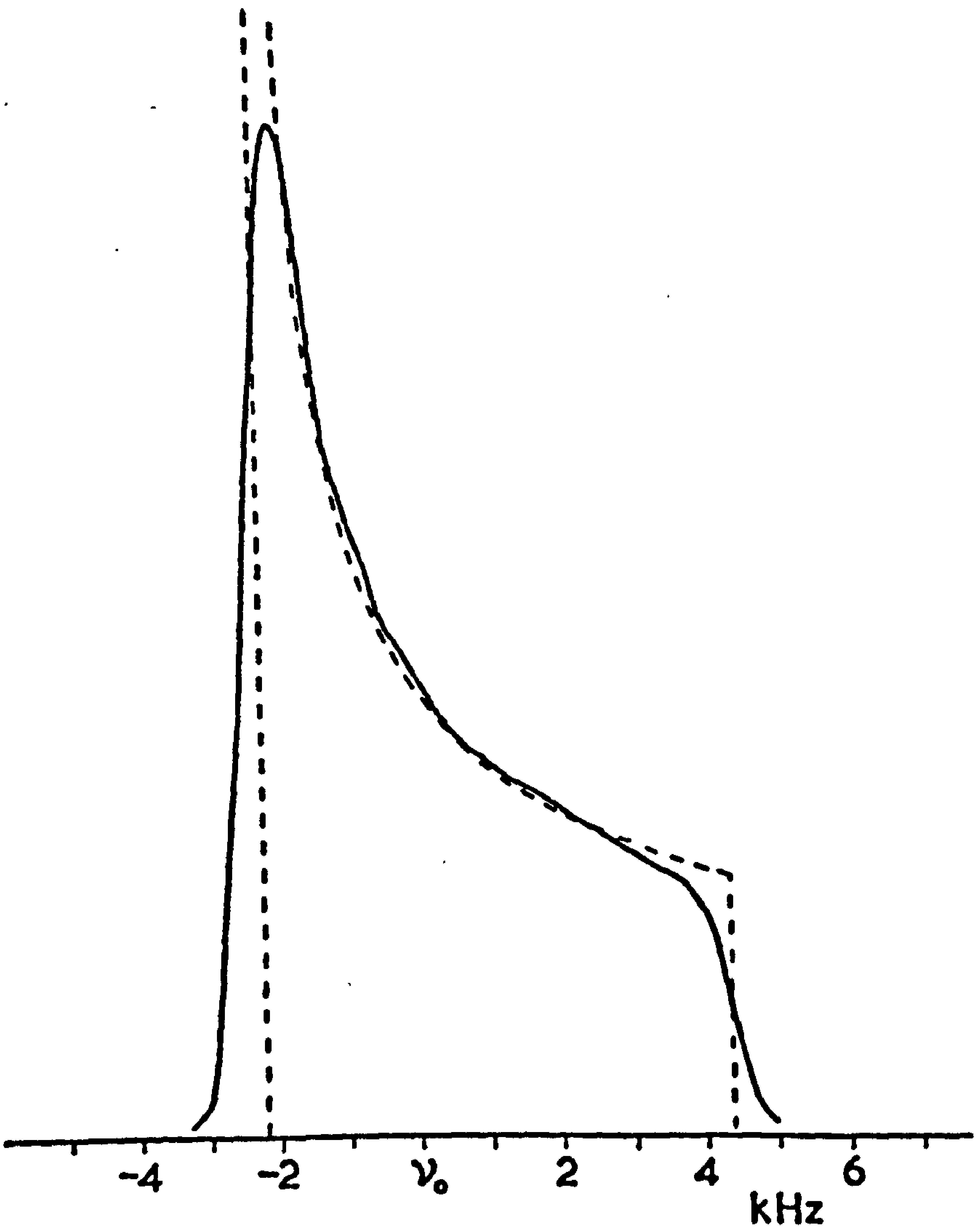

FIGURE 8.3 : The ^{113}Cd static powder spectrum. The form of lineshape predicted by the anisotropic Knight shift interaction alone is shown as the broken line.

which gives

$$K_{an} = 0.048 \pm 0.002 \ .$$

Although somewhat larger than the estimate by Masuda(130), this figure is in good agreement with the results of Rowland(129) and of Borsa and Barnes(132) who determined K_{an} from a measurement of linewidth against magnetic field.

Figure 8.2 shows the ^{111}Cd resonance spectrum measured with the powder specimen spinning about the magic angle at three different rates. The conical rotor system was employed in an applied magnetic field of 1.45 T. Accurate adjustment of the magic angle was performed by observation of the strong resonance signal from a small amount of aluminium powder mixed with the cadmium. It can be seen that the anisotropic Knight shift broadening of the resonance spectrum is indeed removed by rotation at the magic angle. As the rotation rate is increased the spinning sidebands, which are asymmetric about ν_o, become completely removed from the central spectrum leaving a residual symmetric line. The signal-to-noise ratio of the transformed lineshapes was not sufficient to enable the second moments of the central lines to be estimated with any degree of certainty. However the half-height linewidths could be determined. Although there was considerable scatter in the results obtained at differing rotation frequencies, the width of the ^{113}Cd resonance line was consistently greater than that of the ^{111}Cd. The mean values of their residual linewidths were 800 ± 100 Hz and 750 ± 80 Hz respectively. The large spread in values is assumed to arise because of the relatively poor signal strengths and the ad hoc assumptions made about the data points obscured during the instrumental dead time.

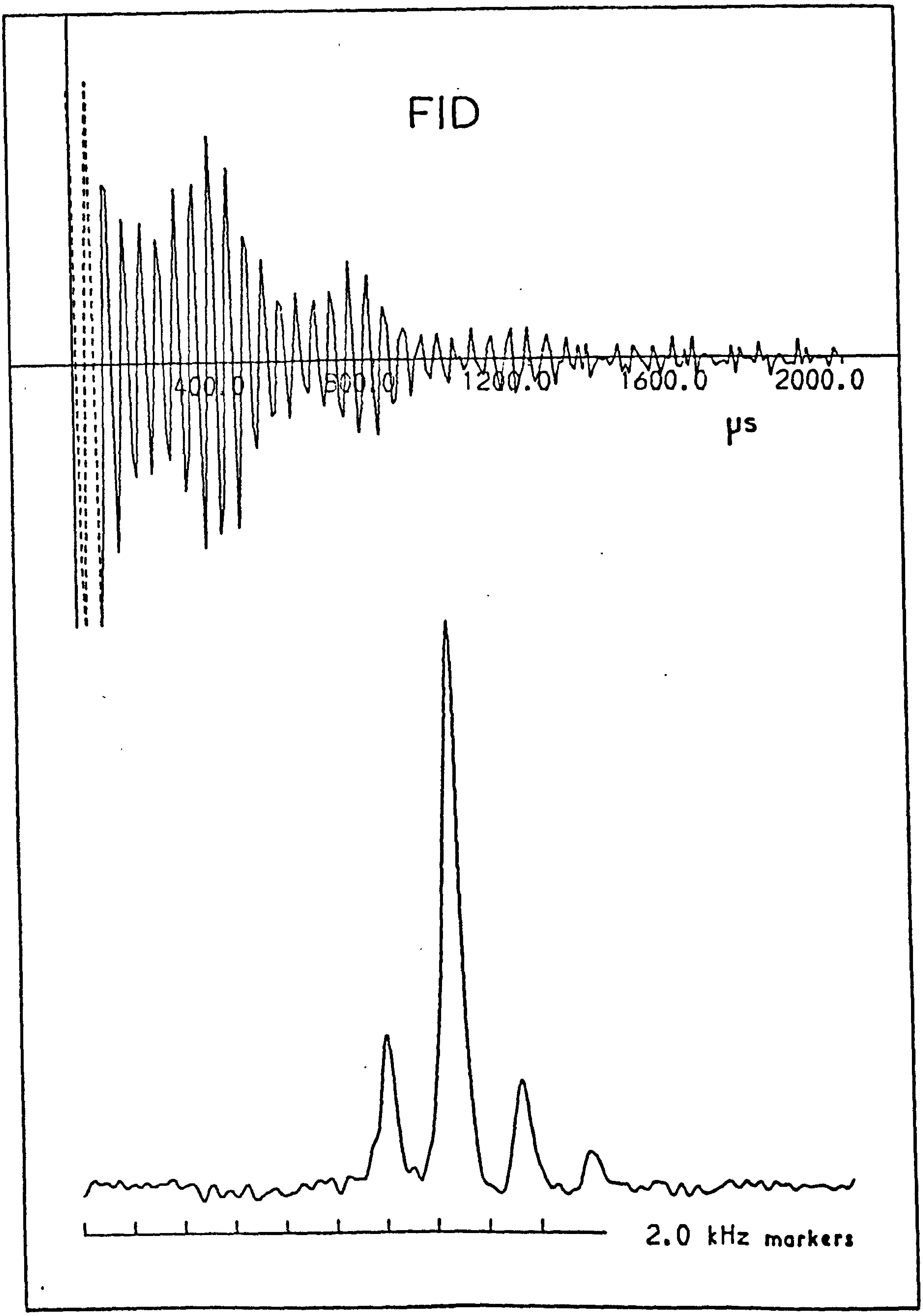

FIGURE 8.4 : The ^{111}Cd F.I.D. and fourier transformed spectrum with the specimen rotated about the magic axis at 2.6 kHz. The dashed lines indicate the form of the F.I.D. assumed during the instrumental dead time

Lifetime broadening alone gives rise to a Lorentzian lineshape in the frequency domain with a width at half-height of $1/\pi T_1$. Assuming that the lifetime contribution to the total width of the residual spectrum can be separated by a simple subtraction, then upon substituting the values for T_1 recorded previously the secular broadening of the central line becomes about 560 Hz for both isotopes. The above value includes a contribution from the inhomogeneity of the magnetic field but this was estimated to be negigible (< 20 Hz) in comparison. Consequently the figure quoted represents a measure of the electron coupled scalar interaction between the cadmium nuclei. The equivalence of the linewidth for the two isotopes simply reflects their almost equal natural abundancies.

At room temperature the relaxation times of both isotopes are of approximately the same magnitude as the inverse of the first and second nearest neighbour exchange coupled constants as determined by Alloul and Deltour(139). This leads to the possibility that the isotropic magnetic exchange interaction may be time averaged by lifetime fluctuations in the nuclear spin states. Any detailed calculation of the Rudermann-Kittel(14) indirect exchange interaction is precluded by an incomplete knowledge of the effect of these fluctuations as well as by the preliminary nature of the results. Consequently we content ourselves with making a simple comparison of our results to those obtained by Alloul and Deltour from observation of the modulated structure of the spin echoes of the ^{113}Cd resonance in cadmium based alloys. Their experiment was undertaken at liquid helium temperatures, in which region T_1 contributions to the lineshapes are negligible. The exchange coupling constants, J_1 and J_2, between the first and second nearest neighbours in the hexagonal close packed crystal lattice were calculated using the expression for the second moment

$$M_2 = 0.95B_1^2 + 0.218J_1^2 + 0.192J_2^2$$

where B_1 represents the total dipolar coupling between first nearest neighbours (including pseudo-dipolar coupling). Rotation at the magic angle removes the dipolar and pseudo-dipolar contributions to the central spectrum. The second moment of the residual line is then given by

$$M_2' = 0.218J_1^2 + 0.192J_2^2 \quad .$$

The width of a Gaussian lineshape is often approximated to $2\sqrt{M_2}$. Applying a similar approximation here and substituting Alloul and Deltour's values for J_1 and J_2 of -510 Hz and -380 Hz respectively into the above expression, we obtain a theoretical linewidth of 580 Hz. The agrement with the T_1 corrected value for the experimental linewidth quoted previously is very satisfactory. In view of the assumptions made in the calculation, the precise agreement may be fortuitous. Nevertheless, it does serve to demonstrate that any lifetime averaging effect on the scalar interaction at room temperature is probably small.

In conclusion we emphasize the preliminary nature of our measurements. The experimental accuracy could be improved by averaging the detected decay signals over a longer period of time and by employing a more reliable procedure for fitting the dead time data points. However, as the rotors at present available cannot be spun at low temperatures, any determination of the scalar coupling constants in cadmium is dependent upon a detailed consideration of the effect of the short spin-lattice relaxation time on this interaction.

REFERENCES

General References for Chapters 1 and 2.

C. P. Slichter, Principles of Magnetic Resonance (1963) Harper and Row, New York.

A. Abragam, The Principles of Nuclear Magnetism (1961), Clarendon Press, Oxford.

J. Winter, Magnetic Resonance in Metals (1971) Clarendon Press, Oxford.

Review Articles on NMR in Metals

T. J. Rowland, Progress in Materials Science (1961) 9 1.

L. E. Drain, Metallurgical Reviews (1967) 12 195.

1. F. Bloch, Phys. Rev. (1946) 70 460.
2. See for example, P. Mansfield, M. J. Orchard, D. C. Stalker, K. H. B. Richards, Phys. Rev. B (1972) 7 90.
3. M. H. Cohen, F. Reif, in Solid State Physics, Vol. 5, p.321-428, Academic Press, New York (1957).
4. G. D. Watkins, R. V. Pound, Phys. Rev. (1953) 89 658.
5. A. J. Freeman, R. E. Watson, 'Hyperfine interactions in magnetic materials' in Magnetism, Vol. IIA, Ed. G. T. Rado and H. Suhl, Academic Press, New York (1965).
6. M. H. Cohen, D. A. Goodings, V. Heine, Proc. Phys. Soc., A73 811 (1959).
7. R. V. Heine, Phys. Rev. (1957) 107 1002.
8. A. M. Clogston, V. Jaccarino, Y. Yafet, Phys. Rev. (1964) 134 A650.
9. J. A. Seitchik, A. C. Gossard, V. Jaccarino, Phys. Rev. (1964) 136A 1119.
10. R. Kubo, Y. Obata, J. Phys. Soc. Japan (1956) 11 153.

11. L. E. Orgel, J. Phys. Chem. Solids (1961) 21 123.

12. N. F. Ramsey, E. M. Purcell, Phys. Rev. (1952) 85 143.

13. N. Bloembergen, T. J. Rowland, Phys. Rev. (1955) 97 1679.

14. M. A. Ruderman, C. Kittel, Phys. Rev. (1954) 96 99.

15. S. Gade, Phys. Rev. (1969) 187 419.

16. J. H. Van Vleck, Phys. Rev. (1948) 74 1168.

17. J. Korringa, Physica (1950) 16 601.

18. A. G. Anderson, A. G. Redfield, Phys. Rev. (1959) 116 583.

19. P. A. Wolff, Phys. Rev. (1963) 129 84.

20. G. R. Khutsishvili, Soviet Phys. JETP (1957) 4 382.

21. J. Van Kranendonk, M. B. Walker, Phys. Rev. Letters (1967) 18 701.
and Can. J. Phys. (1968) 46 2441.

22. J. Van Kranendonk, Physica (1954) 20 781.

23. R. L. Mieher, Phys. Rev. (1962) 125 1537..

24. R. M. Sternheimer, Phys. Rev. (1954) 95 736.
H. M. Foley, R. M. Sternheimer, D. Tycko , Phys. Rev. (1954) 93 734.

25. E. G. Wikner, T. P. Das , Phys. Rev. (1958) 109 360.

26. K. Yosida, T. Moriya, J. Phys. Soc. Japan (1956) 11 33.

27. J. Kondo, J. Yamashita, J. Phys. Chem. Solids (1959) 10 245.

28. E. G. Wikner, W. E. Blumberg, E. L. Hahn, Phys. Rev. (1960) 118 631.

29. M. J. Weber, Phys. Rev. (1963) 130 1.

30. S. K. Joshi, R. Gupta, T. P. Das , Phys. Rev. A (1964) 134 693.

31. F. Bridges, W. Gilbert Clark, Phys. Rev. (1967) 164 288.

32. C. E. Torr, L. M. Stacey, C. V. Briscoe, Phys. Rev. (1967) 155 272.

33. S. Clough, K. W. Gray, Proc. Phys. Soc. (1962) 79 457, 80 1382.

34. H. Kessemeier, R. E. Norberg, Phys. Rev. (1967) 155 321.

35. E. R. Andrew, A. Bradbury, R. G. Eades, V. T. Wynn, Phys. Letters (1963) 4 99.

36. E. R. Andrew, L. F. Farnell, Mol. Phys. (1968) 15 157.

37. E. R. Andrew in 'Progress in Nuclear Magnetic Resonance Spectrosdopy', Vol. 8, Part 1, Pergamon Press (1971).

38. E. R. Andrew, A. Jasinski, J. Phys. C: Solid State Phys. (1971) 4 391.

39. A. C. Cunningham, S. M. Day, Phys. Rev. (1966) 152 287.

40. G. E. Pake in 'Solid State Physics', Vol. 2,1 (1956).

41. E. R. Andrew, R. A. Newing, Proc. Phys. Soc. (1958) 72 959.

42. E. R. Andrew, G. J. Jenks, Proc. Phys. Soc. (1962) 80 663.

43. E. R. Andrew, A. Bradbury, R. G. Eades, Nature (1958) 182 1659, and 183 1802 (1959).

44. I. J. Lowe, Phys. Rev. Letters (1959) 2 285.

45. S. Clough, I. R. MacDonald, Proc. Phys. Soc. (1965) 86 833.

46. U. Haeberlen, J. S. Waugh, Phys. Rev. (1969) 185 420.

47. A review of such work is given in Reference 37.

48. Guinness Book of Records, Ed. R. and N. McWhirter (1973).

49. E. R. Andrew, L. F. Farnell, M. Firth, T. Gledhill, I. Roberts, J. Mag. Res. (1969) 1 27.

50. J. Babka, D. Doskocilova, H. Purcova, Z. Ruzicka, B. Schneider, Proc. XVI Ampere Congress (1970), Ed. I. Ursu, p.785, Romanian Publishing House, 1971.

51. S. Timoskenko,'Strength of Materials', Part 2, 216, Van Nostrand, New York (1956).

52. A detailed description of this effect is given in 'Gas Lubricated Bearings', Editors N. S. Grassan and J. W. Powell, Chapters 3 and 5, Butterworths, London (1964).

53. See for example H. W. Liepmann and A. Roshko, 'Elements of Gas Dynamics', Wiley and Son, New York (1967).

54. E. Heriot, E. Huguenard, Comptes Rendus (1925) 180 1389, and J. de Phys. et Rad. (1927) 8 443.

55. J. W. Beams, Rev. Sci. Instrum. (1930) 1 667.

56. J. W. Beams, E. G. Pickels, Rev. Sci. Instrum. (1935) 6 299.

57. T. D. Gledhill, Ph.D. Thesis, University of Nottingham (1967).

58. M. Firth, Ph. D. Thesis, University of Nottingham (1970).

59. P. J. Randall, Ph.D. Thesis, University of Nottingham (1972).

60. A more detailed description of the characteristics of a foil bearing rotor support is given by:

M. Wildmann, Paper 1, Gas Bearing Symposium, University of Southampton (1969).

61. R. W. Woolley, Paper 25, Gas Bearing Symposium, University of Southampton (1971).

And Private Report to the Department of Physics, University of Nottingham, unpublished.

62. Degussit, Technical Information.

63. S. Timoshenko, J. N. Goodier, 'Theory of Elasticity', p. 410, McGraw-Hill, New York (1951).

64. Advanced Materials Limited, Technical Information.

65. D. Doskocilova, B. Schneider, Chem. Phys. Letters (1970) 6 381.

66. B. Bleaney and B. I. Bleaney, 'Electricity and Magnetism', p. 171, Oxford University Press (1965).

67. E. R. Andrew, J. L. Carolan, P. J. Randall, Phys. Letters (1971) 35A, 435.

68. D. S. Banaal, I. J. Lowe, Phys. Rev. Letters (1963) 11 258.

69. J. Jeener, P. Brockaert, Phys. Rev. (1967) 157 232.

70. J. G. Powles, J. H. Strange, Proc. Phys. Soc. (1963) 82 6.

71. P. Mansfield, Phys. Rev. A (1965) 137 961.

72. D. P. Tunstall, D. Brown, Phys. Rev. B (1970) 1 2881.

73. A. F. Wells, 'Structural Inorganic Chemistry', Oxford University Press, London (1962).

74. A. C. Chapman, P. Rhodes, E. F. W. Seymour, Proc. Phys. Soc. B (1957) 70 345.

75. D. Kotzur, O. Kanert, M. Mehring, Proc. XVII Ampere Congress, Ed. V. Hovi, p. 322, North-Holland, Amsterdam (1973).

76. P. L. Sagalyn, J. A. Hofmann, Phys. Rev. (1962) 127 68.

77. E. R. Andrew, J. L. Carolan, P. J. Randall, Chem. Phys. Letters (1971) 11 298.

78. B. D. Guenther, R. Hultsch, J. Mag. Res. (1969) <u>1</u> 609.

79. K. D. Becker, G. W. Herzog, D. Kanne, H. Richtenig, E. Stadler, Z. Elecktrochem. (1970) <u>74</u> 527.

80. S. Domngang, J. Wucher, C. R. Acad. Sci. Paris (1969) <u>268</u> 1608.

81. S. Domngang, J. Wucher, J. F. Caillard, Proc. XV Ampere Congress, Ed. P. Averbuch, p. 399, North-Holland, Amsterdam (1969).

82. H. Kruger, U. Meyer-Berkhout, Z. Phys. (1952) <u>132</u> 171.

83. J. G. King, V. Jaccarino, Phys. Rev. (1954) <u>94</u> 1610.

84. B. Bleaney, K. D. Bowers, M. H. Pryce, Proc. Roy. Soc. (1955) <u>A228</u> 166.

85. R. M. Sternheimer, Phys. Rev. (1966) <u>146</u> 140.

86. G. Burns, E. G. Wikner, Phys. Rev. (1961) <u>121</u> 155.

87. Values taken from Chemical Rubber Handbook, 54th Edition, C.R.C. Press, Cleveland.

88. R. W. G. Wyckoff, 'Crystal Structures', <u>1</u> 110, Wiley, New York (1963).

89. W. Hinshaw, J. T. Lewis, C. V. Briscoe, Phys. Rev. (1967) <u>163</u> 878.

90. See values quoted by J. Van Kranendonk, M. B. Walker, Phys. Rev. Letters (1967) <u>18</u> 701 (Reference 22).

91. W. D. Knight, Phys. Rev. (1949) <u>76</u> 1259.

92. H. S. Gutowsky, B. R. McGarvey, J. Chem. Phys. (1952) <u>20</u> 1472.

93. F. Borsa, R. G. Barnes, J. Phys. Chem. Solids (1966) <u>27</u> 567.

94. A. Narath, A. T. Weaver, Phys. Rev. (1968) <u>175</u> 373.

95. U. El Hanany, D. Zamir, Solid State Comm. (1972) <u>10</u> 1223.

96. T. Kushida, J. C. Murphy, Phys. Rev. B (1971) <u>3</u> 1474.

97. J. A. Pople, W. G. Schneider, H. J. Bernstein, 'High Resolution Nuclear Magnetic Resonance Spectroscopy', p. 81, McGraw-Hill, New York (1959).

98. Value taken from J. A. Osborne, Phys. Rev. (1945) <u>67</u> 351.

99. D. G. Hughes, Private Communication.

100. S. Kobayashi, T. Takahashi, W. Sasaki, Phys. Letters (1970) <u>33A</u> 429.

101. H. R. Khan, J. M. Reynolds, R. G. Goodrich, Phys. Rev. B (1970) 2 4796.

102. W. M. Shyu, T. P. Das, G. D. Gaspari, Phys. Rev. (1966) 152 270.

103. E. F. W. Seymour, Proc. Phys. Soc. A (1953) 66 85.

104. J. J. Spokas, C. P. Slichter, Phys. Rev. (1959) 113 1462.

105. E. A. Faulkner, R. K. Ham, Phil. Mag. (1962) 8 7 279.

106. C. P. Flynn, E. F. W. Seymour, Proc. Phys. Soc. (1961) 77 922.

107. A. G. Anderson, Phys. Rev. (1959) 115 863.

108. N. Fernelius, Proc. XVI Ampere Congress, Ed. R. Blinc, p. 497, North-Holland, Amsterdam (1967).

109. T. J. Rowland, F. Y. Fradin, Phys. Rev. (1969) 182 760.

110. E. Van Meerwall, T. J. Rowland, Phys. Rev. B (1971) 3 1781.

111. W. Warren, R. E. Norberg, Phys. Rev. (1967) 154 277.

112. F. Y. Fradin, T. J. Rowland, Appl. Phys. Letters (1967) 11 207.

113. F. Y. Fradin, T. J. Rowland, Phys. Rev. B (1971) 3 1781.

114. J. H. Pifer, Phys. Rev. (1968) 166 540.

115. L. C. Hebel, C. P. Slichter, Phys. Rev. (1959) 113 1504.

116. M. R. Smith, Ph.D. Thesis, University of Alberta (Canada) (1972), communicated by D. G. Hughes.

117. J. Butterworth, Phys. Rev. Letters (1960) 5 305.

118. I. Solomon, Phys. Rev. (1958) 110 61.

119. J. Butterworth, Proc. Phys. Soc. (1965) 86 297.

120. W. D. Knight in 'Solid State Physics', Vol. 2, p. 93, Academic Press, New York (1956).

121. W. E. Blumberg, J. Eisenger, V. Jaccarino, R. T. Matthias, Phys. Rev. Letters (1960) 5 149.

122. See T. J. Rowland, Progress in Materials Science (1961) 9 1.

123. L. E. Drain, Proc. Phys. Soc. (1964) 83 755.

124. D. J. Lam, J. J. Spokas, D. O. Van Ostenburg, Phys. Rev (1967) 156 735.

125. H. E. Walchi, H. W. Morgan, Phys. Rev. (1952) 87 541.

126. J. Butterworth, Proc. Phys. Soc. (1965) 85 735.

127. See L. E. Drain, Metallurgical Reviews (1967) 12 195.

128. A. M. Clogston, A. C. Gossard, V. Jaccarino, Y. Yafet, Rev. Mod. Physics (1964) 36 170.

129. T. J. Rowland, Phys. Rev. (1956) 103 1670.

130. Y. Masuda, J. Phys. Soc. Japan (1957) 12 523.

131. L. E. Drain, Phil. Mag. (1959) 4 484.

132. F. Borsa, R. G. Barnes, J. Phys. Chem. Solids (1964) 25 1305.

133. E. F. W. Seymour, G. A. Styles, Phys. Letters (1964) 10 269.

134. R. G. Goodrich, S. A. Khan, J. M. Reynolds, Phys. Rev. B (1971) 3 2379.

135. H. Kruger, O. Lutz, A. Schwenk, G. Stricker, Z. Physik (1974) 266 233.

136. T. K. Kushida, L. Rimai, Phys. Rev. (1966) 143 157.

137. Y. Masuda, J. Phys. Soc. Japan (1958) 13 597.

138. E. M. Dickson, Phys. Rev. (1969) 184 294.

139. H. Alloul, R. Deltour, Phys. Rev. (1969) 183 414.